MATERIAL MODIFICATIONS FOR IMPROVED PERFORMANCE OF SHAPE MEMORY POLYMER MEDICAL DEVICES

A Dissertation

by

LANDON DANIEL NASH

Submitted to the Office of Graduate and Professional Studies of
Texas A&M University
in partial fulfillment of the requirements for the degree of

DOCTOR OF PHILOSOPHY

Chair of Committee,	Duncan J. Maitland
Committee Members,	Elizabeth Cosgriff-Hernandez
	Balakrishna Haridas
	David Staack
Head of Department,	Anthony Guiseppi-Elie

May 2017

Major Subject: Biomedical Engineering

ABSTRACT

Shape memory polymers (SMPs) are a class of materials that can be programmed into a secondary, metastable geometry and subsequently stimulated to return to their original geometry. These biocompatible materials enable the delivery and subsequent expansion of multiple catheter-based medical devices, including low density foams for embolic applications. In this work, cold plasma surface modifications and bulk compositional changes were used to address three design limitations of previous SMP systems: controlled foam expansion, controlled foam membrane removal, and inherent x-ray visibility.

SMP parameters including glass transition temperature, foam pore size, expansion rate in water, and x-ray contrast can be modified by altering the SMP composition or by using particulate additives to form an SMP composite. However, aggressive changes in bulk material chemistry can also affect properties associated with the surface, such as biocompatibility or hydrophobicity. To address the current limitations of SMP devices, this dissertation investigates the use of cold gas plasma techniques as an additional tool to alter surface material properties independent of bulk material composition.

The material modifications imparted by plasma processes or changes in composition were first analyzed on simple film and bulk substrates using techniques such as ellipsometry, x-ray photoelectron spectroscopy, Fourier transform infrared spectroscopy, differential scanning calorimetry, dynamic mechanical analysis, uniaxial

tensile testing, and goniometry. After material characterization, each process was applied to a specific medical device application and characterized based on device performance criteria. Device-specific characteristics, including cell-material interactions, x-ray visibility, fluid permeability, and expansion kinetics, were conducted on device prototypes using confocal microscopy, fluoroscopic imaging, flow system analysis, and isothermal expansion imaging, respectively.

Cold plasma film deposition using hydrocarbon gases was proven to influence SMP foam expansion kinetics by modulating the rate of moisture plasticization. Additionally, oxygen and tetrafluoromethane cold plasmas preferentially removed foam membranes to increase the interconnected porosity and fluid permeability of embolic SMP scaffolds with minimal impacts on material toughness. Finally, chemically incorporating triiodobenzene containing monomers not only provided x-ray visibility, but also significantly improved tensile toughness.

DEDICATION

Until I have kids of my own, this dissertation will probably be the biggest pain in the neck, but most rewarding thing I have ever created. I dedicate this work to the most loving, supportive, dedicated, patient and motivating parents I could have ever asked for. I'm proud to be your pain in the neck. I love you Mom and Dad.

ACKNOWLEDGEMENTS

I wouldn't trade it for anything in the world, but graduate school was really tough for a variety of reasons. I wouldn't have made it to the finish line without the help and support from numerous people that I am incredibly fortunate to have in my life. I expected to learn a significant amount of science during graduate school, but more surprising was the amount I learned about myself and what is most important to me. I learned, without a doubt, that the relationships with my friends and family will always be more rewarding than any professional or academic accolades. Although this section appears at the beginning of my dissertation, it was the section I drafted last because it is incredibly difficult, almost impossible, to put into words how much my friends and family mean to me.

First and foremost, I have to thank my advisor and greatest mentor Dr. Duncan Maitland (the BDL patriarch) for his advice, direction, and respect in both my professional and personal development over the last 6 years. I was incredibly hesitant to remain in my hometown for another 4 years of graduate school, but Duncan was a significant factor in my decision to stay in College Station and I never regretted it. I am a little disappointed that he set an impossibly high standard for my future bosses and additional mentors, but I think that is a good problem to have. Thank you Duncan for creating a unique, collaborative graduate school environment that enabled me to learn a variety of skills that extend beyond a traditional PhD experience. I'm sure these experiences will be valuable in my desired career as an entrepreneur.

I would also like to thank the “first generation” Biomedical Device Lab members (My BDL Aunts and Uncles), Wonjun Hwang, Andrea Muschenborn, Brent Volk, Jennifer Rodriguez, Pooja Singhal, and Keith Hearon. They are all talented scientists who always offered me selfless advice and guidance during my formative years in the lab. I would especially like to thank Keith Hearon for going above and beyond as a mentor and friend. He put me on the path towards enjoying polymer chemistry and solving engineering problems at the molecular level. I aspire to be as technically creative as him, and look forward to future collaborations.

My fondest graduate school memories were with my lab peers (BDL siblings). I can’t overstate the amount of respect I have for each one of you, and how proud I am of your accomplishments. It has been an honor to collaborate with Tony Boyle and wade through the trials and technical challenges associated with brain surgery. He is a pleasure to work with and helped me address my organizational and IT deficiencies. Mark Wierzbicki is one of the most talented engineers I’ve encountered, in addition to being one of the most patient and kind people I’ve ever met. I have always admired Todd Landsman’s work ethic and genuine selflessness. It always baffled me to see undergrads intimidated by the man who easily volunteered and gave back to his community more than anyone in BDL. Marziya Hasan is the Donna Meagle to my Tom Haverford. Thank you for being such a prolific collaborator and trusted friend. Adam Nathan and Jesse Bryant, I can’t acknowledge 90% of our best moments in this excerpt, but you are a true friends. It was a pleasure collaborating with Scott Herting and Grace Fletcher for a brief time. Scott taught me the true meaning of Aloha Friday, and Grace gave me a more

profound respect for “The Bachelor.” I have absolute faith that both of you will continue the illustrious BDL legacy. Finally, I would like to thank my BDL “Minions,” Kendal Ezell, Rachael Muschalek, and Jason Szafron for their dedication and incredible work ethic. I enjoyed mentoring each one of you, and I look forward to following your continued success.

To my family, thank you so much for your endless love and support. Mom and Dad, you are my greatest heroes, role models, and motivators. Everything about me stems from your hard work, compassion, and selflessness as parents. Hollee, nobody makes me laugh more often or harder than you. You will always be my big sister and hero.

CONTRIBUTORS AND FUNDING SOURCES

Contributors

This work was supported by a dissertation committee consisting of Professors Duncan Maitland, Elizabeth Cosgriff-Hernandez, and Balakrishna Haridas of the Biomedical Engineering Department and Professor David Staack of the Mechanical Engineering Department.

The cell culture experiments for chapter 3 was conducted by Jake Carrow of the Biomedical Engineering Department. Kendal Ezell of the Biomedical Engineering Department was a valuable collaborator throughout the completion of chapters 2-4. Nicole Rivera and Mary Beth Browning-Monroe of the Biomedical Engineering Department contributed the permeability and platelet/fibrinogen data in chapter 3, respectively. All other work conducted for the dissertation was completed by the student independently.

Funding Sources

Graduate study was supported by the Texas A&M University Merit and Enrichment Fellowships. This work was also supported by the National Science Foundation Graduate Research Fellowship Program grant number 1252521.

This work was made possible in part by the National Institutes of Health/National Institute of Biomedical Imaging and Bioengineering Grant R01EB000462 and Nation Institutes of Health/National Institute of Neurological Disorders and Stroke Grant NS089692.

NOMENCLATURE

AFM	Atomic Force Microscopy
ATIPA or AT	5-Amino-2,4,6-triiodoisophthalic acid
BDL	Biomedical Device Lab
BEP	2-Butyl-2-ethyl-1,3-propanediol
BL22	Tertiary amine blowing catalyst
BPC	Bare Platinum Coil
CVI	Chronic Venous Insufficiency
DMA	Dynamic Mechanical Analysis
DSC	Differential Scanning Calorimetry
E-beam	Electron beam radiation
EVA	Endovenous Ablation
HDI	Hexamethylene diisocyanate
HIPE	High Internal Phase Emulsion
HPED	N,N,N',N'-Tetrakis(2-hydroxypropyl)ethylenediamine
HT	1,2,6-Hexanetriol
MPD	3-Methyl-1,5-pentanediol
PECVD	Plasma Enhanced Chemical Vapor Deposition
PED	Peripheral Embolization Device
RF	Radio Frequency
SEM	Scanning Electron Microscopy

SMP	Shape Memory Polymer
T131	Organotin gelling catalyst
TEA	Triethanolamine
T_g	Glass transition temperature
THF	Tetrahydrofuran
TMHDI	Trimethylhexamethylene diisocyanate
W	Tungsten
XPS	X-ray Photoelectron Spectroscopy

TABLE OF CONTENTS

Page

LIST OF FIGURES

Page

LIST OF TABLES

Page

CHAPTER I

INTRODUCTION*

1.1 Shape memory polymers

Shape memory polymers (SMPs) are a class of materials that can be stimulated to actuate from a programmed, secondary metastable geometry to a primary geometry. This entropy driven process can be stimulated in a variety of ways, but this work focuses on thermally actuated SMPs, which actuate over a characteristic transition temperature.[5] This shape memory effect has been utilized to create devices with intricate geometries that are compressible to diameters small enough for delivery into the body via microcatheter. Once delivered to the target anatomy, the devices can be actuated to restore their primary shape and perform a therapeutic function. This approach has been previously implemented for the design of devices such as stents, thrombectomy devices, and laser stimulated micro actuators.[6-8]

SMPs consist of net points, which are a part of the stable polymer network, and reversible switching segments.[9, 10] Net points are responsible for the original shape while the switching segments provide the secondary shape and allow for shape change to occur. A thermally actuated SMP can be programmed, via external stress, into a secondary shape after being heated above the transition temperature of the switching segments. The new shape can be set by cooling at a constant load. The new shape is at a higher energy state because the new orientation of the polymer chains decreases the

*Parts of this chapter were reprinted from "Porous Shape Memory Polymers: Design and Applications," by Sayyeda M. Hasan, Landon D. Nash, Duncan J. Maitland, Journal of Polymer Science Part B: Polymer Physics 2016. Copyright (2016) John Wiley and Sons.

entropy of the system. However, the rigidity of the polymer chains below the transition temperature prevents the polymer from relaxing to the lower energy primary shape. When heated above the transition temperature, the programmed SMP returns to its original shape due to entropic recovery of the net points.[11, 12] In addition to ambient changes in temperature, this shape change can be triggered by different stimuli such as light, magnetic field, pH, solvent, and electricity and is dependent on the polymer type and incorporation of additives such as nanoparticles.[13].

1.1.1 Shape memory polymer medical devices

The biomedical device lab leverages the shape memory effect to create minimally invasive SMP medical devices.[14] These devices include shape memory polymer stents, septal occludes, thrombectomy devices, and embolic foams for peripheral vessel and aneurysm occlusion.[1, 4, 15-19]

Work by Nash et al. proposed a shape memory polymer microactuator for releasing microcatheter-based medical devices, such as SMP embolic foams.[20] This release device consists of a nichrome wire coil that resistively heats a shape set SMP tube, triggering it to radially expand and axially retract from the heating coil. The nichrome coil and crimped polymer tube are configured around a T type thermocouple to provide the user with temperature feedback and prevent the device from overheating within the patient. Figure 1.1 summarizes an in-vitro prototype deployment.

Although many SMP devices show promise for improving clinical outcomes for medical devices, the device designs and constituent materials still require improvement to create commercially viable devices that can translate from the research environment

to use in real patients. This dissertation focuses on solving technical hurdles for SMP devices to help facilitate clinical translation of SMP medical technologies.

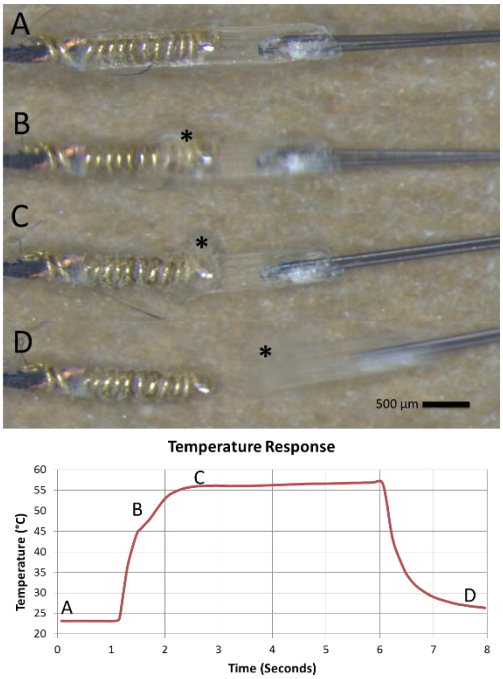

Figure 1.1: **Top: Sequenced images depicting micro-release device actuation. Asterisks identify the expanded portion of the SMP tube. Bottom: Measured device temperature at each stage of release.**

1.2 Porous shape memory polymers

Porous shape memory polymers have become particularly popular in the medical industry. Traditionally, porous polymers had applications as insulators and ion exchange resins.[21] However, these materials have also found use in the medical community as tissue engineering scaffolds for bone, drug delivery vehicles, and optical sensors.[21] Porous SMPs have a unique advantage as biomaterials because they can be implanted via minimally invasive procedures and undergo geometric changes after

implantation.[22] For tissue engineering applications, porous SMPs can be designed to serve as self-fitting scaffolds for tissue growth. Some stimulus-responsive hydrogels are also considered to be SMPs; however, this review will focus on porous SMPs that contain pores on the micrometer or larger scale.

1.2.1 Particulate leaching

Particle leaching is a fabrication technique that provides porous scaffolds with well-interconnected cells.[23, 24] This process consists of leaching solid particles out of a polymer system.[23, 25] A polymer solution is synthesized at varying solvent concentrations (5-20%).[26] Salt particles with a fixed diameter are mixed into the polymer/solvent solution to ensure uniform distribution.[27] The solvent is then removed via air-drying, vacuum-drying, or freeze-drying, leaving behind the salt particles embedded into the polymer matrix.[28] The polymer/solid composite is further immersed in water to dissolve the salt particles, leaving behind a porous, interconnected polymer scaffold.[27]

Scaffold porosity and cell size are dependent on the particle concentration and diameter, respectively.[25, 29] Insufficient particle concentration results in isolated pores that are surrounded by a thick layer of polymer. However, high particle loading causes voids, due to close poragen packing, which ultimately decreases mechanical properties. Hariraksapitak et al. reported changes in scaffold porosity directly related to particle concentration.[26] By increasing the particle concentration from 25x to 40x, larger voids were generated, which caused a significant decrease in mechanical properties. However, using particles ranging between 200–400 μm maintained uniform

pore size within the scaffold.[26] Most particle leaching techniques utilize salts; however, other particles such as sugar, ammonium chloride, sucrose, starch, paraffin, and gelatin particles have also been reported.[24, 25, 27]

Advantages of particle leaching include the ease of fabrication, since no specialized equipment is required for scaffold synthesis, uniform cell sizes, and interconnected pores. Difficulty associated with selecting particle type and size is a disadvantage because maintaining high porosity and adequate mechanical strength is a challenge. Lastly, unlike gas foaming, particle leaching has a risk of solvent toxicity on cells infiltrating the scaffold.[30]

1.2.2 PolyHIPEs

Porous scaffolds can be constructed from polymerized high internal phase emulsions (PolyHIPEs). HIPEs are typically defined as paste-like emulsions consisting of over 74% “internal” phase distributed within a continuous “external” phase.[31, 32] These scaffolds are particularly useful for biomedical applications due to their inherent potential for interconnected porosity. However, these emulsions are typically stabilized during polymerization by large amounts of surfactants. The impact of residual surfactant on material properties and the cost associated with the use and removal of these surfactants have motivated the use of alternative interface stabilization methods. Surfactant-free Pickering HIPES are stabilized at the oil-water interface by solid amphiphilic particles that migrate and self-assemble at the boundary layer.[33] These emulsions approach monodisperse void sizes, and they resist coalescence due to higher nanoparticle desorption energies when compared to traditional surfactants.[34-36]

Additional information on PolyHIPEs and Pickering HIPEs can be found in comprehensive reviews by Silverstein.[37, 38]

Specific to shape memory scaffolds, acrylate and methacrylate Pickering HIPES with shape memory capacities were successfully fabricated using silane functionalized nanoparticulate silica stabilizers that doubled as crosslinking centers to enable shape memory via side chain crystallization.[39] Gel content for each composition was above 90%, demonstrating effective nanoparticulate crosslinking. These constructs also demonstrated modest pore interconnectivity, recovery ratios of 1, and melt transitions ranging from 29 to 48 °C.

1.2.3 Gas blown polyurethane foams

Although gas blowing is traditionally used to create commercial polymer foams for thermal and mechanical insulation, the use of this fabrication technique has significantly increased in the medical industry.[21, 25]

Regardless of the desired application or foaming process being used, cell nucleation and growth of bubbles are important for the development of pores.[40, 41] Bubbles can be generated using three different methods: chemical, physical, and biological blowing. Chemical blowing agents generate gas due to a chemical reaction while physical blowing agents cause bubble formation as a result of mechanical action or phase transitions.[40] Biological agents are usually bacterial species that generate gas as a result of their metabolic functions.[40] Carbon dioxide (CO_2) and other volatile solvents are typical blowing agents due to their low critical point, non-flammability, and non-toxicity.[41, 42]

Gas foaming can be divided into two classes. The first class occurs when a liquid phase turns to vapor as a result of pressure drop or temperature rise.[40] Singhal et al. developed SMP foams that utilized gas blowing to achieve solid polyurethane foams. This polymer system was chemically crosslinked during foaming to maintain the pore morphology and prevent bubble coalescence.[3] Water was the chemical blowing agent for synthesis. During foam blowing, water reacted with the isocyanate monomers to generate carbon dioxide. The released gas provided cell nucleation and yielded a porous material with good interconnectivity. Pore structure and interconnectivity were tuned by controlling the type of foaming agent and its concentration in the polymer-gas mixture.[42] Reduced scaffold toxicity for in vivo applications is an advantage of gas blowing when compared to other fabrication methods.[25] Disadvantages associated with gas blowing include difficult control over pore sizes and connectivity.[25]

In the second class of gas-blown foams, a gas phase separates from a supersaturated solution due to changes in pressure and temperature. Inert gasses, such as carbon dioxide, can be compressed into supercritical fluids at pressures and temperatures above their critical point. These supercritical fluids simultaneously possess fluid characteristics, namely density, and gas properties such as compressibility and mass diffusion, which collectively enable supercritical fluids to solvate polymer networks.[43] Once the supercritical pressure conditions are removed, the dissolved gas expands and blows the polymer into a porous structure. The lack of residual solvents, catalysts, and surfactants make supercritical fluids attractive for creating porous structures for biomedical and tissue engineering applications.[44, 45] Supercritical carbon dioxide has

been used to create porous structures from blends of thermoplastic polyurethane and polylactic acid. Because the foam formation occurs below the thermal transition, these scaffolds have a dynamic, contractible porous structure that is proposed for drug delivery systems and wound dressings.[17]

1.3 Embolic applications for SMP foams

Low density SMP embolic foams have been proposed as a solution to alleviate the numerous drawbacks associated with current therapies for both intracranial and peripheral embolization.[3, 17, 46] Low density SMP foams can be compressed to fractions of their expanded volume, allowing them to be delivered through a microcatheter. As shown in Figure 1.2, a stimulus, such as heat, can restore the compressed foam to its original expanded geometry. The volumetric expansion capabilities and demonstrated biocompatibility of SMP foams make them a promising solution for providing more effective embolization and improved healing. However, additional work is needed to achieve facile device delivery and appropriate foam actuation profiles for commercial medical applications.

Previous work with SMP foams has focused on tailoring properties, such as the thermo-mechanical behavior or x-ray contrast, using bulk material changes or particulate additives, respectively.[47, 48] These approaches have achieved varying degrees of success for each application and frequently occur at the expense of other performance criteria. This dissertation solves material performance deficiencies using alternative techniques (surface or bulk chemistry modifications) in an effort to preserve desirable

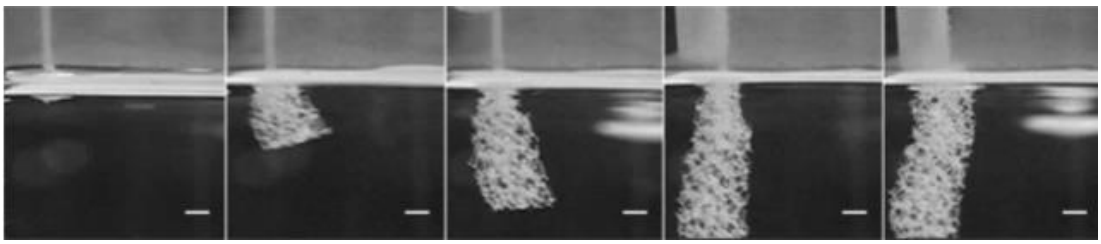

Figure 1.2: Time-lapsed images depicting the expansion of compressed SMP foam when submerged in a heated water bath. Scale is 2.5 mm.[3]

bulk material properties. Each aim is focused within the scope of a specific device application, either peripheral or intracranial aneurysm embolization.

1.3.1 Aneurysm embolization

The current gold standard for preventing hemorrhagic stroke involves treating intracranial aneurysms with bare platinum coils (BPCs), which are delivered through a microcatheter and left within the aneurysm to initiate a clotting response and divert blood flow from the aneurysm sac.[49] BPCs have helped to reduce the annual number of hemorrhagic stokes in the United States to approximately 103,000, but this treatment still has clinical limitations.[50] For instance, volumetric filling densities that are considered to be very high by clinical standards (30-35%) may not induce complete embolization.[51] Attempts to increase packing density with more coils can lead to over-packing and eventual aneurysm rupture. Embolizations that are initially effective can have recanalization rates as high as 35% and 50% in large and giant aneurysms, respectively.[49] Treating large aneurysms (11-20 mm diameter) requires an average of 159.5 cm of coils to completely occlude the aneurysm, which can cost as much as $97,000.[52, 53] This cost is associated with the number and type of implanted coils, as well as increased procedure time and complexity. Thus, the cost and efficacy limitations

of BPCs demand solutions for more efficient volumetric filling of intracranial aneurysms.

Stent-assisted coiling can be used to safely increase packing densities; however, this method occurs at the expense of higher procedure cost due to additional coils and a stent to bridge the aneurysm neck.[54-56] Despite their effective initial occlusion rates, stent-assisted coiling procedures still have recanalization rates as high as 12%.[56] Hydrogel-coated coils have been developed to increase volumetric aneurysm filling for comparable coil lengths. After implantation, the hydrophilic coating on these coils swells with water to effectively increase the coil diameter. Hydrocoils can consistently achieve packing densities above 50%, and they often achieve densities 3 times greater than bare platinum coils.[52] Despite these demonstrated packing densities, studies have shown no clear advantage for preventing aneurysm recurrence by coating platinum coils with hydrogels, making the additional cost associated with hydrophilic coatings unwarranted.[57, 58]

Significant advancements in the mechanical design and coating of bare platinum embolic coils have given clinicians a broad portfolio of devices to treat a wide variety of aneurysm geometries. However, there is still no clear endovascular solution for effectively treating all intracranial aneurysms, especially those classified as large or giant. There is still a clinical need for a reliable and cost-efficient embolization device with negligible recanalization rates.

Embolic SMP foams are proposed as an effective solution to these current clinical limitations. Figure 1.3 summarizes healing outcomes for SMP foams surgically

implanted in a porcine vein pouch aneurysm model. This dissertation addresses technical hurdles for the translation of microcatheter-delivered neurovascular embolic SMP coils, including tailored expansion profiles and improved x-ray visualization.

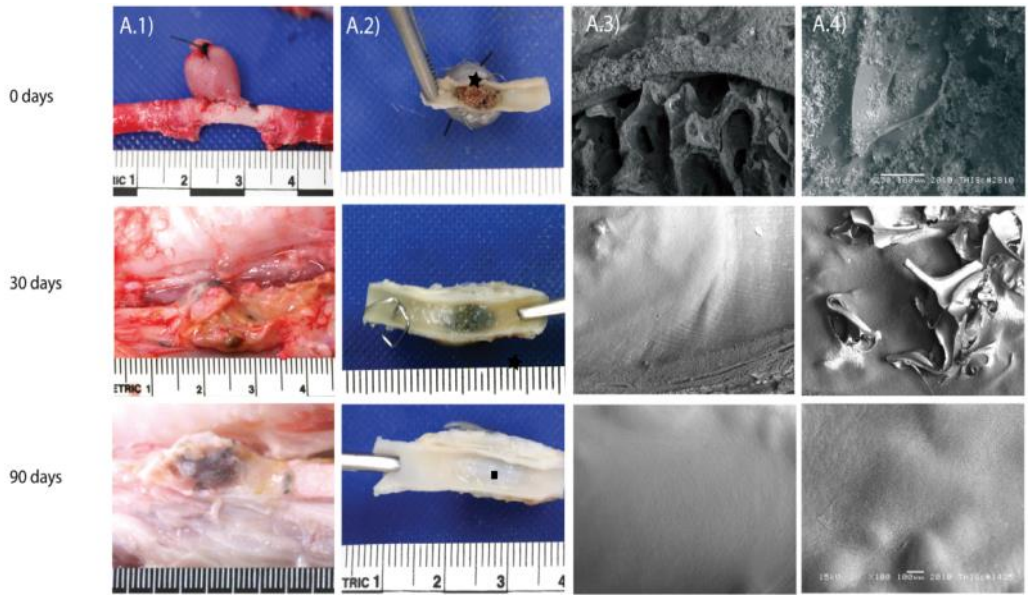

Figure 1.3: Pathology summary for SMP foams implanted in a porcine aneurysm model. Column A.1 depicts dissected aneurysms both ex vivo and in situ at 0-, 30-, and 90-day time points. Each aneurysm was filled with tungsten-doped embolic SMP foams.[4] Column A.2 shows clotting after initial implantation, healing, and complete endothelialization at 0-, 30-, and 90-day time points, respectively. Column A.3 is comprised of scanning electron microscope (SEM) images of the interface between the foam and vessel wall at the three time points. The red blood cells and fibrin within the first image are indicative of clotting at zero days. The lack of polymer strut visibility at 30 days is indicative of a developing mature endothelial covering. At 90 days, a mature endothelial lining obstructs any visibility of polymer struts. SEM images of healing at the base apex of the foam make up column A.4. The healing trends at each time point are similar to those seen in column A.3.

1.3.2 Peripheral embolization

In addition to aneurysm embolization, clinical needs exist for a variety of peripheral embolization applications. For example, better therapeutics are needed for the estimated 6 million Americans who suffer from severe symptoms of chronic venous insufficiency (CVI).[59] CVI occurs when venous valves are compromised and allow backflow in peripheral veins, leading to blood pooling, discomfort, varicose veins, and even venous ulcers. The manifestation and recurrence of venous ulcers contribute to the majority of costs associated with CVI, accounting for $1 billion in costs annually in the US.[60]

Although there are a multitude of embolization devices with peripheral indications, they have general limitations in the venous circulation due to the inherent compliance of veins and the presence of valves that may impede proper device placement and apposition to the vessel wall. Further, some treatments require embolization of large vessels, such as the full length of the great saphenous vein. The current standard of care for treating CVI is endovenous ablation (EVA), an ultrasound-guided therapy that uses a high energy source (e.g. lasers or radiofrequency generators) to cause significant damage to the vessel endothelium, leading to fibrous obliteration of the lumen. This treatment improves upon previous treatments, such as surgical ligation and stripping with recurrence rates as high as 52%; however, EVA is not without limitations.[61] For example, technique-dependent variables still make EVA susceptible to recanalization, which occurs after 24% of procedures.[62] Further, treatment options with EVA are limited because it cannot be used to treat short or highly tortuous

vessels.[62, 63] One of the largest drawbacks to the procedure is significant pain associated with multiple local anesthesia injections along the length of the vessel. These uncomfortable deep tissue injections are implemented to help alleviate long-term pain associated with the procedure and to provide an additional fluid volume to act as a heat sink during the procedure.[64]

As an alternative to stiff nitinol mesh occlusion plugs or multiple implanted embolic platinum coils, the superior embolization and long-term healing outcomes observed for SMP foams have been proposed as a superior solution to enable peripheral embolization with a single implanted device.[16, 17] This dissertation proposes techniques to alter the morphology and functional performance of gas-blown SMP scaffolds to enable this type of device. These material alterations are intended to improve device performance in terms of hemodynamics, acute cellular response, and noninvasive device visualization.

1.4 Cold plasma surface modifications

Cold plasmas, also known as nonequilibrium/nonthermal/low-temperature plasmas, are partially ionized reactive gasses.[65] The plasma field is an excited gaseous fluid system consisting of free electrons, radicals, ions, and neutral molecules. This reactive environment enables a wide variety of surface modifications on substrates including metals, ceramics, composites, and even temperature-sensitive polymers.[66]

Advantages of plasma surface modification include non-line-of-sight modification of intricate part geometries (e.g. Foams), flexible process chemistry, room temperature processing, and surface sterilization. These processing advantages enable a

variety of functional surface changes varying from chemical composition, surface roughness, electrical conductivity, optical characteristics, and biological interaction.[67-69]

Although plasma modification requires an initial investment in capital equipment, the consumable gasses are relatively inexpensive with minimal environmental impact compared to solvent-based wet chemistry surface modifications.[70] Plasma processes are also compatible with masking techniques typically found in the microelectronics industry to enable high fidelity surface patterning.[66]

1.4.1 Industrial plasma applications

Non-medical applications of plasma surface modifications include deposition of diamond-like carbon for low friction coatings, superhydrophobic surfaces for microfluidics or antifouling properties, increased surface adhesion of adhesives for composite manufacturing, and increased wetting of textiles for improved dye absorption.[71-75] Plasma processes have proven to be particularly useful in the semiconductor industry for etching microelectronic features in silicon wafers and removing polymer resist.[76, 77] These oxidizing plasmas serve as the basis for the reticulation plasmas used in chapter 3. Overall, the breadth of industry applications highlights the versatility of plasma functionalization for engineered surface solutions.

1.4.2 Biomedical plasma modification applications

Plasma processes are particularly useful for modifying biomaterial surfaces that interact with their implanted biologic environment.[68] Decoupling surface

characteristics from bulk material properties creates the opportunity for improved biomedical device performance.[78] Further, low temperature conditions and solvent-free processing facilitate modification of temperature-sensitive or biodegradable materials.[79]

The immersive nature of the plasma field also enables surface modification of surfaces beyond flat 2D substrates. Plasma modification has been used on porous substrates for increased cellular infiltration of tissue engineering scaffolds, porous biomaterial sterilization, altered wettability of porous polymers, and partial material foam membrane removal.[80-83]

1.4.3 Rationale for plasma modified SMP medical devices

Although the literature provides a wealth of insight into plasma surface modification of polymer substrates, it is sometimes difficult to resolve the multitude of differences in process conditions and the operation of custom-built plasma chambers. Leveraging the versatility of plasma surface modification approaches also requires careful consideration of numerous process conditions including sample fixturing, ambient moisture, RF chamber tuning, ionization power, process duration, chamber pressure, input gas composition, and process temperature.[84] This dissertation was focused on developing regimented, reproducible plasma modifications that are capable of being implemented at an industrial scale. To achieve this, all plasma treatments were conducted using a commercial-grade plasma treatment system, the Aurora 350 Plasma Surface Treatment system by Plasma Technology Systems. This system incorporates software for different levels of authorized use and rigorous tracking of all lot conditions.

Additionally, the device is housed within a class 100,000 clean room to simulate a medical device manufacturing environment. All of these features provide confidence that these developed processes could be implemented within a validated device manufacturing process.

Figure 1.4 is an excerpt from the Aurora user manual and provides an overview of the type of plasma reactor used in this dissertation. Briefly, a sample is held within a vacuum chamber with controlled gasses being introduced at a low pressure (~100 mtorr). The gasses flow past the sample in a laminar fashion while radiofrequency (RF) electrodes ionize the gas into a reactive cold gas plasma.

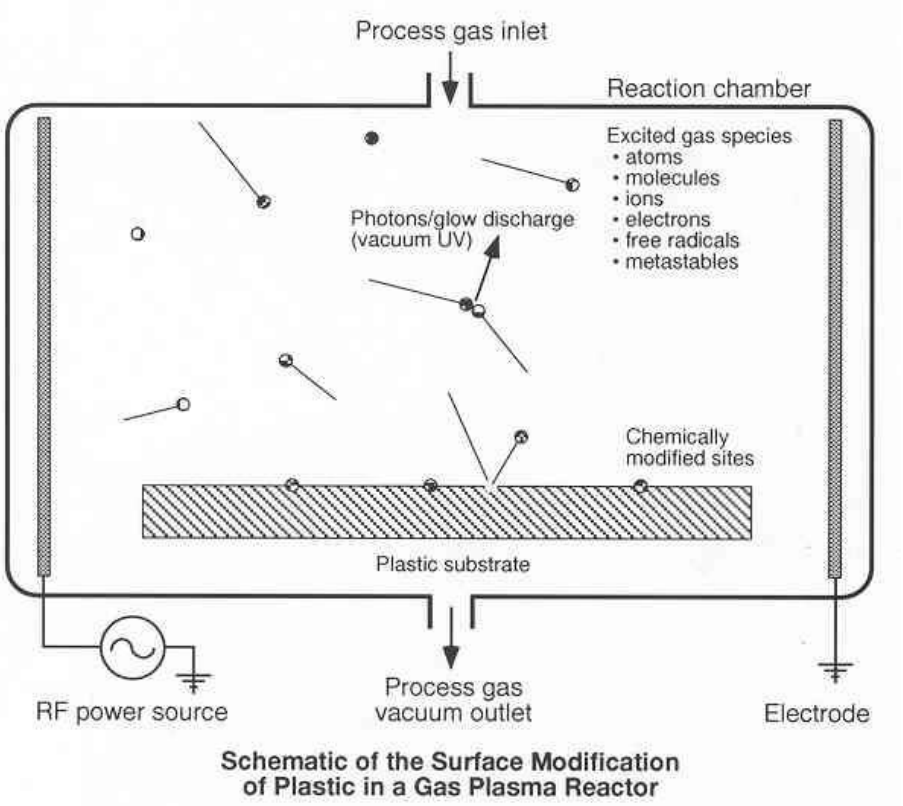

Figure 1.4: General schematic of the Aurora gas plasma reaction chamber.

CHAPTER II

PLASMA DEPOSITED HYDROCARBON DIFFUSION BARRIERS FOR CONTROLLED EXPANSION OF EMBOLIC FOAM DEVICES*

2.1 Introduction

Plasma deposited hydrocarbon films have been reported for a variety of applications, including low friction coatings, dielectric films, optical coatings, and surface modifying silica particles for petroleum hydrocarbon removal.[71, 85-87] Plasma processes have also been recognized as promising techniques for modifying biomaterials, including medical device sterilization, increased cellular affinity, surface functionalization, modulated biodegradation of PLLA fibers, and non-fouling applications.[29, 66, 67, 77, 80, 82, 88-97] Despite the wide variety of plasma induced biomaterial surfaces, a plasma approach has not been proposed to delay the moisture plasticization rate of SMP polyurethane foams.

Low density shape memory polymer (SMP) embolic foams have been proposed as a solution to alleviate the drawbacks associated with current embolization therapies.[3, 46] Low density SMP foams can be compressed to fractions of their expanded volume, allowing them to be delivered through a microcatheter. After implantation, a stimulus, such as heat, can restore the low profile foam to its original

---

*Parts of this chapter were reprinted from "Characterization of Plasma Deposited Hydrocarbon Diffusion Barriers for Embolic Foam Devices," by Landon Nash, Kendal Ezell, Sayyeda Hasan, and Duncan Maitland, 9th IEEE International Conference on Nano/Molecular Medicine and Engineering (NANOMED) 2015.

expanded geometry. Incorporating these low density SMP foams with current embolic coiling techniques can significantly reduce the number of coils used to treat an intracranial aneurysm, which also reduces procedure time and cost. Similar to other coil embolization devices, the embolic foam occludes the aneurysm by disrupting blood flow and causing a clot to form within the aneurysm volume. Results reported by Rodriguez et al. demonstrate promising biocompatibility for bulk SMP foams implanted in a porcine vein pouch aneurysm model.[98] The volumetric expansion capabilities and demonstrated biocompatibility of SMP foams make them a promising solution for providing more effective embolization and improved healing. However, additional work is needed for the effective delivery and actuation of these foams for commercial medical applications.

A major hurdle for the realization of aneurysm filling SMP embolic foams is the concept of working time, which is the window of time a physician has to deliver an SMP device through a microcatheter, reposition the device in the aneurysm, or retract the device before it has expanded sufficiently to bind within the catheter. Bulk material modifications have successfully delayed or prevented moisture-plasticized foam expansion at body temperature by increasing the material hydrophobicity or rigidity of the polymer backbone.[48, 99, 100] However, these bulk modifications simply change the linear expansion rate, which requires concessions for ultimate device expansion or a working time that is at the clinical minimum of 5 minutes, based on predicate devices.[101] Ideally, the foam would actuate in a nonlinear fashion, where the device expands a few thousandths of an inch over approximately 10 minutes and subsequently

recovers 20–30 thousandths in the next 20 minutes. This idealized expansion profile would enable clinically relevant SMP devices for treating neurovascular aneurysms. A hydrocarbon surface diffusion barrier deposited using plasma-enhanced chemical vapor deposition (PECVD) is proposed to achieve this ideal nonlinear expansion behavior by delaying the moisture plasticization rate of the SMP foam without mechanically constraining the material.

In this study, unsaturated hydrocarbon gasses, including acetylene, ethylene, and propylene, are used to deposit aliphatic water diffusion barriers to slow the moisture plasticization rate of SMP foams and delay passive foam expansion in vitro. By altering the bulk hydrophobicity of the foam and the diffusion characteristics of the surface, the actuation profile of the foam can be tailored for delayed expansion in body-temperature water.

2.2 Materials and methods

2.2.1 Plasma processes

This study focused on characterizing the functional relationship between process parameters and the characteristics of the resulting plasma-deposited film. Process gas compositions and room temperature chamber pressures prior to plasma ignition are summarized in Table 2.1. Plasma gas compositions were run on silicon wafers at four

Table 2.1: Plasma gas compositions and flow rates. LE - Low flow ethylene, LEA - Low flow ethylene/acetylene, HE - High flow ethylene, HEA - High flow ethylene/acetylene, LP - Low flow propylene, LPA - Low flow propylene/acetylene, HP - High flow propylene, HPA - High flow propylene/acetylene. Process flow rate in standard cubic centimeters (sccm).

Process Label [a]	**Process Conditions**			
	Ethylene Flow Rate (sccm)	***Propylene Flow Rate (sccm)***	***Acetylene Flow Rate (sccm)***	***Average Process Pressure (mtorr)***
LE	150	-	-	77
LEA	125	-	25	77
HE	300	-	-	125
HEA	250	-	50	125
LP	-	150	-	70
LPA	-	125	25	74
HP	-	300	-	119
HPA	-	250	50	119

time intervals between 1 and 30 minutes at the discrete powers of 75, 150, 225, and 300 Watts for a total 128 different process combinations.

2.2.2 Sample preparation

Silicon wafers (University Wafer,Inc.) were cut into rectangles approximately 1.25 cm x 1.7 cm, cleaned in water and isopropanol under sonication for 15 minutes each, dried overnight at 1 torr, and stored under desiccation.

All SMP polyurethane foams were fabricated according to the protocol reported by Singhal et al.[3] with a 33:67 hydroxyl equivalent ratio of triethanolamine (TEA) to N,N,N',N'-tetrakis(2-hydroxypropyl)ethylenediamine (HPED). Foams used for differential scanning calorimetry (DSC) were made with an isocyanate composition of 100 percent hexamethylene diisocyanate (HDI). Two additional foam compositions were synthesized for expansion studies using a 50:50 isocyanate ratio of HDI to trimethylhexamethylene diisocyanate (TM). Based on results from a concurrent study, 3

weight percent nanoparticulate tungsten was included in one synthesis, and the other included 1 weight percent nanoparticulate aluminum oxide.[102] After synthesis, all foams were cut into 1.5 x 1.5 x 4 cm blocks and cleaned in vials using 15-minute sonication intervals. The first interval used reverse osmosis filtered water, followed by 2 intervals of isopropyl alcohol and 4 intervals of reverse osmosis water. The cleaned foams were frozen, lyophilized, and stored under desiccation.

Cleaned foams were punched into 1 mm diameter, 4 cm long cylinders using a biopsy punch and threaded axially over a 150 micron (0.006") diameter stainless steel wire. Foams intended for expansion studies were then transferred to 0.006" diameter 92/8 Pt/W coils (Motion Dynamics) with a 0.002" diameter propylene suture threaded through the lumen. Foam-over-wire (FOW) samples and foam-over-coil (FOC) samples were plasma treated while suspended between two 4.5 cm tall glass cuvettes. 100HDI FOW samples were used for differential scanning calorimetry. 50TM FOC samples were compressed using an SC250 Stent Crimper (Machine Solutions Inc.) after plasma treatment. FOC samples were loaded into the crimper at 100°C, equilibrated for 15 minutes, compressed to an average diameter of 305 microns (0.012"), and held compressed during a convective air cooling cycle over a one-hour period. Once at room temperature, the samples were removed and stored under desiccation.

2.2.3 Plasma treatment

Plasma films were deposited using an Aurora 350 Plasma Surface Treatment System (Plasma Technology Systems). The reaction chamber held a single glass shelf mounted in the third rack space from the bottom. For mapping the spatial reactivity of

the plasma field, silicon wafers were fixed to 4.5 cm tall glass cuvettes placed in a 6 x 6 grid on the glass shelf. All other experiment samples were fixed to the top of a 4.5 cm tall glass cuvette centered in the back third of the shelf. The chamber was evacuated to a base pressure of 10 mtorr, followed by process gas introduction into the chamber at the specified process flow rate for 1 minute prior to plasma ignition. The plasma field was generated using a continuous 13.56 MHz RF power supply, and the process gasses continued flowing through the chamber for 1 minute after plasma treatment. The chamber was then purged with atmospheric air for 10 minutes and returned to atmospheric pressure. All samples were stored in polypropylene bags or trays under desiccation.

2.2.4 Ellipsometry

Ellipsometric thicknesses were measured using an Alpha-SE Spectroscopic Ellipsometer (J.A. Woollam Co.) operating at 380–890 nm and a 70° angle of incidence. Data analysis employed a J. A. Woollam optical model assuming a thin transparent film on a Silicon substrate.

2.2.5 Contact angle

Static water contact angle measurements were made with a CAM 200 Goniometer (KSV Instruments) using drop volumes of 5 µl. Six contact angles were measured for each reported process using a Young/Laplace fitting model.

2.2.6 X-Ray photoelectron spectroscopy (XPS)

Silicon wafers were treated with LP and LPA processes at 75, 150, 225, and 300 watts for X-ray photoelectron spectroscopy (XPS) analysis. Plasma treatment times were

chosen to deposit a normalized film thickness of 30 nm for each process. XPS spectra were acquired using an Omicron ESCA+ system with a Mg X ray source and CN10 charge neutralizer. Atomic ratios were calculated using the software Casa XPS.

2.2.7 Differential scanning calorimetry (DSC)

Polymer glass transition temperatures (T_g) were determined for 100HDI FOW samples using a Q200 DSC (TA Instruments). For dry T_g, a 0.5–2 mg sample was loaded into a vented aluminum pan at room temperature, cooled to -40°C, and run through a heat/cool/heat cycle from -40°C to 120°C at temperature rates of 10°C/min. T_g was determined to be the transition inflection point during the second heat cycle. For wet T_g analysis, foam-over-wire samples were immersed in a 50°C water bath for 5 minutes and subsequently compressed between laboratory grade Kimwipe sheets (Kimberly-Clark Inc.) at 1 metric ton for 30 seconds using a #3925 Hydraulic press (Carver, Inc). The foam was then loaded into a vented aluminum pan, cooled to -40°C, and heated to 80°C at 10°C/min. Wet T_g was determined to be the heating cycle transition inflection point. Wet and Dry T_gs were measured for 5 samples of each reported plasma composition.

2.2.8 Foam expansion

Compressed FOC diameters were measured with a stereoscopic microscope (Leica KL 2500 LCD). A custom aluminum fixture was used to hold FOC samples in the same plane as a 12 mm geometric standard. The fixture was submerged in a 37°C water bath and imaged from above at 30 second intervals for 30 minutes. Five diameter measurements were taken along the length of each foam sample within the captured

images using ImageJ software (National Institutes of Health). Five samples of each plasma composition were measured.

2.3 Results and discussion

2.3.1 Spatial plasma reactivity

As seen in Figure 2.1, the plasma deposition rate increases toward the back of the plasma chamber, except for a low reactivity margin around the periphery of the shelf. This reactivity gradient is in parallel with the flow of process gasses through the

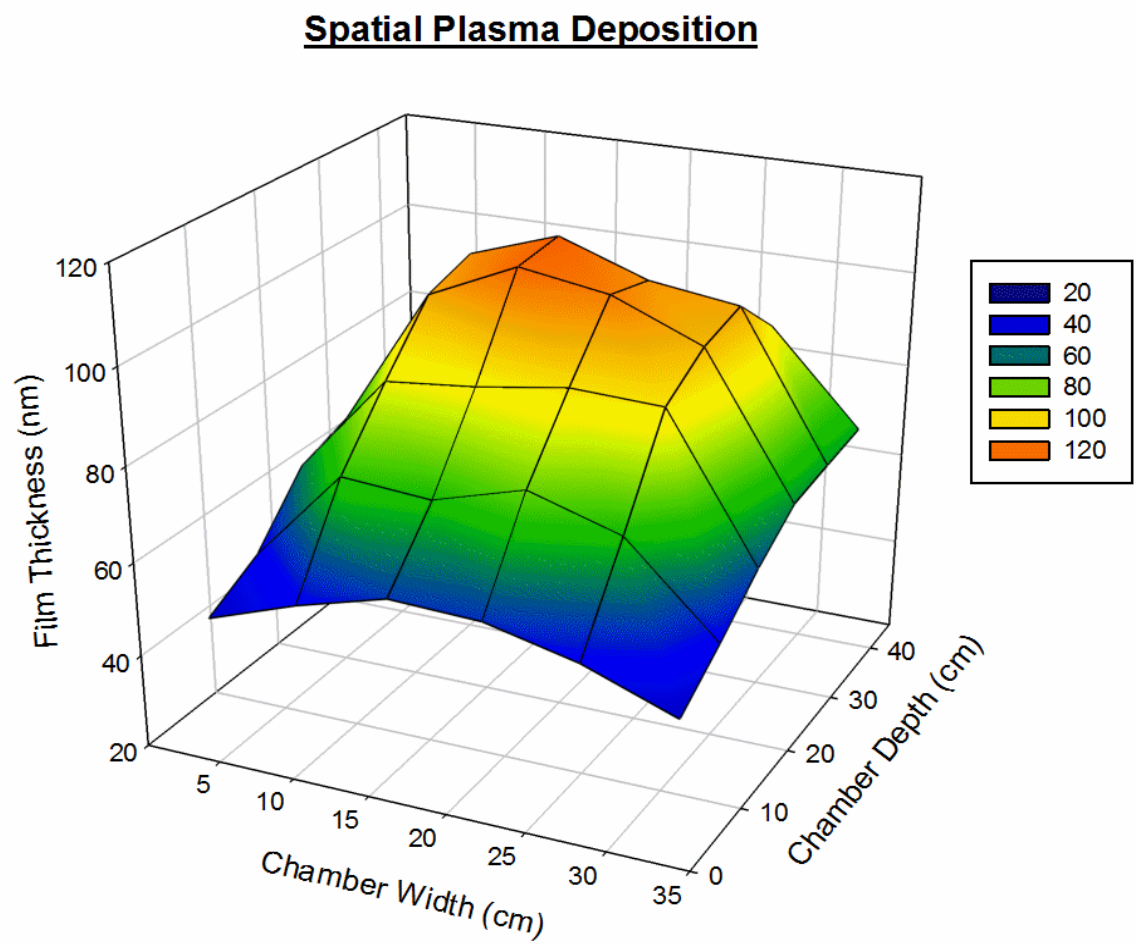

Figure 2.1: Ellipsometry measured spatial deposition map for a 6 x 6 grid of silicon wafers raised on glass cuvettes and treated with a low flow ethylene and acetylene process at 150 watts for 7.5 minutes.

chamber. Thus, the deposition profile increases as gaseous species are exposed to the RF field for longer periods of time, increasing their reactivity. To mitigate variations due to sample placement within the chamber, all subsequent samples were fixtured within the orange region (100–120 nm deposition) shown in Figure 2.1.

2.3.2 Hydrocarbon film deposition

Film deposition profiles were measured to determine the deposition rate for each plasma process. The graphs in Figure 2.2 depict typical deposition profiles for high flow ethylene (HE) and high flow ethylene/acetylene (HEA) processes. All processes show

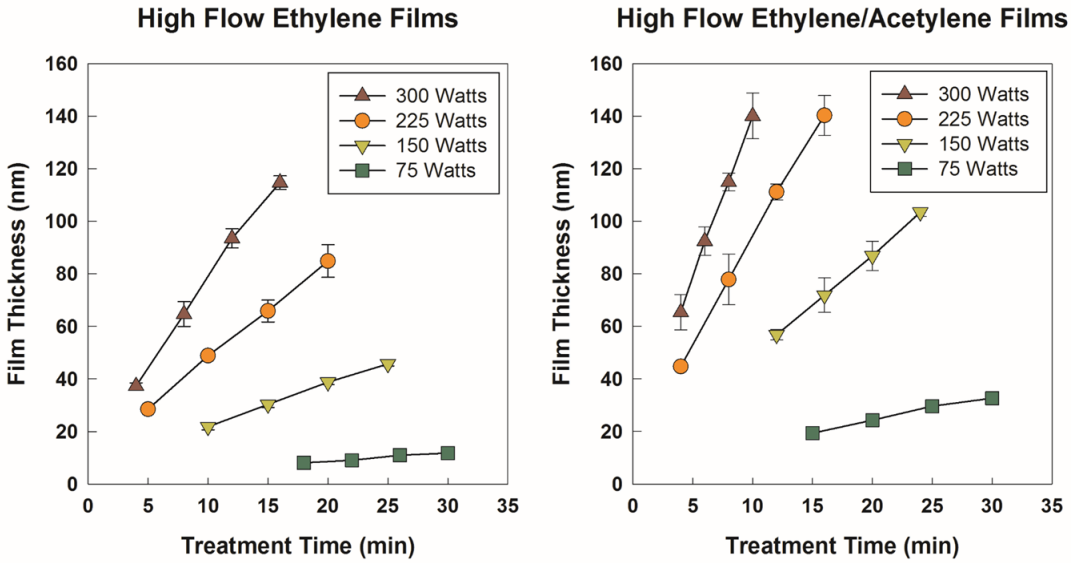

Figure 2.2: Plasma film deposition profiles for silicon wafers treated with high flow ethylene processes (left) and high flow ethylene/acetylene processes (right) as measured by spectroscopic ellipsometry. Error bars are MSE values for the optical model fit.

linear time dependent deposition profiles. The average R^2 value for all 32 linear regressions is 0.992. As seen in Figure 2.2, deposition rates increased with increasing power, and with the introduction of acetylene (i.e., HEA) at similar process conditions.

Figure 2.3 summarizes the deposition rates determined from all 128 processes. The power-dependent change in deposition rate is assumed to be linear over the studied power range, and the average linear R^2 value for all 8 plots in Figure 2.3 is 0.960. Increasing process power, decreasing process pressure, and introducing acetylene to a process all result in an increased deposition rate. In general, ethylene processes have faster deposition rates than propylene.

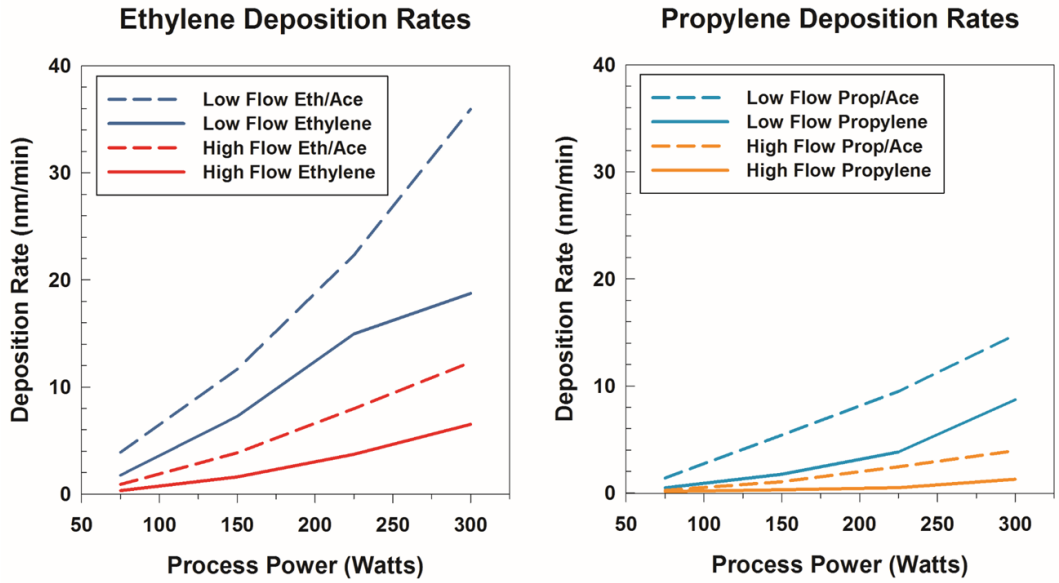

Figure 2.3: Plasma film deposition rates for ethylene processes (left) and propylene processes (right). Deposition rate was assumed to be the slope of the linear fit for each time dependent deposition profile for a given process.

2.3.3 Film hydrophobicity

Static water contact angles for each process gas and power combination are summarized in Figure 2.4. Contact angle decreased with increasing process power and when introducing acetylene to a process. Propylene processes were consistently more

hydrophobic than ethylene processes, presumably from methyl groups incorporated within the film. In general, process parameters that increased film deposition rate tended to decrease surface hydrophobicity. All plasma deposited films were significantly more hydrophobic than untreated silicon wafers, which had an average contact angle of 37 ± 1°C.

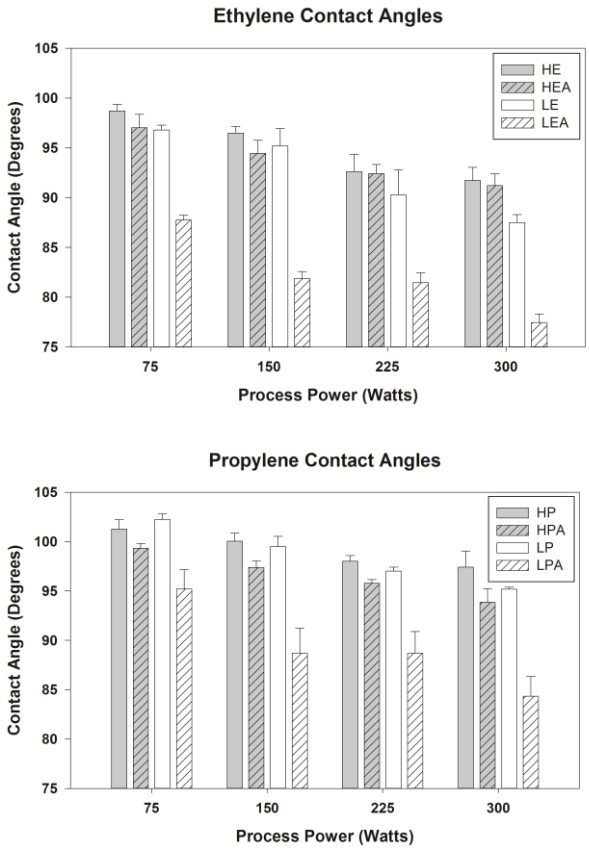

Figure 2.4: Static water contact angles on treated silicon wafers. Top Panel: high flow ethylene (HE), high flow ethylene acetylene (HEA), low flow ethylene (LE), and low flow ethylene (LEA) processes. Bottom panel: high flow propylene (HP), high flow propylene/acetylene (HPA), low flow propylene (LP), and low flow propylene/acetylene (LPA). Untreated silicon wafers had contact angles of 37 ± 1° (not shown). Error bars are standard deviation (n=6).

Selected processes were chosen for XPS analysis to determine the cause of power-dependent changes in contact angle. All films were normalized to an average thickness of 30.5 ± 1.5 nm. As shown in Figure 2.5, increasing process powers resulted in higher rates of film oxidation, which contribute to lower water contact angles. This oxidation is likely due to residual radicals from higher energy processes reacting with atmospheric oxygen after plasma polymerization. Similarly, the higher reactivity of the acetylene processes likely result in higher levels of residual radicals that oxidize after plasma treatment.

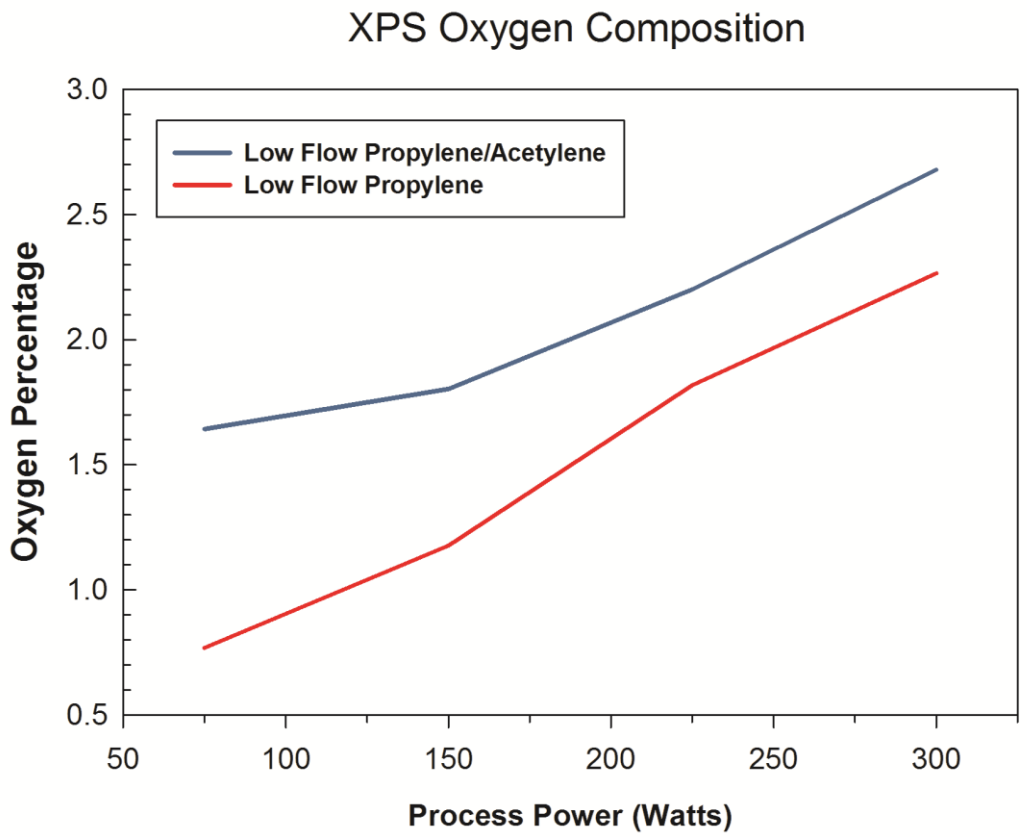

Figure 2.5: **Power-dependent film oxygen concentration for low flow propylene and low flow propylene/acetylene process films as measured by XPS.**

2.3.4 Effects on T_g

Four plasma processes were chosen to encompass a variety of process powers, gas compositions, pressures, and ranges of surface hydrophobicity. These processes were applied to the 100HDI foams at a normalized thickness of 20 nm. The dry and moisture saturated glass transition temperatures for these foams are summarized in Table 2.2.

Table 2.2: Glass transition temperatures (n=5)

Process Label*	***Contact Angle (Degrees)***	***Dry T_g (°C)***	***Wet T_g (°C)***
Untreated	72.8 ± 0.8	70.0 ± 0.5	14.7 ± 0.7
LEA75	88 ± 0.5	70.1 ± 0.4	17.1 ± 0.7
LE225	90 ± 2.5	70.1 ± 0.4	15.6 ± 1.0
HE300	92 ± 1.3	69.7 ± 0.5	17.1 ± 0.7
LP75	102 ± 0.6	70.1 ± 0.3	16.8 ± 0.8

*Label numbers indicate process power

None of the four processes had a significant effect on the thermal properties of dry SMP foams. The glass transitions of moisture saturated SMP foams were marginally increased by the diffusion barriers. This suggests that the bulk polymer thermal properties are preserved and that any changes in foam expansion rate would largely be due to the surface polymerized films modulating the rate of moisture plasticization.

2.3.5 Effects on expansion rate

Shape memory polymer foam-over-coil prototype devices are shown in Figure 2.6. The device dimensions and constituent materials were chosen based on requirements for neurovascular delivery such as x-ray contrast and crimped diameter.

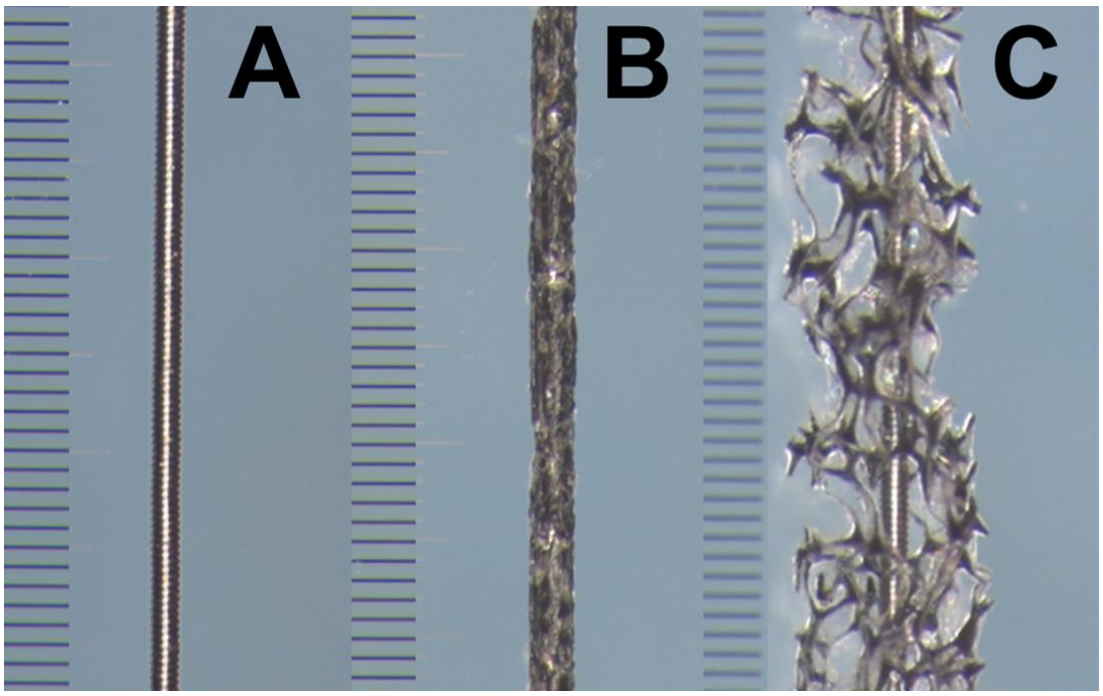

Figure 2.6: **A) Bare 0.006" diameter platinum/tungsten coil. B) Crimped SMP foam coating with 0.012" average diameter. C) Expanded 0.040" diameter SMP foam coated coil. All scales are 0.1 mm.**

Figure 2.7 summarizes in vitro foam expansion for two different plasma processes when compared to untreated foams. Working time is assumed to be the standard deviation intercept with the dotted line, which represents the lumen of a traditional 0.021" microcatheter used to deliver neurovascular coils.

The working time for untreated tungsten doped foam is between 2 and 3 minutes (Figure 2.7, top image). The ethylene plasma treatment (LEA75) marginally extended this working time to between 3 and 4 minutes. Both of these working times are unacceptable for the clinical environment. With a working time between 7 and 8 minutes, the propylene plasma process (LPA75) effectively tripled the working time of untreated tungsten doped foam and enabled clinically relevant SMP foam performance.

When considering alumina doped foams, the working time for untreated foam is between 4 and 5 minutes (Figure 2.7, bottom image). Ethylene plasma treatment (LEA75) successfully extended working time above the clinical threshold to between 6 and 7 minutes. Propylene-treated (LPA75) alumina doped foams had the longest working times between 9 and 10 minutes. This device performance is well within the therapeutic range for safely delivering an embolic coil, including a clinical safety factor.

Similar to bulk approaches for delaying SMP foam expansion, the observed increases in working time come at the expense of ultimate expanded diameter. Maximum expansions were determined after 30 minutes of immersion because it is estimated that acute clot formation will limit further expansion on this time scale. Untreated tungsten doped foam recovered to an average diameter of 0.044" compared to 0.037" and 0.027" for LEA75 and LPA75 treated foams, respectively. Control alumina doped foam recovered to an average diameter of 0.036" compared to 0.030" and 0.026" for LEA75 and LPA75 treated foams, respectively.

Although decreases in ultimate expansion limit the potential volumetric occlusion for each device, the smallest reported ultimate foam diameter of 0.026" provides more volumetric occlusion and surface area through a smaller catheter lumen than the largest marketed bare platinum neurovascular coils.[103] This expanded diameter also provides similar volumetric filling with a higher surface area when compared to 0.027" expanded diameter hydrogel coated HES-14 coils delivered through 0.019" ID microcatheters.[101] Finally, LEA75 treated alumina foams had comparable

ultimate expansion on a similar 5 minute time scale to 0.033” expanded diameter hydrogel coated HES-18 coils delivered through 0.021” ID catheters.[101, 104]

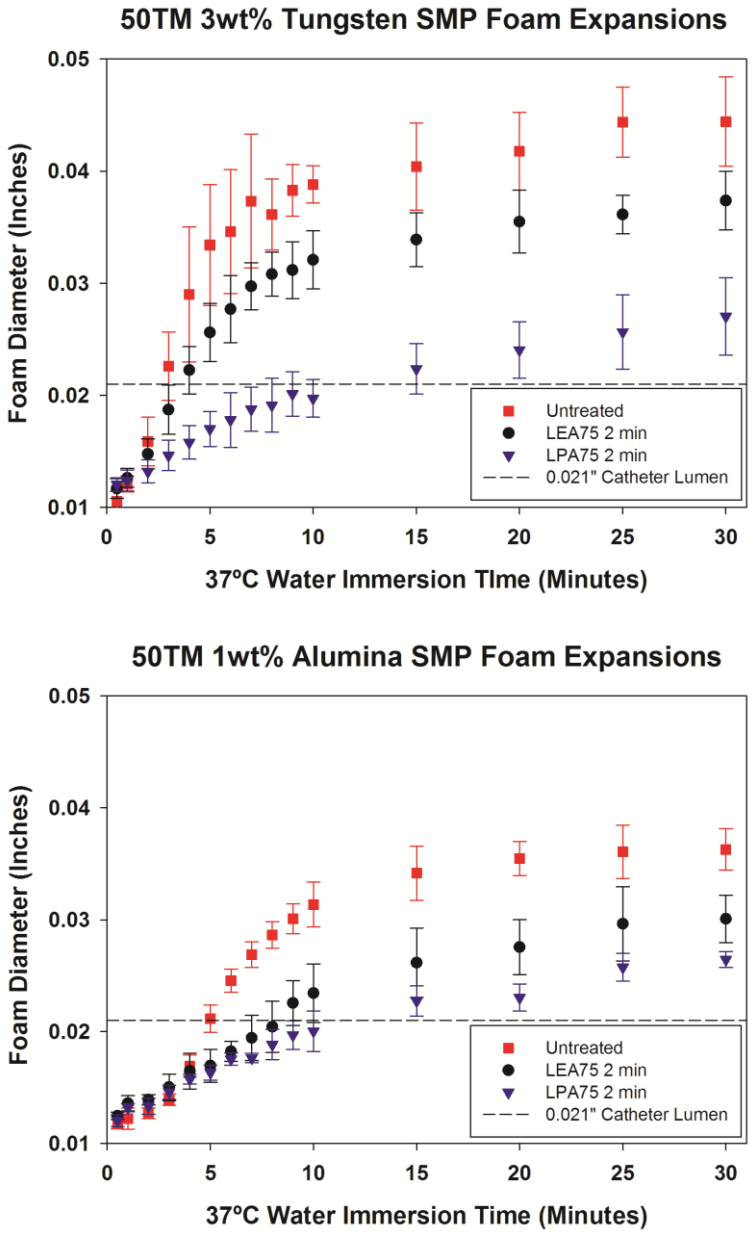

Figure 2.7: Unconstrained expansion profiles for untreated and plasma treated SMP foams doped with tungsten (top) and alumina (bottom) nanoparticulates. Working time is determined by the standard deviation intercept with the dotted line representing a 0.021” lumen microcatheter.

2.4 Conclusion

This study proved that plasma-deposited hydrocarbon films are effective water diffusion barriers for delaying the rate of moisture plasticization in SMP embolic foams. Reported device materials, catheter sizes, delivery working times, and expansion diameters all fall within clinically relevant device specifications with comparable performance to existing neurovascular devices. This benchmark device performance study and the favorable biocompatibility of SMP foam make these devices promising for future aneurysm therapies.

CHAPTER III

COLD PLASMA RETICULATION OF SHAPE MEMORY EMBOLIC TISSUE SCAFFOLDS*

3.1 Introduction

Shape memory polymer (SMP) foams have shown promise as effective embolic materials that address current embolization technique limitations by reducing the number of devices needed for treatment and improving long term healing outcomes.[1, 14, 46, 105] These low density materials can be radially compressed and programmed into a low volume configuration to facilitate minimally invasive catheter delivery to a diseased vascular anatomy. Once delivered, the material can be stimulated with heat to expand to its primary configuration for effective volumetric filling and flow stasis, leading to embolization. These materials demonstrate excellent biocompatibility for aneurysm embolization applications, but additional material optimization is necessary to enable their use in other applications, such as peripheral embolization devices to treat chronic venous insufficiency.[106]

The implanted SMP foam is intended to serve as a tissue scaffold for thrombus formation and subsequent cell-mediated healing. However, gas blown foams inherently have membranes between pores, which can limit their performance as tissue scaffolds.[3] Namely, implanted foams without interconnected pores can limit cellular

*Parts of this chapter were reprinted from "Cold Plasama Reticulation of Shape Memory Polymer Embolic Foams" Macromolecular Rapid Communications, 2016.

infiltration during healing. Low permeability foams can also generate large pressure gradients in circulation, leading to potential device failure or migration after deployment in peripheral vasculature.

Reticulation, or the removal of membranes between adjacent foam pores, is advantageous for increasing foam permeability to improve material performance. Controlled reticulation of SMP foams would provide multiple benefits, such as an optimized surface area to volume ratio for intrinsic pathway-triggered blood coagulation and flow stagnation within the foam to produce thrombogenic fluid shear rates.[107-109] Additionally, reticulated foams would allow for cellular infiltration as the body heals the thrombus within the foam.[110]

Traditional reticulation processes are too aggressive to use with ultra-low density SMP foams (~0.015 g cc-1). Commercial techniques, such as acid etching, concussion, mechanical cycling, and combustion, can significantly decrease the mechanical integrity of the foam. A mechanical reticulation method that utilizes a floating array of weighted flexible pins to preferentially puncture foam membranes was previously reported as an effective reticulation method for ultra-low density SMP foams with demonstrated utility in vessel occlusion.[106] Alternatively, cold gas plasma can be used for SMP foam reticulation. The proposed process uses a reactive oxygen (O2) and tetraflouromethane (CF4) plasma, commonly used to etch features for microelectronics, to non-thermally degrade and volatize high surface area membranes and reticulate SMP foam structures.[76, 111-113]

Plasma processes have been widely used to alter the surface chemistry of biomaterials.[66, 67, 69, 78] Many of these processes increase surface hydrophilicity for enhanced cell attachment.[80, 97, 114] Other studies aimed to modify the interior surfaces of porous structures.[75, 83, 115] We hypothesize that the proposed plasma treatment can be utilized to reticulate foams in a controlled manner. Previously, a group used H_2O_2 plasma to sterilize SMP foams with an observed increase in pore interconnectivity.[29] Fu et al. also observed increases in porosity when treating polyurethane substrates with an active screen plasma.[81] However, no studies have explicitly focused on using plasma to tune the opening of porous structures. This work characterizes the effects of cold gas plasma reticulation processes on bulk polyurethane SMP films and foams to enhance their functionality and expand their potential use as embolic scaffolds.

3.2 Materials and methods

3.2.1 Sample preparation

SMP foams were prepared according to the protocol described by Singhal et al. with an isocyanate composition of 100 mol% trimethylhexamethylene diisocyanate (TM) and a hydroxyl equivalent mole ratio of 33:67 triethanolamine (TEA) to N,N,N',N'-tetrakis(2-hydroxypropyl)ethylenediamine (HPED).[3] The cured foams were cut with a resistive wire cutter into 50 x 50 x 25 mm blocks and washed to remove residual surfactants and catalysts. The previously reported cleaning protocol involved two, 15-minute sonication intervals in reverse osmosis (RO) water, one interval in a 20 vol% Contrad® 70 solution in RO water (Decon Laboratories, King of Prussia, PA), and

four, 15-minute intervals in RO water.[105] Cleaned samples were frozen in aluminum trays and lyophilized for 3 days. Dried foams were stored in polypropylene bags under desiccation.

Neat polymer films were prepared with the same monomer ratios as the foam. The monomers were massed into a Flacktek speed mixing cup (Flacktek SpeedMixers, Landrum, SC) in a moisture-controlled glovebox. The reaction components were then mixed at 3400 rpm for 2 minutes to create a single phase solution. Once mixed, the solution was poured into a polypropylene casting tray and oven cured by heating to 120°C at a rate of 30°C hr-1 and holding at 120°C for one hour. Films were then cooled to ambient temperature, milled on a single side to a uniform thickness of 0.2 cm, and CO_2 laser-cut into 2 cm squares. The top face of the film that was in contact with air during curing was preserved for surface analysis. Cured films were stored in polypropylene bags under desiccation.

3.2.2 Plasma reticulation

Plasma treatment was conducted using an Aurora 350 Plasma Surface Treatment System (Plasma Technology Systems). Polymer foam blocks were fixed on a 12.5 cm tall aluminum mesh fixture centered in the back third of the reaction chamber. Polymer films were fixed to a 4.5 cm tall glass cuvette during treatment. The chamber was evacuated to a base pressure of 10 mtorr, and then O_2 and CF_4 process gasses were introduced into the chamber at 200 sccm and 800 sccm, respectively, to bring the chamber to a pressure of 385 mtorr. Foam samples were plasma treated at 300 Watts for 8 or 15 minutes for partial or full reticulation, respectively. Unless otherwise stated, all

film samples were treated with the full 15-minute process. Plasma-treated samples were stored in polyethylene bags under desiccation.

3.2.3 Scanning electron microscopy

Using a resistive wire cutter, foam samples were cut into 1 mm slices parallel (axial) and orthogonal (transverse) to the foaming axis. Each slice was mounted to a stage with carbon black tape and sputter coated for 90 seconds at 20 mA using a Cressington Sputter Coater (Ted Pella, Inc. Redding, CA). Samples were then visualized using a Joel NeoScope JCM-5000 Scanning Electron Microscope (SEM) (Nikon Instruments, Inc., Melviille, NY).

3.2.4 Mechanical testing

Uniaxial tensile tests were conducted at room temperature using an Insight 30 Material Tester (MTS Systems Corporation, Eden Prairie, MN) with a constant strain rate of 50 mm/min. Ultimate tensile strength (kPa), strain at break (%), and elastic modulus (kPa) were calculated from the stress-strain curve of each sample. Statistical analysis was conducted using a one-way ANOVA with Bonferroni's multiple comparisons test to the untreated control values.

3.2.5 Permeability

The porous media properties of the plasma-reticulated and untreated foams were measured using a permeability system as previously reported and calculated using the Forchheimer-Hazen-Dupuit-Darcy (FHDD) equation (1):

(1) $$-\frac{\partial P}{\partial x} = \frac{\mu}{K} v_0 + \rho C v_0^2$$

where, $\partial P/\partial x$ is the pressure gradient across the sample in the direction of flow (Pa m^{-1}), μ is the dynamic viscosity of the working fluid (Pa s), K is the permeability of the sample (m^2), v_0 is the Darcy velocity (flow rate divided by the cross-sectional area of the sample) (m s^{-1}), ρ is the density of the fluid (kg m^{-3}), and C is the form factor of the sample (m^{-1}).[106] Permeability, K, and form factor, C, are geometric parameters of the foam.

Permeability test samples (untreated, partially reticulated, and fully reticulated foams) were cut into 16 x 20 mm (OD x length) cylinders using a resistive wire cutter and biopsy punch. Each sample was slightly compressed to fit into a 30 x 19 x 16 mm (length x OD x ID) poly(methyl methacrylate) (PMMA) tube. UV cure epoxy (Dymax See-Cure 1202-M-SC, Dymax Corporation, Torrington, CT) was applied to the exterior surface of each cylindrical sample using a plastic spatula. Each sample was then placed into the PMMA tube with one end of the cylindrical sample flush with the tube opening. The epoxy was UV cured for 30 sec (OmniCure® S1000, Lumen Dynamics, Canada) to bond the foam to the tube, and samples were stored under desiccation until testing.

Prior to permeability testing, each sample was sonicated in water for 1 hr to remove air bubbles. The pressure drop across each foam sample was measured for at least 30 seconds at flow rates ranging from 0 to 750 mL min-1 (0 to 0.065 m s-1 Darcy velocity) to determine the K and C values of the foam. Each sample was initially measured with two digital 206,800 Pa pressure gauges (model #DPGWB-06, Dwyer Instruments, Michigan City, IN) to determine the peak pressure at maximum flow rate and to select the highest resolution transducer for subsequent tests. Based on these

results, untreated and partially reticulated samples were analyzed using two 206,800 Pa absolute membrane pressure transducers (model #PX42G7-030GV, Omega Engineering, Inc.). Fully reticulated samples were analyzed using 2,482 Pa (model #PX409-10WDWUV, Omega Eningineering, Inc) and 17,240 Pa (model #PX409-2.5DWUV, Omega Engineering, Inc.) differential pressure transducers.

A second-order least squares fit was applied to the pressure gradient versus Darcy velocity data to calculate K and C for each sample using Equation 1 with water at room temperature as the working fluid.

3.2.6 Volumetric expansion

Three cylindrical samples measuring 6 x 5 mm (OD x length) were prepared for each reticulation condition using a biopsy punch and razor blade. The foam samples were threaded axially onto a 200 micron diameter nitinol wire (NDC, Fremont, CA) and loaded into a SC150 Stent Crimper (Machine Solutions, Flagstaff, AZ) preheated to 100°C. The samples were equilibrated for 15 min before being radially compressed. The samples remained constrained until they were cooled back to room temperature. Crimped foam over wire samples were stored under desiccation for a minimum of 24 hours before expansion testing. Samples were mounted within a custom aluminum fixture that held the samples in the same imaging plane as a 12 mm measuring reference. The fixture was submerged in a 37°C water bath and imaged at 1 minute intervals for 15 minutes. Five diameter measurements were made along the length of each sample at each time point using ImageJ analysis software (National Institute of Health, MD, USA).

3.2.7 Static water contact angle

Static water contact angle measurements were made on untreated and plasma treated films (300 Watts for 15 minutes) using a CAM 200 Goniometer (KSV Instruments) and drop volumes of 5 µl. Contact angles were measured at day 0, 7, 14, 21, and 28 post reticulation to examine hydrophobic relaxation of the sample. Three contact angles were measured using a Young/Laplace fitting model on 4 separate films for a total of 12 measurements for each process and time point.

3.2.8 XPS

Untreated polymer films and films exposed to the full plasma reticulation process were prepared for XPS analysis. Plasma treated films were analyzed within 3 hours of plasma treatment. Single scan XPS spectra were acquired using an Omicron ESCA+ system with a Mg X ray source at 150 Watts and a CN10 charge neutralizer. Atomic ratios and C1s deconvolution calculations were calculated using Casa XPS software. Deconvolution caclulations were made using a Marquardt fitting model.

3.2.9 Platelet attachment

Bovine blood was acquired from a slaughterhouse immediately following animal sacrifice. To prevent coagulation, the blood was citrated in a 1 L glass jar with a 9:1 volume ratio of blood to 3.2% sodium citrate solution in phosphate buffered saline (PBS, pH 7.4). All blood studies were completed within 8 hours of animal sacrifice.

Plasma treated (1 and 28 days post-treatment) and untreated films were rinsed three times with PBS and placed in a petri dish with the plasma-treated surface face up. The samples were submerged in citrated whole bovine blood and incubated for 1 hour at

37°C. After removing blood from the petri dish, the samples were rinsed three times with PBS and fixed with 3.7% glutaraldehyde at 37°C for two hours. A total of 16 images were captured for each sample surface condition using a brightfield microscope (Nikon Eclipse TE2000-S) at 40X magnification. Platelets were manually counted within each field of view, and platelet attachment density was calculated using known objective scaling.

3.2.10 Fibrinogen adsorption

The wells of a black 96 well plate were blocked with 5% bovine serum albumin overnight at 4°C. Wells were washed 3 times with phosphate buffered saline (PBS), and laser-cut samples (non-treated control, 0, 7, 14, 21, and 28 day aged plasma-treated) were placed into wells with the treated side face up (n=6). A solution of 1 mg/ml human plasma fibrinogen (Fg) and 0.2 mg/ml Alexafluor 488 Fg conjugate in PBS was added to 3 specimens of each sample type (100 µl). PBS was added to the remaining 3 specimens per sample type. Samples were incubated at 37°C for 2 hr. The Fg solution was removed, and sample surfaces were washed 3 times with PBS. A standard was prepared using a serial dilution of the Fg solution in PBS (1.2 to 0.1875 mg Fg/ml and 0 mg Fg/ml, n=3), and 100 µl of PBS was added to each sample well. Fluorescence intensity was measured (495/519 nm) using a plate reader. A standard curve was prepared from the Fg standard and used to quantify the amount of adsorbed Fg on each sample surface.

3.2.11 AFM

Plasma-induced changes on polymer topography were assessed using a Bruker Dimension Icon AFM in tapping mode. Untreated films and films exposed to the full

plasma reticulation process were imaged at 1 hz with 512 lines per image. Amplitude error images, 3D surface projections, and calculated changes in surface roughness were produced using Nanoscope Analysis software.

3.2.12 Cell spreading

Cell-material interactions were evaluated on plasma-treated (0 and 28 days post treatment) and untreated films. Films (n = 3 per treatment condition) were sterilized under UV light for three hours prior to seeding green fluorescent protein (GFP)-expressing 3T3 fibroblasts (NIH3T3/GFP, Cell Biolabs Inc., USA) on their surfaces at 200 cells mm^{-2}. At set time points (3 hr, 1, 3, and 7 days), cells were imaged using fluorescent microscopy (excitation: 488 nm, Nikon FN1 Upright Microscope, NY, USA). Cell area was quantified using ImageJ software over three images for each film condition with five representative cells measured per image. Cell proliferation was quantified over three images for each film condition using particle analysis in ImageJ with manual verification. Statistical analysis was conducted for the cell spreading and cell density data sets using two-way ANOVA with Bonferroni's multiple comparisons test.

3.3 Results and discussion

3.3.1 Influence of foam morphology on fluid permeability

The plasma-induced changes in foam morphology are clearly visualized via SEM imaging, Figure 3.1. Untreated foams have inter-pore membranes that are still largely intact. The partially reticulated foams have moderate membrane degradation with pinholes in the majority of the membranes, providing a degree of pore interconnectivity

while maintaining a large surface area of membranes for blood-material interactions. Only a small percentage of membranes remain in the fully reticulated foams, while the foam struts remain intact. Full reticulation provides an open porous matrix for improved fluid permeability and cellular infiltration.

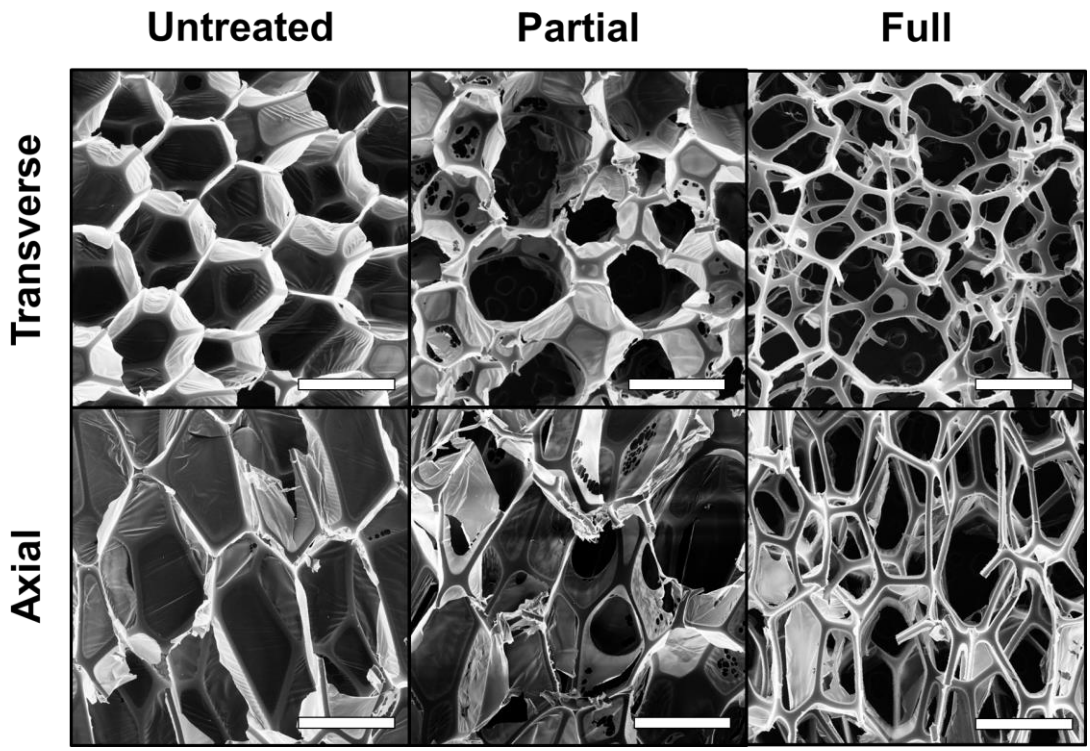

Figure 3.1: SEM images of untreated, partially reticulated (8 min treatment), and fully reticulated (15 min treatment) foams; scale bar is 1 mm.

Figure 3.2 quantifies the increases in material permeability due to plasma reticulation. For each reticulation condition, the permeability data is differentiated based on ramping the fluid velocity up or down to account for hysteresis. Untreated, partially reticulated, and fully reticulated foams had average form factor values of 2.91×10^5 m^{-1}, 1.43×10^5 m^{-1}, and 0.15×10^5 m^{-1}, respectively. Average permeability values for untreated, partially reticulated, and fully reticulated foams were 0.16×10^{-9} m^2, 1.44×10^{-9} m2, and 2.55×10^{-9} m2, respectively. Pressure drops across fully reticulated foams are over 16 times lower than those of untreated foams at Darcy velocities (5-7 cm s^{-1}) that correlate to those typically found in the saphenous vein (7 ± 2 cm s^{-1}).[27] Partially reticulated

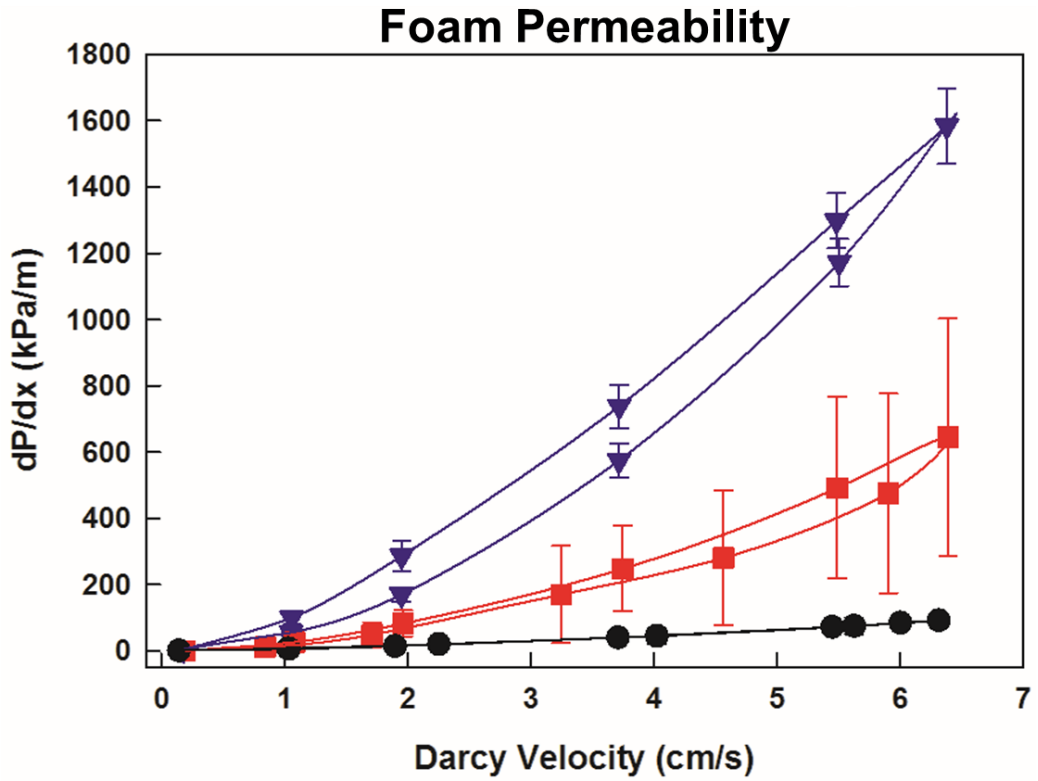

Figure 3.2: Pressure differential measurements across plasma reticulated and untreated foams with increasing and decreasing fluid flow rates; n = 5, mean ± standard deviation.

foam permeability fell between that of untreated and fully reticulated foams, consistent with the degree of observed membrane removal. The pressure gradient standard deviations for partially reticulated foams were significantly higher than those of untreated or fully reticulated foams due to the relative inhomogeneity of the reticulation.

3.3.2 Mechanical testing

Table 3.1 summarizes the tensile mechanical properties of plasma reticulated SMP foams. Increasing reticulation resulted in slight decreases in ultimate tensile stress with full reticulation causing the only statistically significant difference when compared to untreated foam ($p < 0.001$). Strain to failure slightly increased with reticulation, but "2 Partial" was the only reticulation condition determined to be statistically different from the untreated control ($p < 0.05$). Ultimate stress and strain to failure are largely preserved because the foam struts that are left intact after reticulation contribute more to the tensile integrity and overall cross sectional area of the foam when compared to membranes.

Significant decreases in elastic modulus were observed for each reticulation condition ($p < 0.001$). Membrane removal decouples the mechanical link between adjacent foam struts. This affords greater flexibility for each strut and results in an overall decrease in material stiffness. Comparable decreases in elastic modulus were also observed in mechanically reticulated SMP foams.[106]

Table 3.3: Tensile mechanical properties of untreated and plasma reticulated foams (n=5, average ± standard deviation, One-way ANOVA with Bonferroni's multiple comparisons test to untreated control; *p < 0.05, ***p < 0.001).

Plasma Duration [min]	Ultimate Stress [kPa]	Strain at Break [%]	Elastic Modulus [kPa]
0 (Untreated)	106 ± 7	38 ± 6	490 ± 86
1 (Partial)	97 ± 14	42 ± 3	294 ± 62***
2 (Partial)	92 ± 6	46 ± 3*	241 ± 32***
3 (Full)	79 ± 3***	44 ± 4	202 ± 18***

3.3.3 In-vitro shape recovery

As seen in Figure 3.3, unreticulated foam samples had slow expansion rates at 37°C with only 2 mm of expansion after 15 minutes of immersion. By comparison,

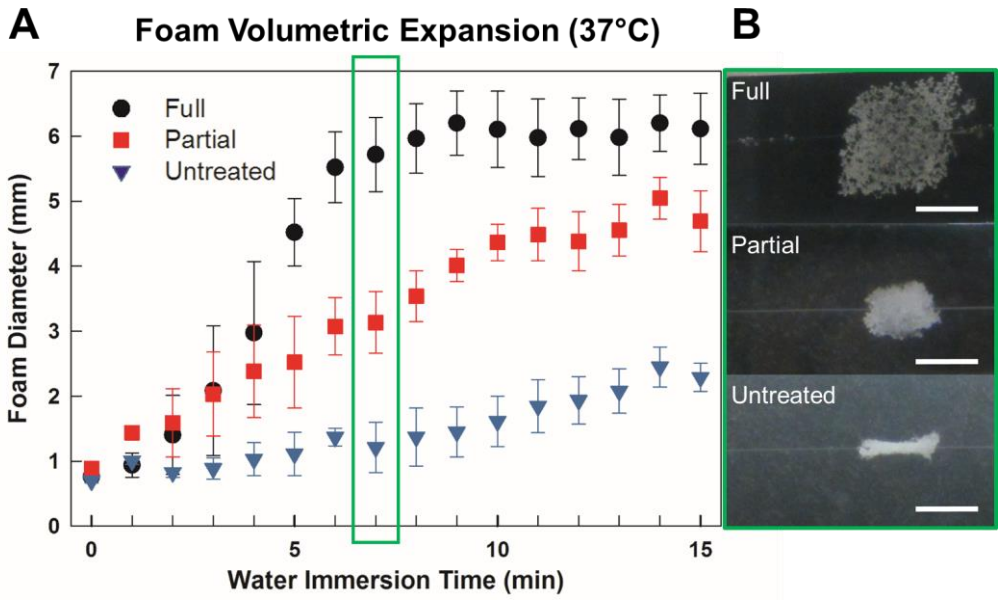

Figure 3.3: A – Unconstrained expansion measurements of plasma reticulated and untreated foam cylinders submerged in 37°C water; n = 15, mean ± standard deviation. B – Still frame images of foams at 7 minutes of immersion. Scale bars are 5 mm.

partially reticulated foams expanded to almost 5 mm in diameter within 15 minutes. Fully reticulated samples achieved full shape recovery (6 mm diameter) in as little as 7 minutes.

These differences in expansion kinetics can be largely attributed to effects on moisture diffusion and moisture-plasticized glass transition temperature (T_g) depression. Actuation of SMP foams via plasticization is a known mechanism.[100, 116] Increased permeability from membrane removal and increased surface hydrophilicity result in faster moisture diffusion throughout the material and a more rapid decrease in T_g, increasing the expansion rate at isothermal body conditions. These changes must be considered during device development to prevent premature foam expansion and excessive device friction within the delivery catheter.

3.3.4 Time-dependent surface hydrophobicity and thrombogenicity

Contact angle measurements were made on plasma treated films to confirm the hypothesis that increased surface hydrophilicity was a driver for increased expansion rates, Figure 3.4. On the day of plasma treatment, films were more hydrophilic with a contact angle of 45 ± 3° compared to untreated films with a contact angle of 96 ± 2°. However, the plasma treated surfaces exhibited hydrophobic recovery with an increased contact angle of 75 ± 4° after four weeks of storage in desiccated air. This partial hydrophobic recovery has been previously reported in polar plasma treatment of polyurethane substrates, and is attributed to surface polar group rearrangement.[92]

Platelet attachment provides an indication of material thrombogenicity. As seen in Figure 3.4, platelet attachment correlated with increased surface hydrophobicity, with

higher platelet attachment to 4 week aged films than to freshly plasma treated films. This result suggests that plasma treated devices intended for embolic applications should be aged prior to delivery to maximize their thrombogenicity.

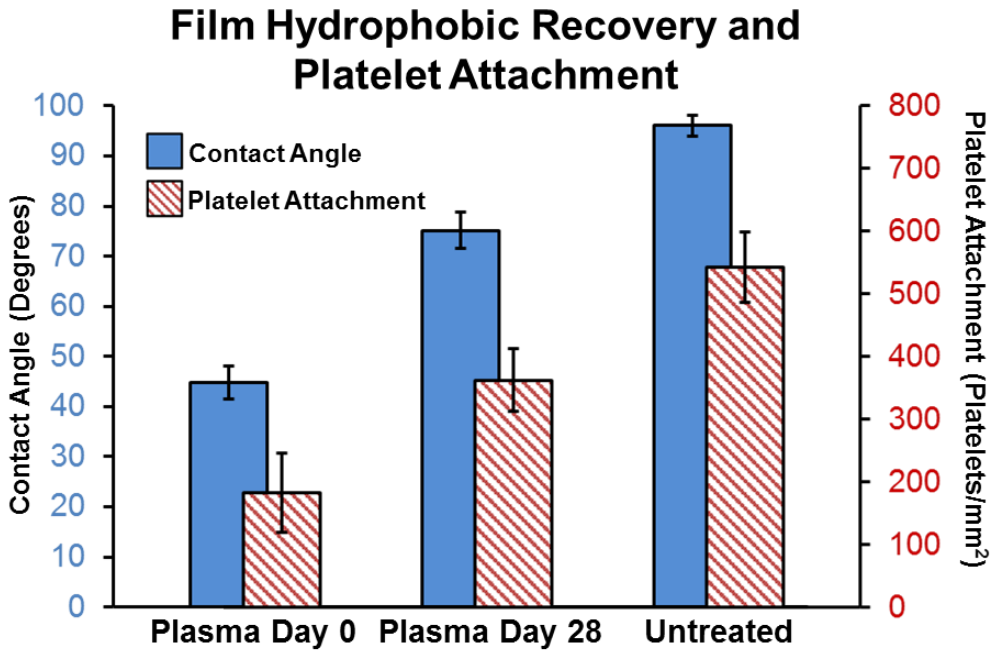

Figure 3.4*:* Water contact angles (n = 12, mean ± standard deviation) and platelet attachment quantification (n = 16 images, mean ± standard error) on SMP films 0 and 28 days post plasma treatment compared with untreated films.

3.3.5 XPS

XPS was used to characterize changes in plasma induced changes in surface oxidation. This technique has higher surface specificity compared to other spectroscopic techniques, such as ATR FTIR, that could not differentiate surface chemistry from the underlying bulk material. As seen in Figure 3.5, changes in surface oxidation could be quantified for untreated 100TMH60 films and films analyzed within

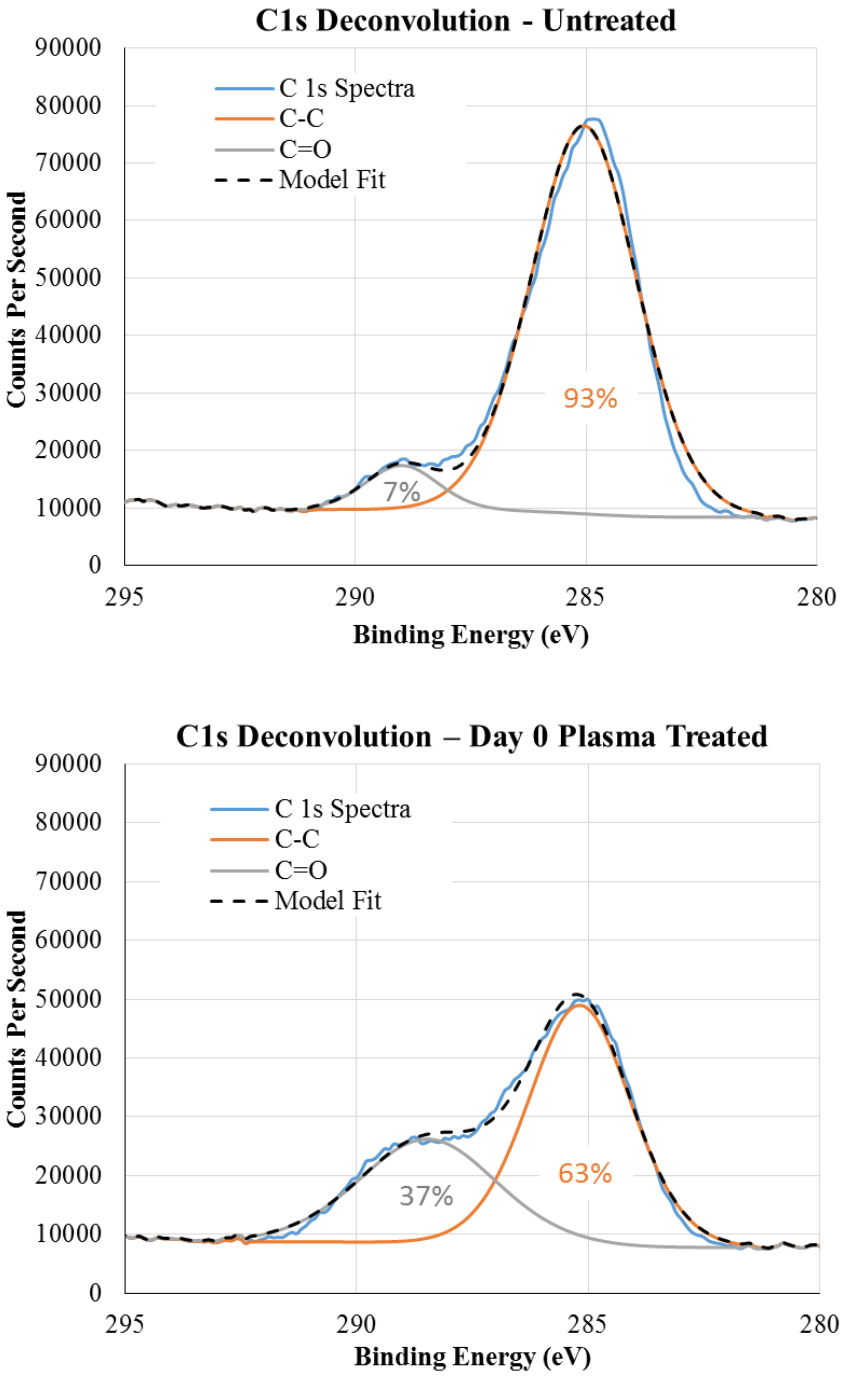

Figure 3.5: Top – C1s deconvolution spectra for an untreated SMP film. Percentages under each curve correspond to the component percentage of the total calculated carbon content. Bottom – C1s deconvolution spectra with carbon component percentages for an SMP film reticulated the same day as analysis.

3 hours of full plasma reticulation treatment. The deconvoluted day 0 spectra had significantly higher carbonyl carbon (C=O) content at 37% when compared to the untreated control with 7% C=O content. This data supports the hypothesis of decreased surface hydrophobicity due to increased surface oxidation.

Atomic ratio calculations in Table 3.2 also support conclusion for plasma induced surface oxidation with surface oxygen content increasing from 63.4% to 77.5%. This XPS analysis also revealed a percentage of Fluorine covalently bound to the polymer surface after CF_4 plasma exposure. Although fluorine peaks could be resolved, there was no discernable C1s peak at 292 or 294 eV related to CF_2 or CF_3, respectively. The increase in nitrogen content is attributed to plasma induced cleaning of the material surface. This cleaning is hypothesized to reduce the adventitious carbon layer that partially convolutes the nitrogen content in the untreated material spectra.[117]

Table 3.2: XPS atomic ratios for untreated and plasma reticulated polymer films

	C 1s %	N 1s %	O 1s %	F 1s %
Untreated	77.5	9.6	12.9	0
Plasma Day 0	63.4	13.4	21.5	1.7

3.3.6 Fibrinogen adsorption

Similar to platelet adhesion, fibrinogen adsorption to the polymer surface provides an indication for material thrombogenicity. Figure 3.6 shows comparable trends when compared to platelet adhesion behavior, with an initial decrease in fibrinogen adsorption at day 0 and a linear increase with increased surface aging after plasma treatment. Initial decreases in surface thrombogenicity and contact activation of the

clotting cascade have been previously reported with polar plasmas.[96, 118] However, the time dependent effect of plasma reticulation on surface thrombogenicity should be carefully considered when plasma reticulating SMP foams for embolic device applications. This data suggests that an aging procedure after plasma treatment could be important for restoring device thrombogenicity.

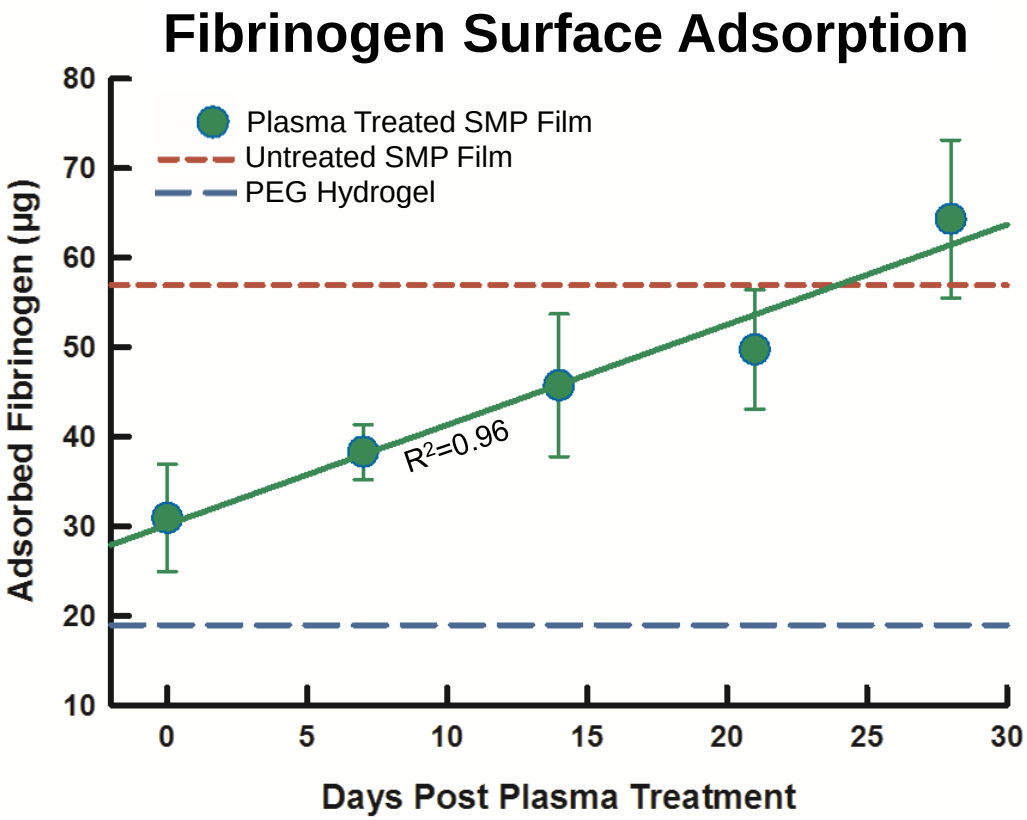

Figure 3.6: **Effects of plasma reticulated surface aging on fluorescent fibrinogen adsorption compared to a PEG hydrogel negative control and untreated SMP positive control, n=3.**

At 28 days, the amount of adsorbed fibrinogen exceeds the positive control level for an untreated SMP films. This result suggests that fibrinogen adsorption could be

dependent on other factors, such as surface morphology, in addition to dynamic changes in surface chemistry and hydrophobicity.

3.3.7 AFM

Quantitative surface morphology images in Figure 3.7 confirm plasma induced changes in physical surface structure and roughness. Comparatively large protrusions on the untreated surface are shortened on the plasma treated sample due to material removal. Although plasma reticulation reduced surface roughness (R_a) from 11.2 nm to 4.8 nm, the number of nanoscale surface protrusions is significantly increased. These features are hypothesized to contribute to the observed fibrinogen adsorption behavior. These features could also influence adsorption of other thrombogenic proteins and subsequent cellular behavior.

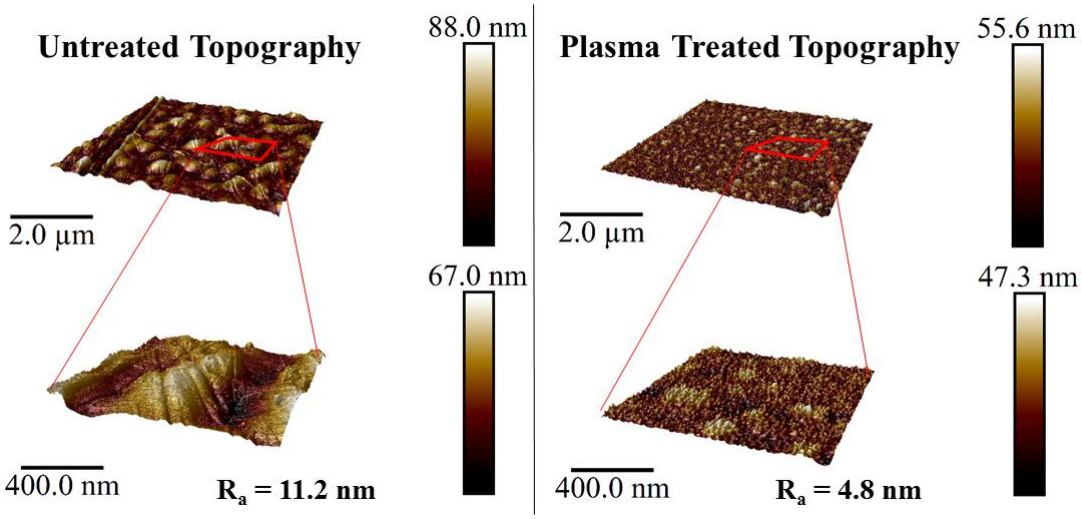

Figure 3.7: Quantitative 3D projections of untreated (left) and plasma reticulated (right) SMP films surfaces with decreased surface roughness.

Qualitative amplitude error images in Figure 3.8 further illustrate plasma induced changes in surface structure. The protrusions in the lower right panel are hypothesized to be urea nanodomains that nucleate during synthesis due to differences in reaction kinetics. The surrounding material is hypothesized to preferentially degrade and leave these domains that are more resistant to oxidative degradation. Similar domains on this size scale have been observed in unpublished TEM images with these materials.

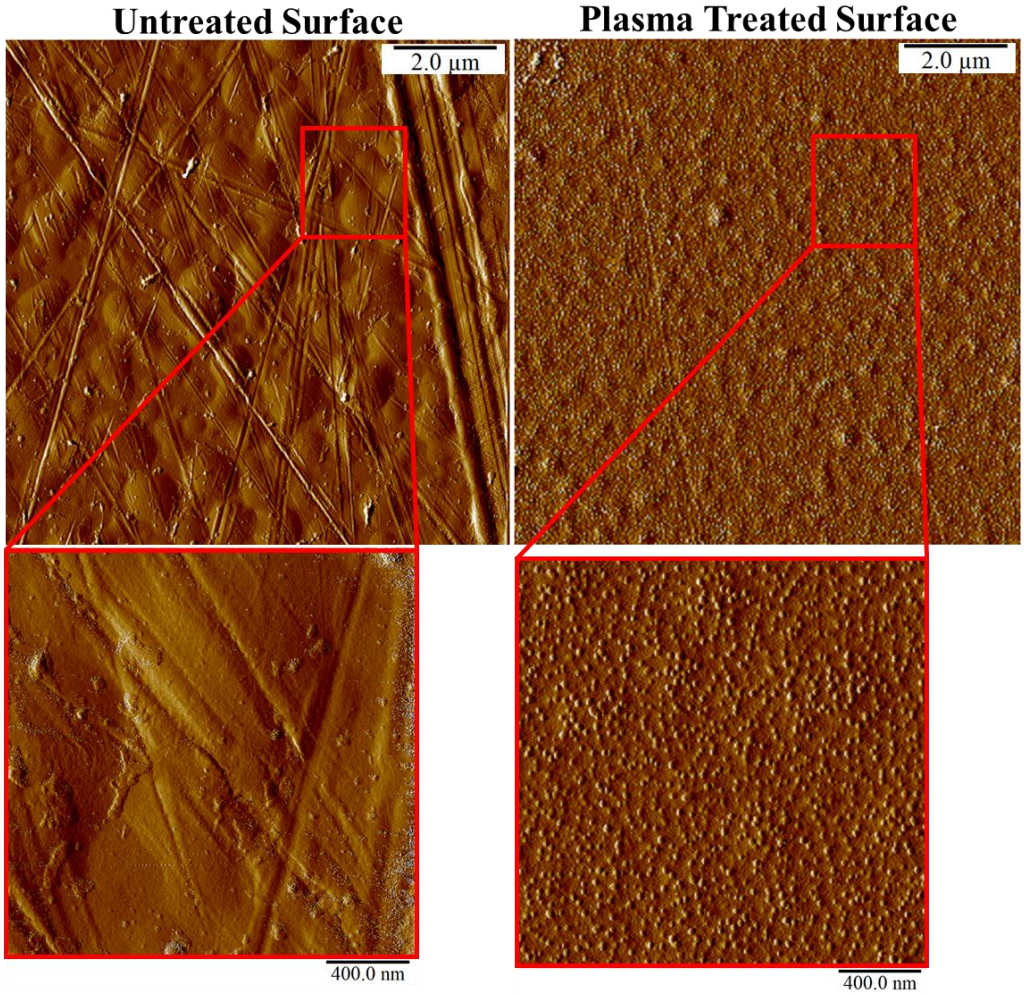

Figure 3.8: Qualitative amplitude error images for untreated (left) and plasma reticulated (right) SMP films with increased nanoscale surface protrusions.

3.3.8 Time-dependent cell responses

Based on cell spreading morphology, cellular affinity to the plasma treated surface is demonstrated in as little as 3 hours after seeding, Figure 3.9A. This initial adhesion enables significantly enhanced cell spreading on the plasma treated substrate at later time points, as seen after a week in vitro. As indicated by Figure 3.9B, the cells on the control film reach a threshold of cell area at ~1 day of culture; however, cells on the plasma-treated surface demonstrate highly extended pseudopodia with consistent increases in cell spreading over a week of culture. Similar fibroblast spreading behavior has been reported for tissue culture polystyrene with a comparable range of surface contact angles 63–68°.[119] The observed decrease in cell spreading after 4 weeks post reticulation is attributed to the temporal hydrophobic recovery of the surface. The increase in cell spreading for both plasma-treated film conditions is hypothesized to be partially attributed to the changes in film topography observed using AFM. Previous reports have shown significant increases in fibroblast spreading and proliferation for surfaces with features down to 13 nm.[120]

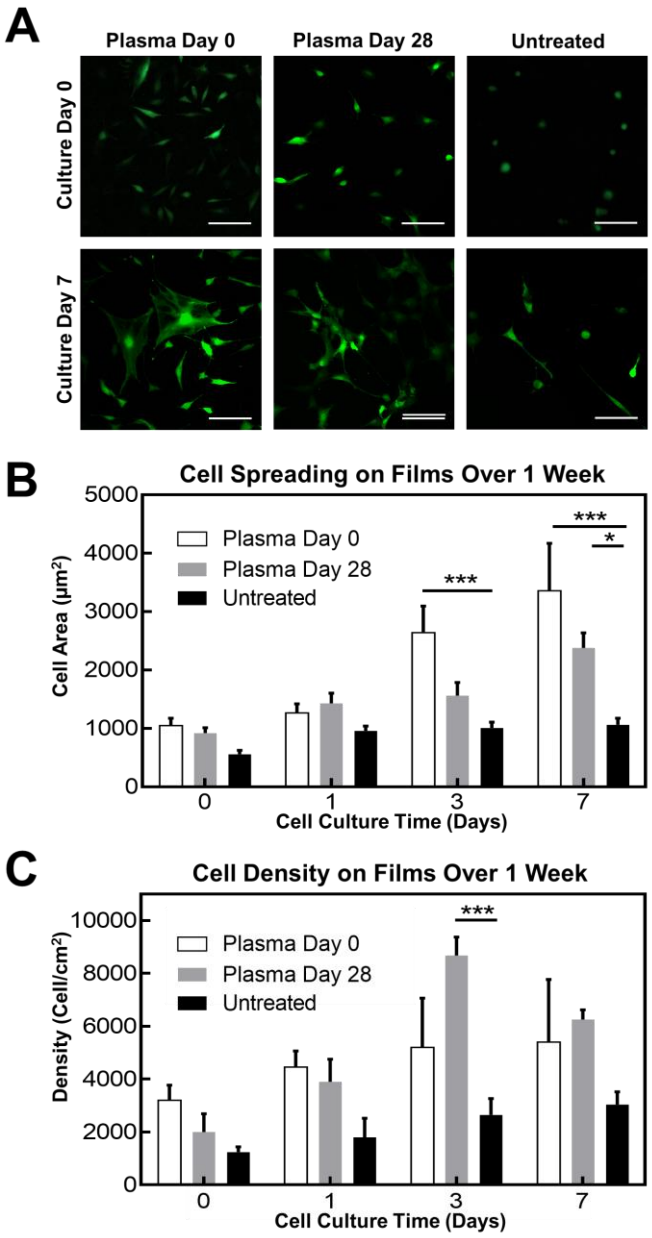

Figure 3.9: A – Fluorescent images of NIH3T3/GFP fibroblasts cultured on SMP films at 0 days and 4 weeks post plasma treatment compared to that on untreated SMP films after 3 hours and 1 week of culture. Scale bar is 100 μm. B – Quantification of cell spreading over 1 week of culture on SMP films. n = 5 cells, 3 images per condition for a total of 15 measurements; mean ± standard error; Two-way ANOVA with Bonferroni's multiple comparisons test; *p < 0.05 relative to untreated control; ***p < 0.001 relative to untreated control. C – Quantification of cell density over 1 week of culture on SMP films. 3 images per condition; mean ± standard error; ***p < 0.001 relative to untreated control.

When compared to the untreated films, both plasma-treated film conditions demonstrated higher average cell densities, especially at the later culture time points of 3 and 7 days, Figure 3.9C. However, only the 3rd culture day "Plasma Day 28" sample showed a statistically significant difference ($p < 0.001$). Temporal changes in surface hydrophobicity did not have the same effect on cell proliferation as cell spreading. Overall, the apparent surface affinity of the plasma-treated film and interconnected porous morphology of the reticulated foam indicate the promise of these materials as embolic tissue scaffolds.

3.4 Conclusions

This work demonstrates control of bulk SMP embolic foam properties, including fluid permeability and volumetric expansion rate, using cold gas plasma reticulation. Observed surface effects are transient and demonstrate a tendency to recover toward baseline hydrophobicity over the course of several weeks. This surface relaxation has significant ramifications for device performance and should be considered in terms of specific device applications, packaging conditions, sterilization techniques, and shelf life. Overall, plasma treatment increases pore interconnectivity and does not appear to impart deleterious effects on cell-material interactions, indicating its utility for developing embolic tissue scaffolds. Furthermore, control over the pore interconnectivity and surface area to volume ratios of porous materials make this process useful for optimizing embolic medical device performance.

CHAPTER IV

CHEMICALLY MODIFIED SHAPE MEMORY POLYMER EMBOLIC FOAMS WITH INCREASED X-RAY VISUALIZATION

4.1 Introduction

The Biomedical Device Lab (BDL) has fabricated ultra-low density SMP foams with mass densities as low as 0.015 g cm^{-3} and high crosslink densities that facilitate 97% shape recovery. These properties collectively enable 70X foam volumetric expansion.[3] Utilization of these low density SMP foams in conjunction with current coiling techniques can significantly reduce the number of coils necessary to fill an aneurysm to reduce procedure time and cost. Additionally, SMP foam expansion forces are significantly lower than those applied by bare platinum coils (BPCs), lowering the risk of aneurysm dissection during implantation.[121] Similar to other coil-based embolization devices, the embolic foam occludes the aneurysm by disrupting blood flow and inducing clot formation within the foam.

Many medical applications for SMPs involve endovascular delivery while imaging with fluoroscopy. Fluoroscopic device visualization is essential for the proper and safe placement of the device into the aneurysm anatomy. In the case of cerebral aneurysm embolization, the lack of SMP x-ray contrast can be partially addressed by utilizing the SMPs as a coating over a radiodense BPC. Figure 4.1 highlights a limitation to this approach. The lefthand frame depicts the typical anatomy of a porcine sidewall aneurysm model. The middle frame shows digital subtraction angiography of an

aneurysm treated with traditional BPCs, which depicts the dense 2D projection of the coil mass that clinicians use as the primary indicator of sufficient coiling. Although the aneurysm appears to be densely packed with coils, the average packing density of embolic coils ranges between 30-35%.[51] The right hand frame shows an aneurysm treated with SMP foam-coated embolic coils.[1] The aneurysm appears to be loosely-filled according to the radiographic projection, but the limited ingress of injected contrast agent proves that the interstitial spaces between the coils are filled with non-x-ray visible embolic foam and thrombus. Using injected contrast agent as the primary indicator of aneurysm embolization is a hurdle for clinical adoption of the device, as it deviates from the standard 2D radiographic projection technique. This procedural change could potentially lead to over-packing the aneurysm with foam coated coils. The proposed x-ray visible SMP formulation is intended to reduce the risk of these complications by giving clinicians a better visual for true volumetric occlusion.

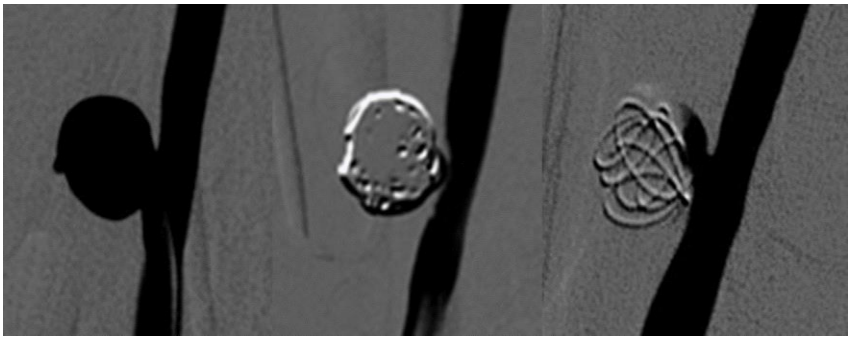

Figure 4.1: Left- Untreated porcine sidewall aneurysm model. Middle – Digital subtraction angiography of aneurysm model treated with bare platinum coils. Ingress of the contrast agent injection is masked by the 2D coil projection. Right – Angiography image of aneurysm treated with SMP foam-coated embolic coils. Ingress of the contrast injection into the aneurysm is prevented by a mass of embolic foam and thrombus.

Previously, SMP foam x-ray visibility has been increased through the incorporation of tungsten microparticles into the foam matrix.[122] However, this approach results in composites with diminished toughness, which raises concerns over particulate generation in vivo and subsequent emboli in the blood stream. Furthermore, the degree of opacification achieved with microparticle incorporation is not sufficient for small-diameter, low density devices, such as those used for neurovascular embolization. Radiopaque nanoparticulate additives were investigated to address decreases in material toughness by increasing dispersion within the polymer matrix. Low concentrations of nanoparticulates improved mechanical strength and toughness, but increasing filler concentration to that needed for sufficient x-ray visualization also resulted in diminished mechanical properties.[2, 102] Thus, there is a need for improved SMP x-ray contrast without sacrificing mechanical integrity.

As an alternative to opaque SMP micro or nanocomposites, this work incorporates iodine motifs into the polymer matrix to increase x-ray visibility without affecting the bulk foam properties. The most typical iodine functional group used in biomedical applications is the triiodobenzene ring, which is used in all commercial fluoroscopy contrast agents to achieve iodine solution concentrations in the range of 150–300 milligrams of iodine per milliliter (mg I/ml).[123, 124] Although triiodobenzene motifs have been proposed as pendant groups for thermoplastic polymers, development of a thermoset biomedical SMP foam system that incorporates commercially available contrast agents as monomers is novel.[125]

When compared to particulate additives, the chemical approach of incorporating triidobenzene monomers into the material during synthesis was hypothesized to enable higher contrast loading percentages without affecting the mechanical integrity of the bulk material. This radiodense SMP material system can be utilized to create low density foams for embolic applications without the need for metal components such as platinum backbones or marker bands. This material system could set the stage for entirely polymeric, degradable, embolic devices used for a variety of applications, including cerebrovascular or peripheral embolization. While this work focuses on the incorporation of iodine into a specific SMP foam system, the information gained here could be applied to a range of polymeric biomaterials to enable their imaging during implantation.

Figure 4.2 shows proof of concept results for combining radiographic contrast agents with shape memory polymer foam for x-ray visualization. These 2.5 mm diameter foam cylinders were solvent swelled with solutions of iohexol dissolved in ethanol and vacuum dried. The expanded foams were imaged through a porcine skull with traditional fluoroscopy. These composites showed comparable visualization to a commercial GDC10 embolic coil. Although visible, physical incorporation of iohexol produced undesirable mechanical properties comparable to a ceramic material, further motivating chemical incorporation of triiodobenzene into the polymer backbone.

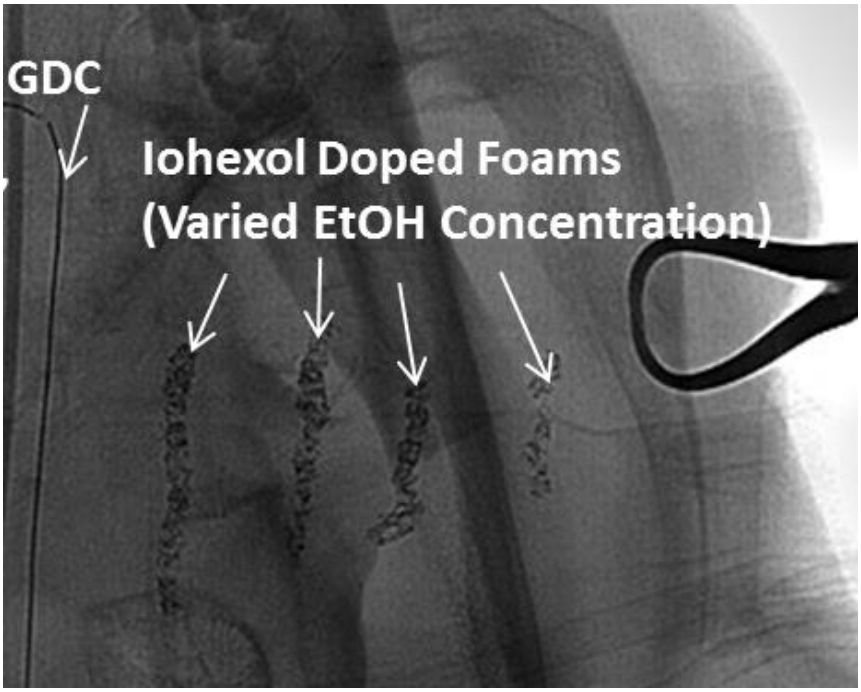

Figure 4.2: 2.5 mm foam devices and a GDC platinum coil imaged through a porcine skull. Iohexol was solvent swelled into the foam with ethanol solutions at 10–40 wt%.

Figure 4.3 depicts the monomers selected to investigate an x-ray visible SMP system. Aliphatic isocyanates were chosen for a polyurethane composition based on previous SMP compositions with demonstrated biocompatibility in embolic applications.[4, 16] Changing the molar ratio of hexamethylene diisocyanate (HDI) and trimethyl hexamethylene diisocyanate was hypothesized to control T_g and bulk material hydrophobicity for tailored material expansion rate.[99]

The proposed contrast agent monomer is 5-amino-2,4,6-triiodoisophthalic acid (ATIPA). The x-ray contrast of the ATIPA molecule is derived from the triiodobenzene motif, which incorporates three high-z iodine atoms. It is terminated with a primary aromatic amine and two carboxylic acids, giving it a functionality of three for

crosslinking reactions with isocyanates. Further, the reaction between isocyanates and carboxylic acids yields an amide linkage and carbon dioxide, making ATIPA a chemical blowing agent during foam polymerization.[126]

Solubility was a significant barrier for the development of this system. ATIPA is a hydrophilic solid monomer with negligible solubility in isocyanates. ATIPA is soluble in tetrahydrofuran and dimethylsulfoxide, but a solvent-free synthetic procedure is preferable to mitigate organic contaminants in end use medical products. The proposed polyols 2-butyl-2-ethyl propandiol (BEP), 3-methyl-1,5-pentanediol (MPD), diethylene glycol (DEG), triethylene glycol (TEG), 1,2,4-butane triol (BT) and 1,2,6-Hexane triol (HT) were selected based on favorable ATIPA solubility and T_g control in the final material.

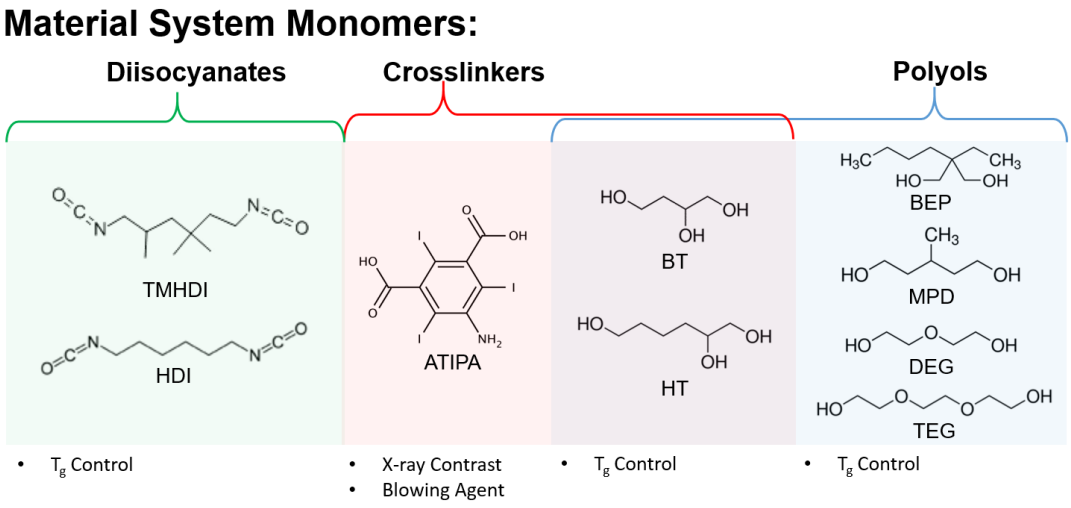

Figure 4.3: Investigated monomers for x-ray visible SMP development.

Figure 4.4 depicts an additional solubility hurdle with these materials. Although the premix resins demonstrated favorable solubility, the final material exhibited considerable phase separation. ATIPA precipitation was predominantly seen during the addition of tertiary amine blowing catalysts. This type of precipitation was also seen with early material development with the polyol crosslinking monomers HPED and TEA. It was concluded that tertiary amines caused ATIPA to precipitate out of solution and should be avoided. Even without traditional polyurethane foaming catalysts, the reactivity of ATIPA does not lead to significant adverse effects when foaming the material.

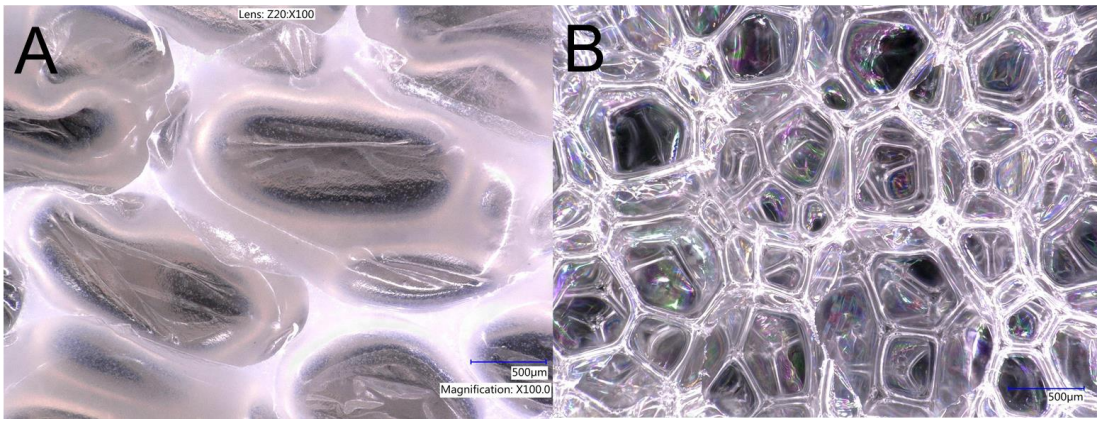

Figure 4.4: A – Phase separated, cloudy foam with 20 eq% ATIPA synthesized with tertiary amine blowing catalyst. B – Optically clear foam with 30 eq% ATIPA synthesized without traditional foaming catalysts.

Preliminary proof of concept materials that incorporate DEG and TEG are summarized in the accepted publication by Ezell et al in the ASME Journal of Medical Devices. However, the focus of this chapter is on the optimization of a system utilizing HDI, TMHDI, ATIPA, BEP, MPD, and HT. MPD was proposed to replace TEG and

DEG to mitigate the risk of degradation product biocompatibility by creating a theoretically more biodurable aliphatic system that does not incorporate ether linkages that are susceptible to oxidative degradation.

4.2 Materials and methods

4.2.1 Foam synthesis

Table 4.1 summarizes all foam compositions that were synthesized. For the A side of the polyurethane synthesis, the reactive hydroxyl, amine, and carboxylic acid functional groups are considered for the eq% calculations. A 2% molar excess of isocyanate was added to each foam synthesis to account for ambient moisture contamination during foam mixing. HDI, TMHDI, BEP, MPD, ATIPA, and HT were used as received from VWR Scientific and Sigma Aldrich.

Figure 4.5 provides an overview of the ATIPA foaming protocol. In summary, hydroxyl (OH) premixes were prepared 1 day prior to foaming by combining a 0.6 equivalent ratio of non-isocyanate monomers (ATIPA, BEP, MPD, HT) to a 15 ml polypropylene flactek mixing cup. The contents were mixed for 30 seconds at 3400 rpm in a flactek high speed shear mixer, heated at 50°C for 1 hour, mixed again for 30 seconds at 3400 rpm, and heated overnight at 50°C. For the 30 and 40 eq% ATIPA composition, 5 wt% and 8 wt% anhydrous THF were added to the OH premix to achieve complete solubility.

Table 4.1: Investigated ATIPA foam compositions. *5 wt% THF addition. **8wt% THF addition.

	Foam ID	ATIPA%	MPD%	BEP%	HT%	NCO	Enovate	Scale
1	0.0 ml Eno - 20AT	20	40	20	20	HDI	0 ml	8g
2	0.5 ml Eno - 20AT	20	40	20	20	HDI	0.5 ml	8g
3	1.0 ml Eno - 20AT	20	40	20	20	HDI	1.0 ml	8g
4	1.5 ml Eno - 20AT	20	40	20	20	HDI	1.5 ml	8g
5	2.0 ml Eno - 20AT	20	40	20	20	HDI	2.0 ml	8g
6	10HT – 20AT	20	50	20	10	HDI	1.5 ml	8g
7	20HT – 20AT	20	40	20	20	HDI	1.5 ml	8g
8	30HT – 20AT	20	30	20	30	HDI	1.5 ml	8g
9	40HT – 20AT	20	20	20	40	HDI	1.5 ml	8g
10	0AT – 40HT	0	40	20	40	HDI	1.5 ml	8g
11	10AT – 30HT	10	40	20	30	HDI	2.0 ml	8g
12	20AT – 20HT	20	40	20	20	HDI	1.5 ml	8g
13	30AT – 10HT*	30	40	20	10	HDI	1.0 ml	8g
14	40AT – 0HT**	40	40	20	0	HDI	1.0 ml	8g
15	20AT HDI	20	40	20	20	HDI	1.5 ml	8g
16	20AT 50H/50TM	20	40	20	20	50/50	1.5 ml	8g
17	20AT TM	20	20	20	20	TMHDI	1.5 ml	8g
18	25AT 32g	25	40	20	25	HDI	1.5 ml	32g
19	30AT 32g*	30	40	20	20	HDI	1.5 ml	32g

Viscous isocyanate (NCO) premixes were prepared in a desiccated glovebox by adding 0.4 molar ratio of reactive polyol equivalents to the entirety of diisocyanate equivalents in a 150 ml polypropylene flactek mixing cup. Contents were mixed at 3400 rpm for ten minutes until a single phase was achieved. This premix was shaken at 1 rpm at room temperature for 2–5 hours until the mixture achieved a room temperature viscosity comparable to honey. For the 0AT composition, 0.04 g of Air Products T131 gelling catalyst and 0.08 g of Air products BL22 blowing catalyst were added to increase the reaction rate during foaming.

To stabilize the foam during blowing, 4 wt% DCI990 surfactant was added to the NCO premix and mixed for 30 seconds. The OH premix was added to the NCO premix and mixed for 30 seconds. 1–2 ml of Enovate was immediately added to the reactive resin and mixed for 30 seconds. The reaction was immediately moved to a 90°C oven for a 20-minute cure. After curing, the foam skin was removed with a razor, and the foam was post cured at 50°C for 12 hours. Post-cured foams were cubed and stored in desiccated polypropylene bags.

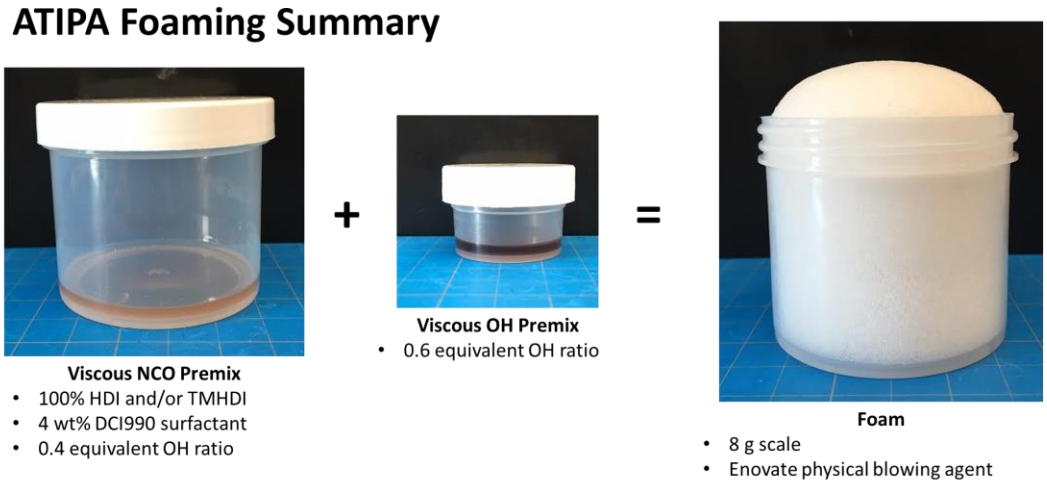

Figure 4.5: ATIPA foaming process summary.

4.2.2 Physical characterization

Pore sizes were determined from light microscopy images acquired at 50X and 100X magnification using a Keyence VHX-5000 metrology system with a variable illumination adapter. Foam samples were cut into 2–4 mm slices in the axial and transverse planes. Ten pore diameter measurements were taken for each foam image.

Six cubes measuring approximately 1 cm^3 were taken from each composition for density measurement. Density was calculated as the sample mass divided by the product of the length, width, and height of the sample.

4.2.3 Fluoroscopy

Foam samples were prepared for x-ray imaging by cutting 1cm x 1cm samples into 8, 4, 2, and 1 mm thick slices and adhering them to a polypropylene sheet. Each foam array included a platinum embolic coil as a radiographic standard. Peripheral occlusion prototypes were prepared by cutting foams into 8 mm diameter cylinders and axially threading them over a 0.006" stainless steel wire. One prototype was imaged in the expanded state while the other was radially crimped using a machine solutions SC250 heated stent crimper. The sample was equilibrated at 100°C in the crimping bore for 15 minutes, radially compressed, and constrained while cooling to ambient temperature. Neurovascular prototypes 2 mm in diameter and without a backbone wire were also prepared and radially crimped. Angiography and fluoroscopy images were acquired using a Philips Allura Xper FD20 x-ray system.

4.2.4 DSC

Dry T_g was determined using a TA Q200 Differential Scanning Calorimeter on 5–10 mg foam samples in a vented aluminum pan. The samples were equilibrated at -40°C for 5 minutes, then heated to 120°C, cooled to -40°C, and reheated to 120°C at temperature ramps of 10°C/min. T_g was calculated as the inflection point of the second heating curve.

Wet T_g foam samples were immersed in 50°C water for 30 minutes to achieve moisture plasticization. Moisture was removed by compressing the foam between tissue paper at 2 tons for 30 seconds using a Carver laboratory press. 5–10 mg foam samples were added to an aluminum pan and hermetically sealed. Samples were cooled to -40°C, equilibrated for 5 minutes, and heated to 100°C at 10°C/min. Wet T_g was calculated from the heating curve inflection point.

4.2.5 DMA

Dynamic mechanical analysis was conducted using a TA Q800 Dynamic Mechanical Analyzer. Foam cylinders were prepared with an 8 mm biopsy punch and cut to approximately 5 mm in length using a razor. Samples were equilibrated to 0°C for 5 minutes and heated to 120°C at 3°C/min while undergoing 40 µm deformation at 1 Hz.

4.2.6 Unconstrained expansion

Foams with varying HT content were cut into 2 mm diameter cylinders and axially threaded over 0.006" stainless steel wires. Samples were radially compressed using a Machine Solutions SC250 heated stent crimper. Crimped samples were allowed to relax 24 hrs before being expanded in a 37°C water bath. Samples were imaged at 5-minute intervals for a total of 45 minutes. Five diameter measurements were taken along the length of the expanding foam using ImageJ software.

4.2.7 ATR FTIR

ATR FTIR spectra were obtained using a Bruker ALPHA Infrared Spectrometer with a diamond ATR crystal. Data analysis was conducted using Bruker OPUS Spectroscopy software.

4.2.8 Tensile testing

Dry foam samples were prepared using an ASTM Type IV dog bone punch. Uniaxial tensile tests were conducted at room temperature using an MTS Insight 30 Material Tester with a constant strain rate of 50 mm/min. Ultimate tensile strength (kPa), strain at break (%), and elastic modulus (kPa) were calculated from the stress-strain curve of each sample.

4.2.9 Gel fraction

Foam samples measuring approximately 1 cubic centimeter were cleaned to remove residual surfactant using three 30-minute sonication intervals in isopropyl alcohol at a 20:1 dilution ratio. The samples were dried under vacuum at 100°C for 12 hours. Dried foam samples were massed and added to 20 ml vials filled to the shoulder with THF and heated at 50°C with 1 Hz oscillation for 48 hours. The THF was removed, and samples were dried under vacuum at 70°C for 36 hours. Gel fraction is reported as the final sample mass divided by the original sample mass.

4.3 Results and discussion

Physical and thermomechanical properties for all foam compositions are summarized in Table 4.2. Each foam series is grouped together and named after the variable altered in the synthetic procedure.

Table 4.2: Physical and thermomechanical ATIPA foam properties.

	Composition	Density (g/cc) n=6	Axial Pore Size (µm) n=10	Transverse Pore Size (µm) n=10	Dry T_g (°C) n=3	Gel Fraction (%) n=5
1	0.0 ml Eno	0.228±0.011	617±243	574±277	46.8±0.5	-
2	0.5 ml Eno	0.149±0.013	1039±523	845±370	44±2.3	-
3	1.0 ml Eno	0.075±0.001	856±321	974±502	47±0.4	-
4	1.5 ml Eno	0.057±0.001	293±102	306±115	45±1.2	-
5	2.0 ml Eno	0.045±0.004	401±158	332±126	44±0.7	-
6	10HT – 20AT	0.051±0.001	402±191	311±112	41±1.0	94.5±2.5
7	20HT – 20AT	0.057±0.001	293±102	306±115	45±1.2	95.1±0.6
8	30HT – 20AT	0.051±0.001	384±152	364±190	53±2.1	96.9±0.5
9	40HT – 20AT	0.044±0.001	372±161	434±243	58±2.1	99±0.4
10	0AT – 40HT	0.078±0.003	231±120	233±123	38±0.1	95.8±3.9
11	10AT – 30HT	0.062±0.009	1360±723	1130±399	37±0.4	98.7±0.7
12	20AT – 20HT	0.057±0.001	293±102	306±115	45±1.2	95.1±0.6
13	30AT – 10HT	0.041±0.005	558±346	579±238	52±1.5	96.4±0.6
15	100HDI	0.057±0.001	293±102	306±115	45±1.2	-
16	50HDI/50TM	0.049±0.002	517±314	482±287	50±0.5	-
17	100TM	0.049±0.001	552±214	488±274	52±0.5	-
18	25AT 25HT 32g	0.040±0.001	515±119	512±249	-	-
19	30AT 20HT 32g	0.051±0.005	415±172	320±137	-	-

For compositions 1–5 with varying volumes of Enovate (Eno), there is an obvious trend of decreasing material density with increasing volume of physical blowing agent. Although there is a statistically significant difference in the dry T_g values (1 way ANOVA, α=0.05), this variation is not expected to significantly affect device design

criteria. The relationship between material density and pore morphology is better illustrated in light microscopy images presented in the next section.

Compositions 6–9 with varying hexanetriol (HT) content have comparable density and consistent average pore diameters ranging between 300–400 μm. There is a statistically significant difference between the dry T_gs for each composition (1 way ANOVA, α=0.01). As seen in the gel fraction data, increasing HT content increases the material crosslink density. Decreasing the molecular weight between crosslinks leads to higher network rigidity and higher glass transition temperatures. These compositions demonstrated that HT composition is an effective way to control T_g at fixed contrast agent loading (20% ATIPA) and foam density.

The ATIPA content was varied for compositions 10–13. HT content was also changed to maintain a consistent theoretical crosslink density. These foams demonstrated decreased bulk density with increasing ATIPA content. This result is expected due to the blowing reaction generated by the two carboxylic acid groups present on the ATIPA monomer. Dry T_g increases with increasing ATIPA content. Although the theoretical crosslink density for these compositions is constant, the aromatic structure of ATIPA is more rigid than the aliphatic HT monomer, increasing network rigidity and glass transition temperatures.

Compositions 15–17 all have 20 eq% ATIPA with varying isocyanate content. Changing the isocyanate composition demonstrated a less significant effect on T_g than altered HT content. Although foams with increased TMHDI content were successfully

fabricated, they were qualitatively less tough compared to HDI foams and were not selected for further device optimization.

Average gel fractions for selected compositions ranged between 94.5–99.0%. These values are comparable to those reported in previous non-visible SMP foam formulations.[3] High gel fractions reduce the risk for complications related to leachable chemicals exiting a permanently implanted biomaterial. If necessary, this risk could be further mitigated with a more rigorous foam cleaning protocol to remove any potential unreacted leachables prior to device implantation.

After characterizing foams 1–17, compositions 18 and 19 were fabricated at 4x scale for tensile testing and neurovascular prototype fabrication. These compositions incorporated chemistry changes to achieve desirable morphology and thermomechanical properties.

4.3.1 Light microscopy

Figure 4.6 illustrates the impact that increasing blowing agent has on foam morphology. The “0 ml” composition that uses no physical blowing agent still has porosity due to the ATIPA blowing reaction. Although these pores are comparable in size to the 0.5 ml and 1.0 ml foams, the thick strut morphology explains the significant difference in bulk material density. Similarly, the smaller pores in the 1.5 ml and 2.0 ml foam yield the least dense materials due to thin strut structures.

Figure 4.7 depicts foams with varying HT composition with comparable pore size, density, and strut morphology. It is important to note that composition and subsequent thermomechanical properties can be altered independent of foam

morphology to enable material optimization toward target medical device applications. Using both chemical ATIPA blowing and physical blowing enables morphology control independent of composition.

The foams in Figure 4.8 have significant differences in pore morphology because the foaming parameters (premix OH ratio, premix cure time, premix viscosity, etc.) were not adequately altered to compensate for changes in ATIPA content. However, this series demonstrated miscibility up to 30 eq% ATIPA. It is important to note that the 30 eq% ATIPA composition required 8 wt% of anhydrous THF during synthesis to prevent ATIPA precipitation.

Figure 4.9 details foams with varying isocyanate content. All foams demonstrate qualitative optical clarity. This promising monomer miscibility makes isocyanate composition a promising variable to control bulk thermomechanical properties and hydrophobicity for tailored material performance.

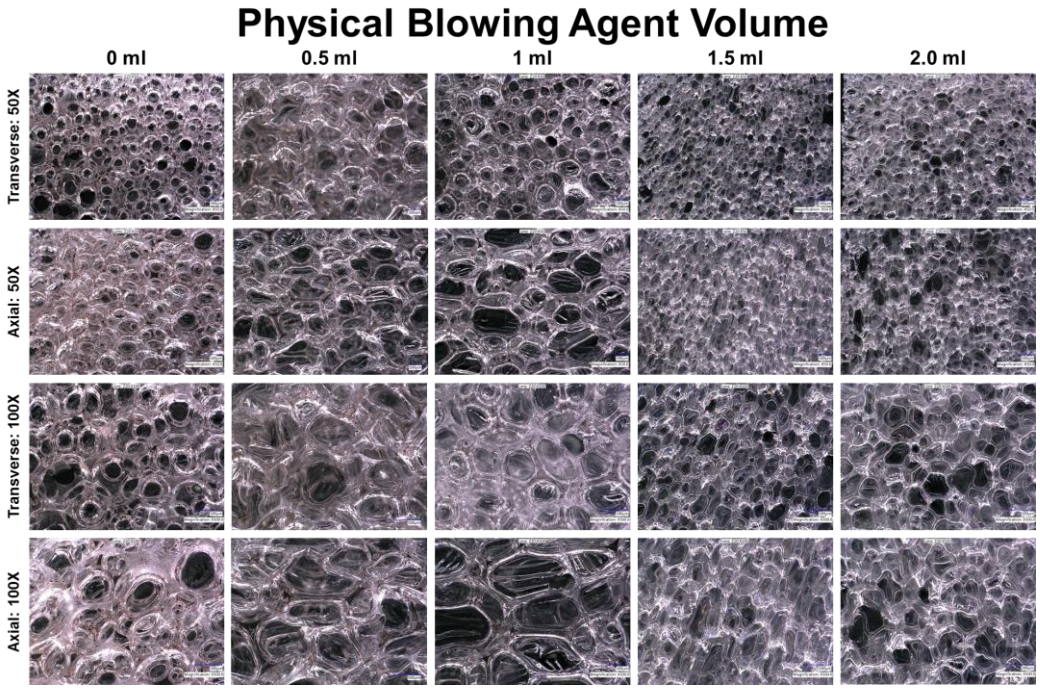

Figure 4.6: Microscopy images at 50X and 100X magnification for an ATIPA foam series varying physical blowing agent (Enovate) volume.

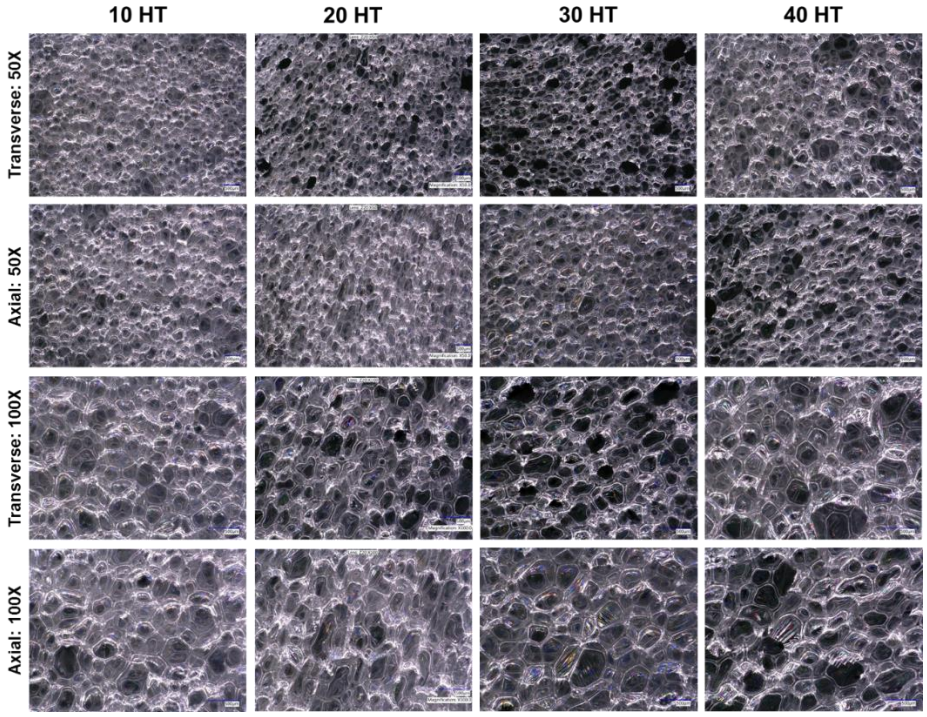

Figure 4.7: Microscopy images at 50X and 100X magnification for foams with 20 eq% ATIPA and varying hexanetriol composition.

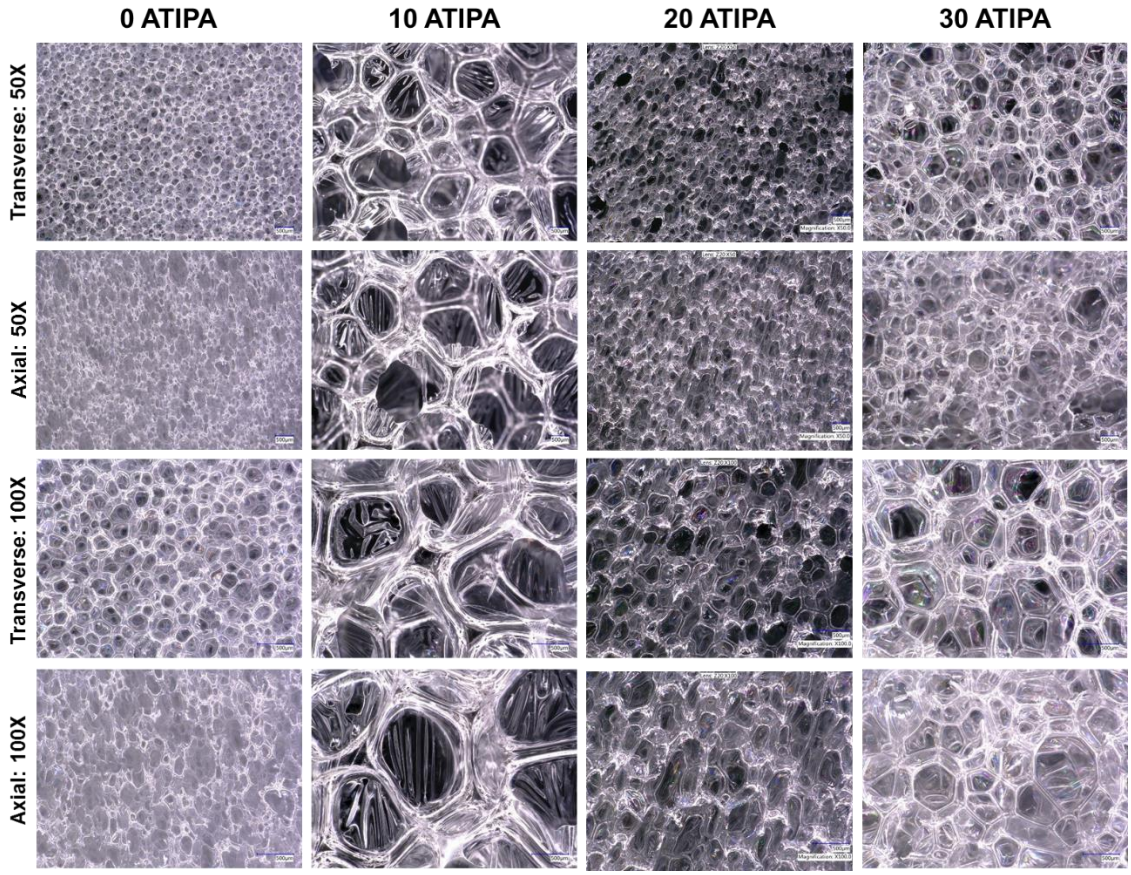

Figure 4.8: Microscopy images at 50X and 100X magnification for foams with varying ATIPA content.

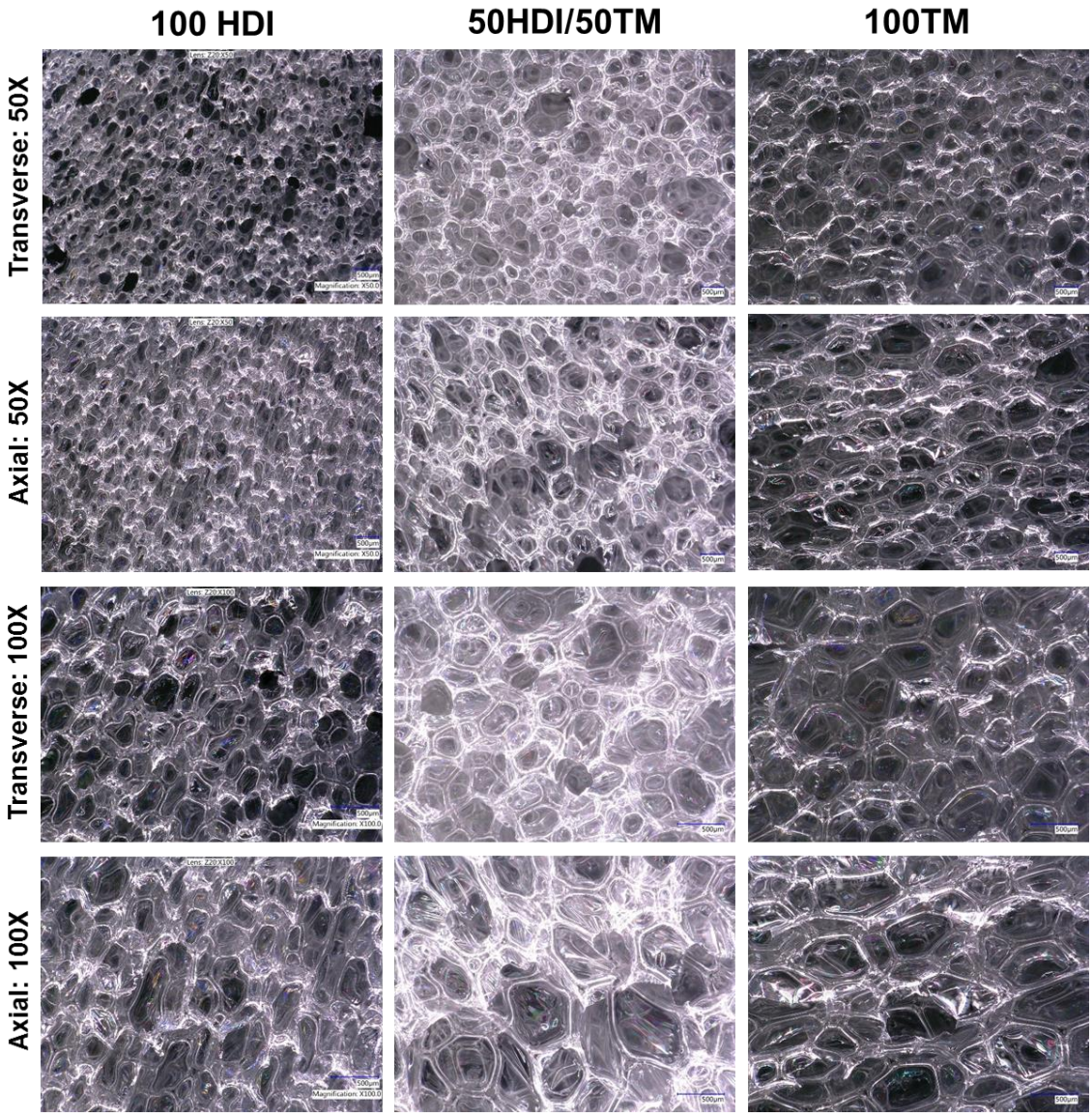

Figure 4.9: Microscopy images at 50X magnification for ATIPA foam series varying isocyanate composition.

4.3.2 Tensile testing

Figure 4.10 shows representative stress vs strain curves and affiliated calculations for a non-visible SMP foam, a 6 volume percent tungsten loaded SMP

composite (6 vol% W), a 25 eq% ATIPA foam, and a 30 eq% ATIPA foam (compositions 18 and 19).[1, 2, 127]

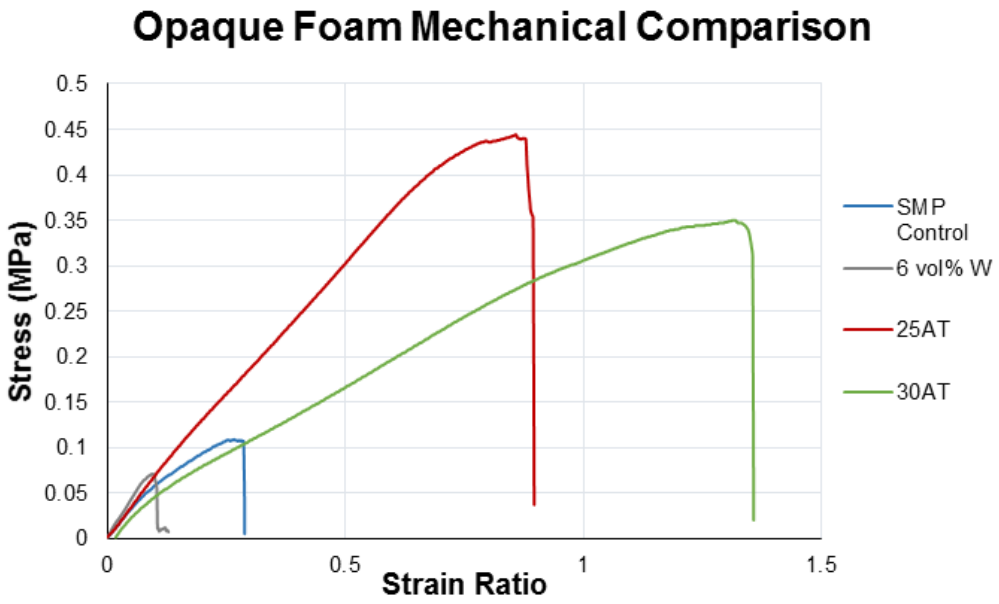

	Peak Stress (kPa)	Strain at Break (%)	Toughness (kJ/m3)
SMP Control	109	29	20
6 vol% W	71	13	5
25AT	444	86	234
30AT	350	132	285

Figure 4.10: Top – representative stress-strain curves for x-ray visible foams (ATIPA and Tungsten loaded) and a non-visible control foam. Bottom – mechanical property calculations from each curve.[1, 2]

ATIPA foam compositions achieve have significantly higher toughness compared to previous low density SMP foams. The increased material strength (peak stress) is attributed to the aromatic structure of the ATIPA monomer. The BDL traditionally avoids aromatic polyurethane monomers, such as Toluene Diisocyanate, due to historical concerns with the biocompatibility of aromatic diamines in potential

degradation products.[128, 129] However, aromatic compounds traditionally display higher strength when compared to their aliphatic counterparts.[130] Although this polymer system was designed to be biodurable with minimal sites for oxidative or hydrolytic degradation, the biocompatibility of potential aromatic degradation products is worthwhile for future investigation. These investigations should be conducted in conjunction with in-vivo vascular implants and in-vitro mass loss studies.

Increases in ductility (strain at break) are attributed to a decrease in crosslink density compared to the non-visible control SMP foam. The foams traditionally used by BDL only use polyols with functionalities of 3 (TEA) or 4 (HPED). These crosslinking sites are bridged by short diisocyanate segments (TMHDI or HDI) to create a highly crosslinked material. This crosslink density affords excellent shape memory, but at the relative expense of overall toughness. This is not a problem in an unloaded foam, but it becomes problematic with Tungsten-loaded composites that introduce stress concentrations in the strut cross section. Alternatively, the proposed ATIPA compositions employ the aliphatic diols MPD and BEP to increase the molecular weight between crosslinks for increased ductility. The rigidity of ATIPA enables this chain extension while keeping the dry transition temperature of the overall material within a functional biomedical range (40–60°C).

The combined increases in ductility and strength contribute to significant increases in tensile toughness. Compared to non-visible foams, 25AT and 30AT compositions are over 11 and 14 times tougher, respectively. Compared to 6 vol% Tungsten nanoparticle foams, 25AT and 30AT foams are 46 and 57 times tougher,

respectively. This dramatic increase in toughness significantly lowers the risk of undesired embolic particles detaching from the foam and flowing downstream from the target therapeutic region. However, this toughness can also impact manufacturing. Increased difficulty for foam machining and cutting could motivate new device prototyping techniques. Additionally, these closed cell foams will need to be reticulated. The increased toughness of cell membranes may require significantly different reticulation parameters for both mechanical and plasma reticulation. Alternatively, foaming parameters could be optimized to introduce cell openers to create open porosity in the native foam.

4.3.3 X-ray imaging

Figure 4.11 summarizes the x-ray visibility of low density foams with varying ATIPA content. The foams with 10–30 eq% ATIPA demonstrate comparable x-ray visibility because the blowing ATIPA reaction resulted in lower material density at higher contrast agent loading. These opposing trends resulted in comparable iodine content within the same expanded sample path length.

The 8 mm cylindrical peripheral embolization prototypes demonstrated visibility in their expanded state, even when imaged through the skull analog. When radially crimped, these materials demonstrated visibility comparable to commercially available embolic platinum coils. Radial compression also compensates for differences in bulk material density, revealing differences in x-ray visualization for samples with varying ATIPA content. For example, the radially compressed 30AT sample is noticeably more visible than the 20AT sample when imaged through the ½” aluminum skull analog.

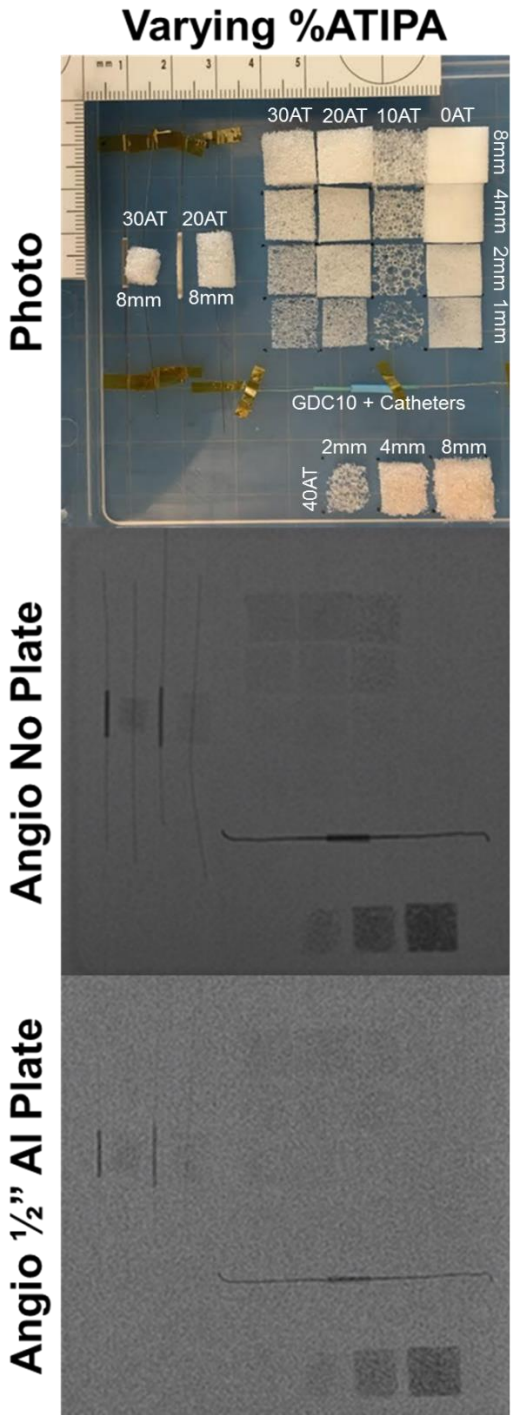

Figure 4.11: Imaging frame including foam samples with varying ATIPA content at varying thickness; platinum embolic coils (GDC10) and catheter segments for radiodensity reference; and 8 mm diameter foam cylinder device prototypes in expanded and compressed states. Samples were imaged with a camera, unimpeded angiography, and angiography through a ½" aluminum human skull analog.

Figure 4.12 details foams with a fixed 20 eq% ATIPA composition at varying density. Increasing material density results in increased material visualization, with the densest foam exhibiting visibility at 1 mm thickness, even through the skull analog. The 2 mm neurovascular prototypes displayed limited visibility, even when axially crimped.

To address the limited material visibility at the neurovascular device scale, future prototypes should incorporate foams with higher ATIPA percentages. Alternatively, a combinatory approach of chemical opacification and tungsten nanoparticulate loading could achieve SMP foam visualization at neurovascular device scales. Based on the tensile testing data in the previous section, an ATIPA composite with tungsten nanoparticulate stress concentrators is hypothesized to maintain a higher fracture toughness than the traditional non-visible SMP foam. This would maintain the existing acceptable risk level for undesired embolic particulates, while affording excellent x-ray visualization during device implantation.

Visualization of the expanded material would be ideal for clinical adoption without significant physician training. However, visible crimped devices would also be acceptable for device performance. Instead of direct visualization foam expansion, the gradual decrease in material visualization would provide a secondary indication of foam expansion.

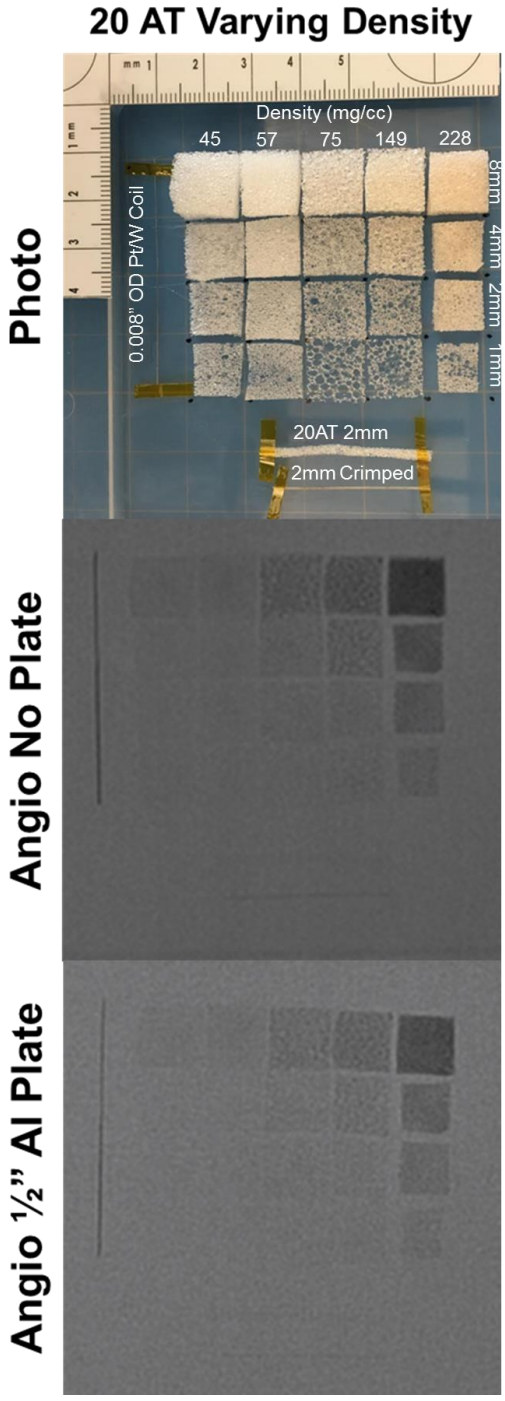

Figure 4.12: **Imaging frame including 20 eq% ATIPA foam samples with varying densities and thickness; a platinum embolic coil (GDC10) for radiodensity reference; and 2 mm diameter foam cylinder device prototypes (20AT, 57 mg/cc) in expanded and crimped states. Samples were imaged with a camera, unimpeded angiography, and angiography through a ½" aluminum human skull analog.**

4.3.4 DSC

Differential scanning calorimetry was used to determine compositional effects on T_g and the breadth of thermal transitions. This data is important input for developing materials that are tuned to specific device design criteria, including foam expansion rate. Figure 4.13 illustrates consistent thermal properties for foams with varying density due to physical blowing agent, further supporting the ability to control foam morphology independent of transition temperature. Lowering the foam density enables more material to crimp to a catheter deliverable cross section. This allows for larger volumetric expansion in-vivo and more effective filling to facilitate occlusion.

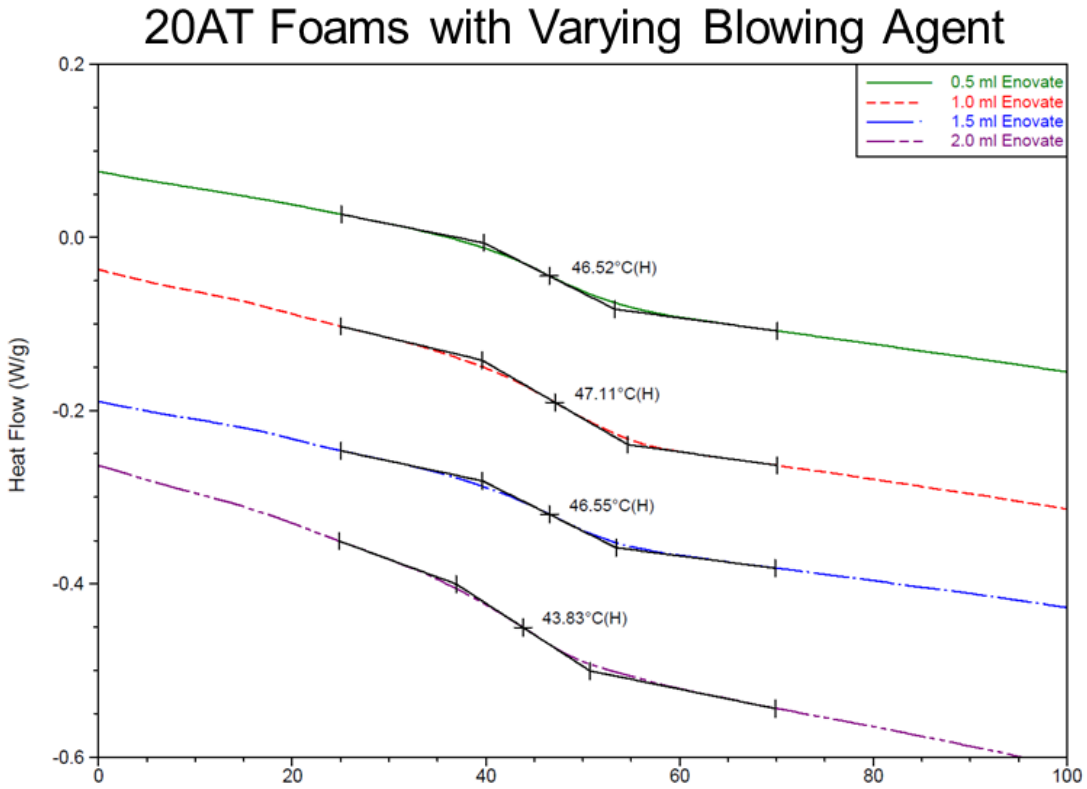

Figure 4.13: Dry DSC thermograms showing minimal change in dry T_g for foams with varying density due to changes in physical blowing agent (Enovate) volume.

Figure 4.14 shows incremental control over both dry and moisture plasticized T_g based on HT composition. Increasing the molar ratio of the trifunctional HT monomer increases the crosslink density to make the polymer structure more rigid and raise the glass transition. For each composition, the wet and dry transitions are positioned on either side of body temperature (37°C), enabling passive material expansion once implanted in the body. Based on these thermograms, the 20HT, 30HT, and 40HT compositions were chosen for further analysis toward device development. The 10HT composition was determined to have a dry transition too low for sufficient working times at the neurovascular device prototype scale.

Both the transition temperature value and the breadth of transition increase with increasing HT content. As seen in the lower left corner of the figure, fully plasticized 10HT compositions still contained sufficient water content to register water freezing in the thermogram.

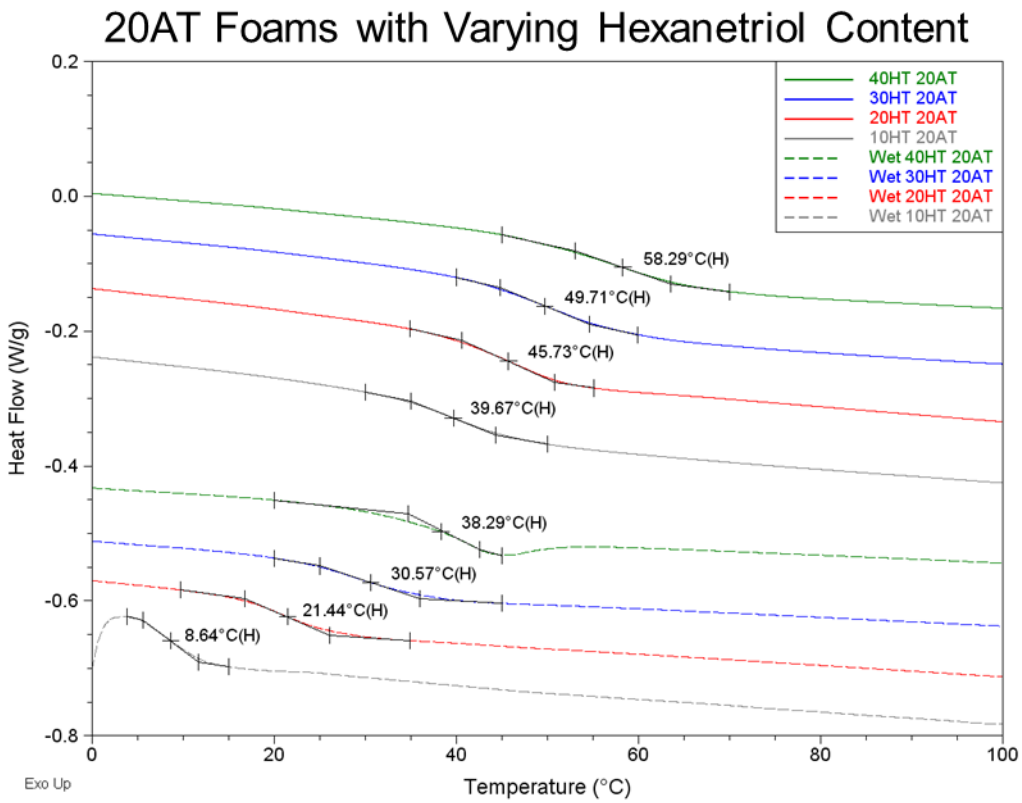

Figure 4.14: DSC thermograms for dry and moisture plasticized 20 eq% ATIPA foams with varying HT content.

Although less significant, changing the isocyanate content also enabled control over T_g. Instead of altering crosslink density, increasing the molar ratio of TMHDI increased the rigidity of polymer chains between crosslinks. In addition to increasing T_g, higher TMHDI content is also anticipated to increase the bulk hydrophobicity of the material to reduce the moisture plasticization rate of the material and overall foam expansion time.

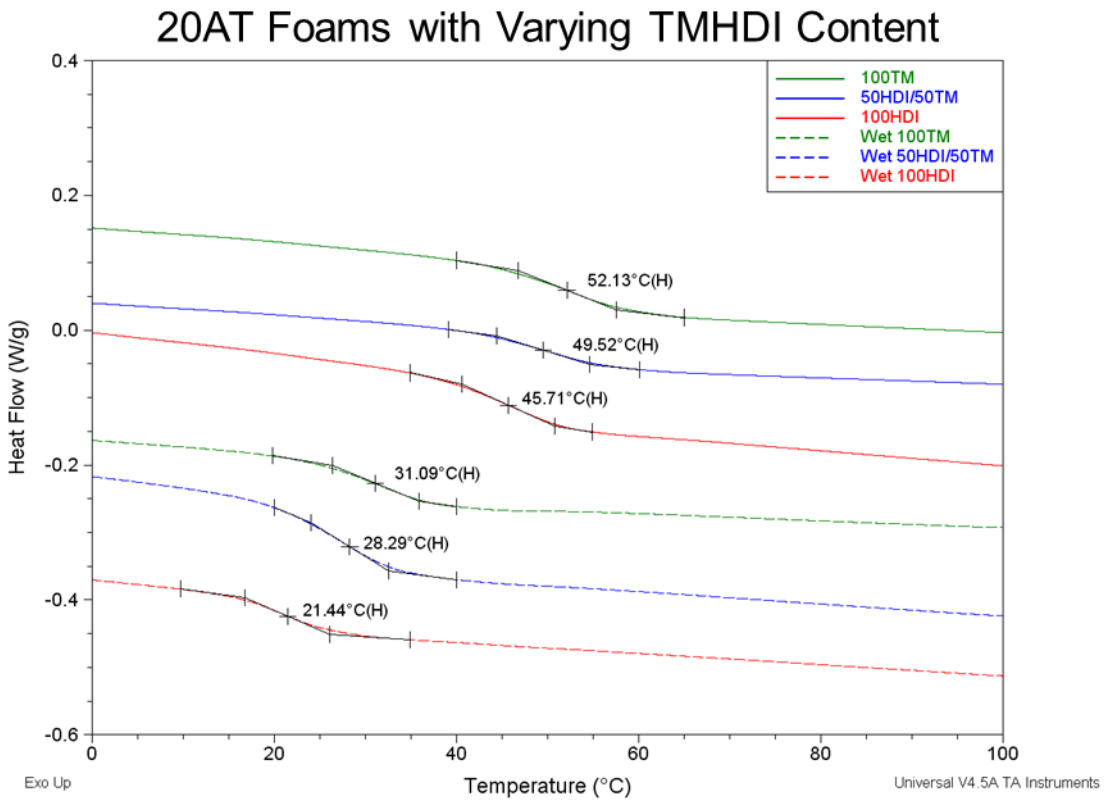

Figure 4.15: Thermograms for dry and moisture plasticized 20 eq% ATIPA foams with varying isocyanate content.

Thermograms depicting increasing ATIPA composition are illustrated in Figure 4.15. In addition to increasing T_g, there is also significant increases in transition breadth. The transition also becomes much less defined. These changes in the thermogram profile motivated further DMA analysis for these select compositions, except for the 40AT composition that was too brittle for sufficient analysis or prototyping.

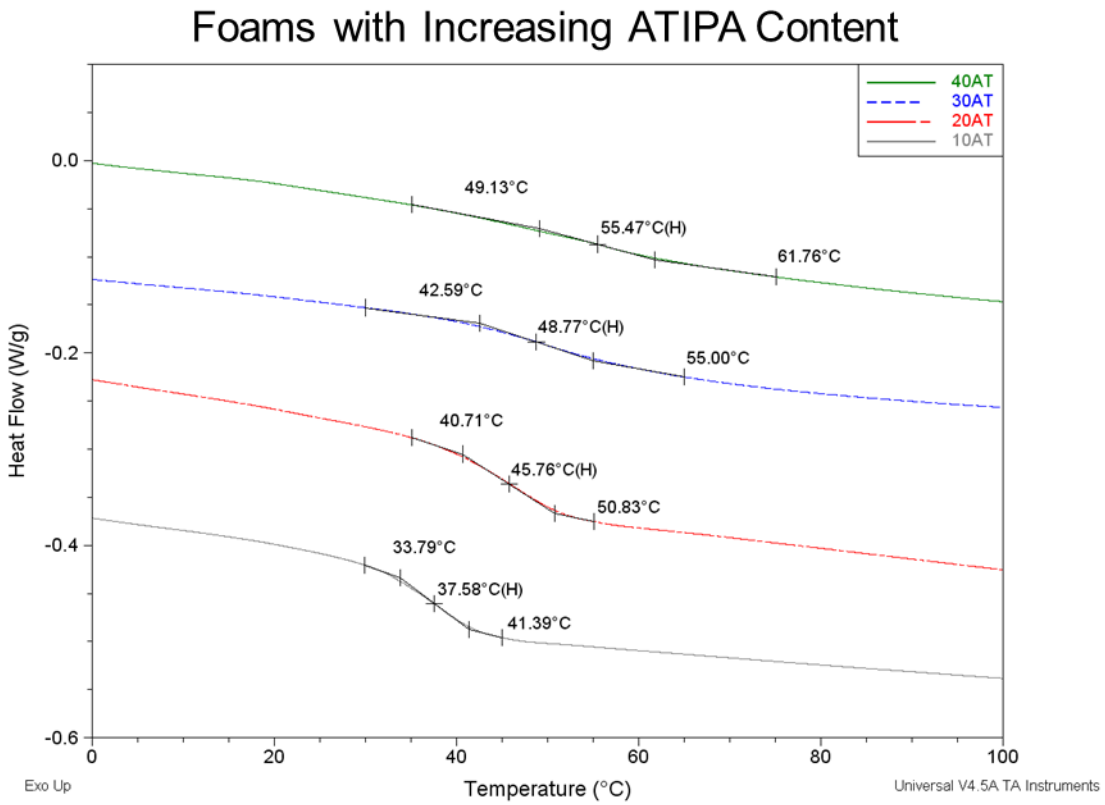

Figure 4.16: Thermograms for dry foams with varying eq% of ATIPA.

4.3.5 DMA

When comparing Figure 4.16 and 4.13, peak Tan δ values are approximately 20°C higher than DSC dry T_g values. However, the incremental differences in each composition are comparable. This DMA data further supports increasing T_g with increasing HT content.

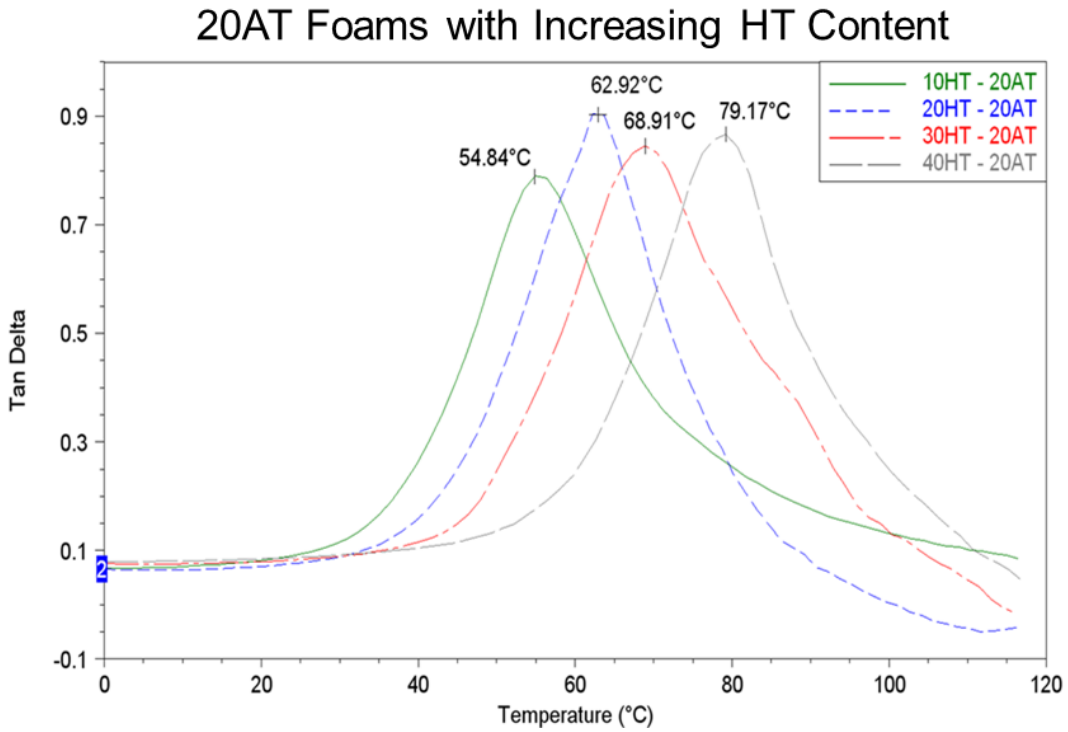

Figure 4.17: Tangent delta plots from compression DMA of dry 20 eq% ATIPA foams with varying HT composition.

Tangent δ plots in Figure 4.17 illustrate T_g values 20–30°C higher than dry DSC values in Figure 4.15. The DMA curves also shows a similar trend with increasing T_g and transition breadth with increasing ATIPA content. Most interesting is the shape of the 30AT composition curve. Although a signal peak is evident, the Tan δ signal does not return to baseline after the thermal transition. This is indicative of a dampening material with a low rubbery modulus, which are both indicative of a poor shape memory polymer. It is unclear if this material response is due to the higher ATIPA composition, or if the introduction of anhydrous THF altered the reaction kinetics and final structure of the polymer system. Based on these results, foam compositions for device prototyping were chosen based on the maximum inherent solubility of ATIPA in the other polyol

constituents without solvent. This maximum is in the 20–25 ATIPA eq% range, depending on the composition.

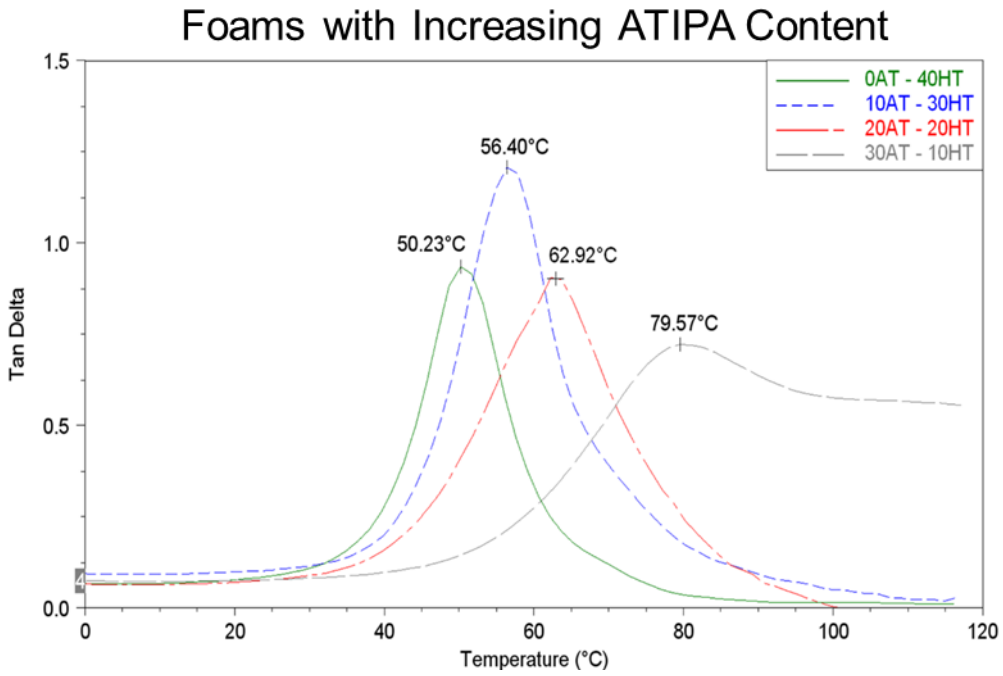

Figure 4.18: Tangent delta plots for compression DMA of dry foams with varying ATIPA composition.

4.3.6 Unconstrained expansion

Foams with varying HT content displayed volumetric recovery behavior in body temperature water that is congruent with T_g trends. As seen in Figure 4.18, compositions with higher HT content and higher T_g took longer to expand. The 30 and 40 eq% HT compositions also showed higher average volumetric recovery (99%) when compared to 20 eq% HT foams with a lower crosslink density (91%).

This data shows promise relative to a neurovascular embolization device design. With an average crimped diameter of 0.0196” ± 0.001”, these prototypes are close to

fitting within a 0.021” microcatheter lumen with a target minimum tolerance of 0.002”. Modifications to the blowing agent and surfactant composition can decrease the bulk foam density for smaller crimped dimensions, in addition to using a smaller diameter device backbone filament.

These expansion profiles show an estimated minimum working time of 10 minutes for the 30HT composition and 15 minutes for the 40HT composition. These default expansion times are already in the clinically acceptable range without employing surface coatings to modulate moisture plasticization.

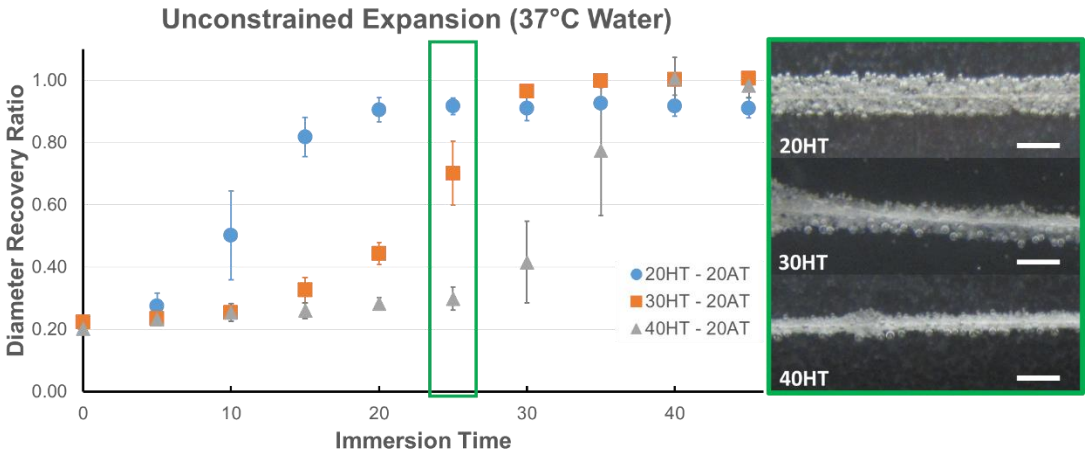

Figure 4.19: Left - Unconstrained expansion profiles of 2mm diameter foams compressed over a 0.006” wire and submerged in 37°C water. Right – Snapshots of foams after 25 minutes of immersion.

4.3.7 FTIR-ATR

Infrared spectra in Figure 4.20 do not exhibit significant changes with increasing HT content. However, these spectra do show peaks characteristic of polyurethane foams.[131-133] The broad peak centered at 3310 cm^{-1} highlights N-H vibrations. Peaks

at 2852 cm^{-1} and 2923 cm^{-1} are from symmetric and asymmetric C-H stretching from the MPD methyl group. It is worthy to note the lack of an unreacted NCO peak at 2260 cm^{-1}. At 1685 cm^{-1}, the C=O urethane peak is significantly right shifted due to hydrogen bonding. This is congruent with hydrogen bonded urethane peaks in other polyurethane SMP foams with relatively low molecular weights between crosslinks when compared to segmented polyurethanes. Strong Amide II and Amide III peaks can be seen at 1515 cm^{-1} and 1230 cm^{-1}, respectively.

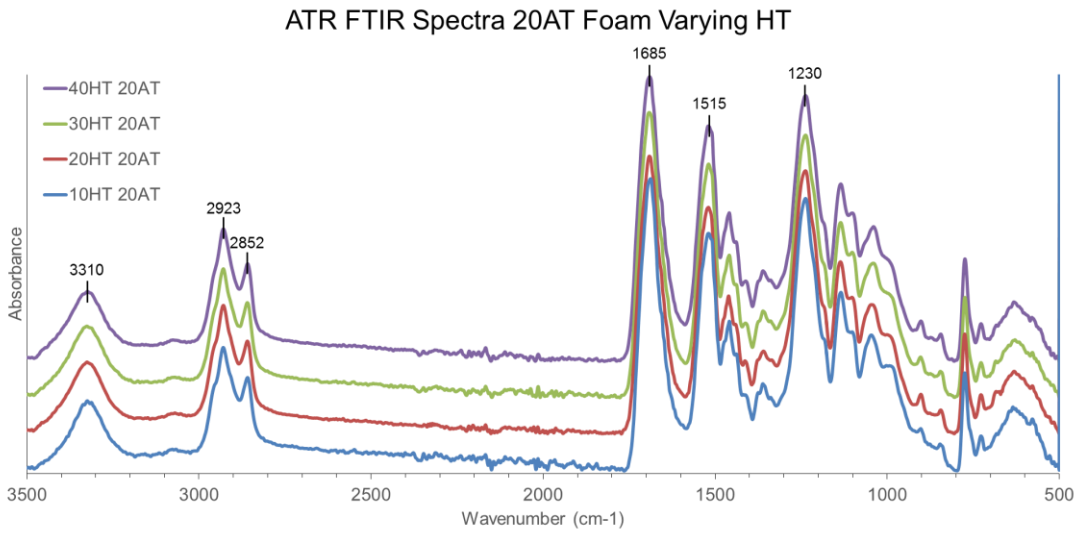

Figure 4.20: ATR FTIR spectra for 20AT foams with increasing HT content.

20 eq% ATIPA foam spectra with increasing TMHDI content are shown in Figure 4.21. A non-visible 100TM H60 foam is also included for comparison. Increased methylation with increasing TMHDI content is evident due to peak broadening between 2800-3000 cm^{-1}. Compared to the non-visible foam, ATIPA foams do not have a

prominent urea shoulder at 1650 cm^{-1} due to the lack of H_2O chemical blowing used in traditional polyurethane foaming.

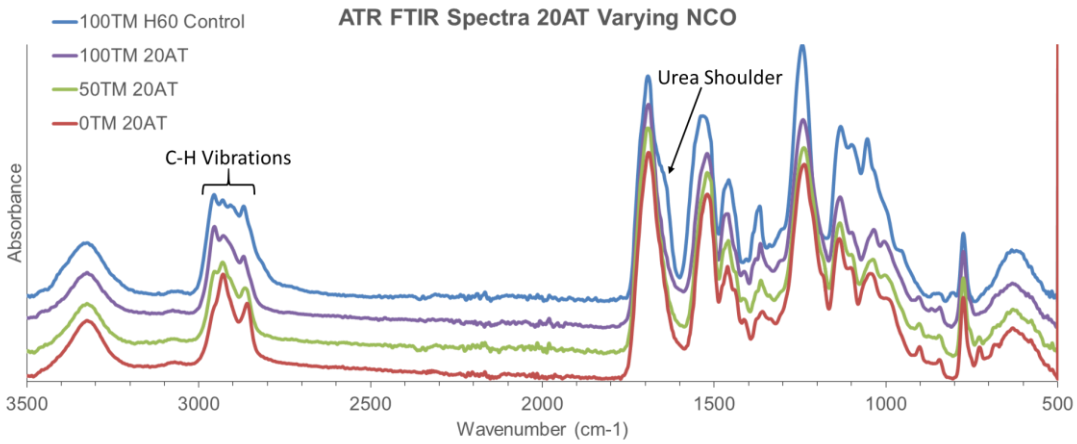

Figure 4.21: ATR FTIR spectra for 20AT foams with increasing TMHDI content. Non-visible 100TM H60 control foam spectra included for comparison.

Compositions with increasing ATIPA content, Figure 4.22, show a broadening urea shoulder due to higher NH_2 reactive groups during synthesis. This differs from the urea content present in traditional polyurethane urea foams that use water as a chemical blowing agent.

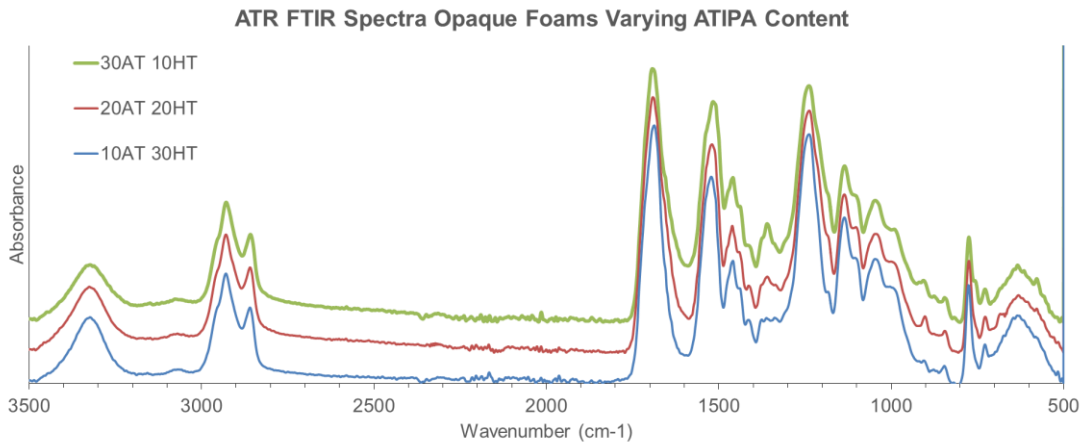

Figure 4.22: ATR FTIR spectra for foams with increasing ATIPA content at fixed theoretical crosslink density.

4.4 Conclusions

In this work, chemically modified shape memory polymer foams with inherent x-ray visualization were successfully fabricated through the incorporation of triiodobenzene containing monomers. Altering the molar ratios of the other constituent monomers also demonstrated functional changes in these polymer scaffolds that show promise for incorporation into embolic medical devices. Future work should pursue characterizing the in-vitro cytocompatibility and in-vivo biocompatibility of these polymers.

CHAPTER V

CONCLUSIONS

5.1 Surface modifications

The engineered surfaces in this dissertation successfully enabled new shape memory medical device performance. Reactive cold plasmas were proven to enable independent control over surface and bulk material properties. Decoupling these performance criteria can create avenues for biomedical devices that interact more favorably with their implanted environment without compromising mechanical integrity or shape memory characteristics inherent to the bulk material. The use of plasma deposited hydrocarbons for controlled expansion and plasma reticulation for selective removal of polymer scaffold membranes are just two examples of a wide array of biomedical applications that can be enabled by cold reactive plasmas.

5.2 Bulk material modifications

Bulk chemical modification of SMPs to incorporate triiodobenzene monomers successfully achieved x-ray visualization with unprecedented performance. A bulk approach was necessary to achieve sufficient loading of high atomic weight constituents for sufficient visualization. The material system was designed with functional material performance and long-term degradation in mind. However, biologic surface interactions with this material remain largely uncharacterized. Cytocompatibility and pathology of implanted ATIPA foam are critical data-sets that are still necessary for assessing the biomedical utility of these materials. Should issues arise during this assessment, new plasma surface modifications could be leveraged to solve potential surface problems.

5.3 Challenges and future directions

Although plasma-deposited hydrocarbons have demonstrated utility, their impact on biocompatibility still remains unanswered. Alternative solvent-based neat polymer coatings were developed in parallel to the plasma-based approach. These neat coatings have the same basic composition as the substrate SMP foam and serve as diffusion barriers with the added benefit of adhering the SMP foam to other device substrates. This neat coating is less sensitive to process and aging conditions and is being incorporated into the development of a commercial embolization device. For the time being, plasma hydrocarbon films are not being actively incorporated into a translational medical device design.

In contrast, plasma reticulation affords unique properties that cannot be achieved with alternative processes. Future work should expand on the control of surface topography relative to cell-material interactions, including the inclusion of masking techniques for gradient control of cellular behavior within tissue engineering scaffolds.

The long-term biocompatibility, hydrolytic stability, and oxidative stability of x-ray visible ATIPA foams remain unanswered within this work. Characterizing these material properties with in-vitro degradation experiments and in-vivo implantation will be important for facilitating the translation of these materials to the clinic.

Finally, the closed cell nature of ATIPA foams and mechanical integrity of intact membranes make plasma reticulation an attractive option for producing open celled scaffolds. However, similar characterization of plasma-reticulated ATIPA surfaces should be conducted to identify cytocompatibility, surface composition, and surface

topography. Alternatively, cell opening agents could be incorporated to the material synthesis to create scaffolds that inherently cure in an open celled configuration.

REFERENCES

[1] A. J. Boyle, T. L. Landsman, M. A. Wierzbicki, L. D. Nash, W. Hwang, M. W. Miller, *et al.*, "In vitro and in vivo evaluation of a shape memory polymer foam-over-wire embolization device delivered in saccular aneurysm models," *Journal of Biomedical Materials Research Part B: Applied Biomaterials*, 2015.

[2] S. M. Hasan, G. Harmon, F. Zhou, J. E. Raymond, T. P. Gustafson, T. S. Wilson, *et al.*, "Tungsten-loaded SMP foam nanocomposites with inherent radiopacity and tunable thermo-mechanical properties," *Polymers for Advanced Technologies,* vol. 27, pp. 195-203, 2016.

[3] P. Singhal, J. N. Rodriguez, W. Small, S. Eagleston, J. Van de Water, D. J. Maitland, *et al.*, "Ultra low density and highly crosslinked biocompatible shape memory polyurethane foams," *Journal of Polymer Science Part B: Polymer Physics,* vol. 50, pp. 724-737, 2012.

[4] J. N. Rodriguez, F. J. Clubb, T. S. Wilson, M. W. Miller, T. W. Fossum, J. Hartman, *et al.*, "In vivo response to an implanted shape memory polyurethane foam in a porcine aneurysm model," *J Biomed Mater Res A,* May 7 2013.

[5] A. Lendlein and S. Kelch, "Shape-memory polymers," *Angewandte Chemie International Edition,* vol. 41, pp. 2034-2057, 2002.

[6] K. Hearon, M. A. Wierzbicki, L. D. Nash, T. L. Landsman, C. Laramy, A. T. Lonnecker, *et al.*, "A Processable Shape Memory Polymer System for Biomedical Applications," *Advanced Healthcare Materials,* 2015.

[7] D. J. Maitland, M. F. Metzger, D. Schumann, A. Lee, and T. S. Wilson, "Photothermal properties of shape memory polymer micro-actuators for treating stroke," *Lasers Surg Med,* vol. 30, pp. 1-11, 2002.

[8] I. V. W. Small, P. R. Buckley, T. S. Wilson, J. M. Loge, K. D. Maitland, and D. J. Maitland, "Fabrication and characterization of cylindrical light diffusers comprised of shape memory polymer," *Journal of Biomedical Optics,* vol. 13, pp. 024018-024018-7, 2008.

[9] M. D. Hager, S. Bode, C. Weber, and U. S. Schubert, "Shape memory polymers: Past, present and future developments," *Progress in Polymer Science,* vol. 49–50, pp. 3-33, 2015.

[10] L. Sun, W. M. Huang, Z. Ding, Y. Zhao, C. C. Wang, H. Purnawali, *et al.*, "Stimulus-responsive shape memory materials: A review," *Materials & Design,* vol. 33, pp. 577-640, 2012.

[11] T. S. Wilson, J. P. Bearinger, J. L. Herberg, J. E. Marion, W. J. Wright, C. L. Evans, *et al.*, "Shape memory polymers based on uniform aliphatic urethane networks," *Journal of Applied Polymer Science,* vol. 106, pp. 540-551, 2007.

[12] Q. Zhao, H. J. Qi, and T. Xie, "Recent progress in shape memory polymer: New behavior, enabling materials, and mechanistic understanding," *Progress in Polymer Science,* vol. 49–50, pp. 79-120, 2015.

[13] Q. Meng and J. Hu, "A review of shape memory polymer composites and blends," *Composites Part A: Applied Science and Manufacturing,* vol. 40, pp. 1661-1672, 2009.

[14] I. V. W. Small, P. Singhal, T. S. Wilson, and D. J. Maitland, "Biomedical applications of thermally activated shape memory polymers," *Journal of Materials Chemistry*, vol. 20, pp. 3356-3366, 2010.

[15] K. Hearon, L. D. Nash, B. L. Volk, T. Ware, J. P. Lewicki, W. E. Voit, *et al.*, "Electron Beam Crosslinked Polyurethane Shape Memory Polymers with Tunable Mechanical Properties," *Macromolecular Chemistry and Physics*, vol. 214, pp. 1258-1272, 2013.

[16] J. Horn, W. Hwang, S. L. Jessen, B. K. Keller, M. W. Miller, E. Tuzun, *et al.*, "Comparison of shape memory polymer foam versus bare metal coil treatments in an in vivo porcine sidewall aneurysm model," *Journal of Biomedical Materials Research Part B: Applied Biomaterials*, 2016.

[17] T. L. Landsman, R. L. Bush, A. Glowczwski, J. Horn, S. L. Jessen, E. Ungchusri, *et al.*, "Design and verification of a shape memory polymer peripheral occlusion device," *Journal of the Mechanical Behavior of Biomedical Materials*, vol. 63, pp. 195-206, 2016.

[18] J. M. Szafron, A. D. Muschenborn, and D. J. Maitland, "Design and Characterization of an Endovascular Mechanical Thrombectomy Device1," *Journal of Medical Devices*, vol. 8, 2014.

[19] M. A. Wierzbicki, J. Bryant, M. W. Miller, B. Keller, and D. J. Maitland, "Mechanical and in vitro evaluation of an experimental canine patent ductus arteriosus occlusion device," *Journal of the Mechanical Behavior of Biomedical Materials*, vol. 59, pp. 156-167, 2016.

[20] L. D. Nash, M. A. Wierzbicki, and D. J. Maitland, "Design and Characterization of a Resistively Heated Shape Memory Polymer Micro-Release Device1," *Journal of Medical Devices,* vol. 8, pp. 020911-020911, 2014.

[21] H. P. Hentze and M. Antonietti, "Porous polymers and resins for biotechnological and biomedical applications," *J Biotechnol,* vol. 90, pp. 27-53, 2002.

[22] D. Zhang, O. J. George, K. M. Petersen, A. C. Jimenez-Vergara, M. S. Hahn, and M. A. Grunlan, "A bioactive “self-fitting” shape memory polymer scaffold with potential to treat cranio-maxillo facial bone defects," *Acta Biomaterialia,* vol. 10, pp. 4597-4605, 2014.

[23] A. M. El-Kady, R. A. Rizk, B. M. Abd El-Hady, M. W. Shafaa, and M. M. Ahmed, "Characterization, and antibacterial properties of novel silver releasing nanocomposite scaffolds fabricated by the gas foaming/salt-leaching technique," *Journal of Genetic Engineering and Biotechnology*, vol. 10, pp. 229-238, 2012.

[24] M. Okamoto and B. John, "Synthetic biopolymer nanocomposites for tissue engineering scaffolds," *Progress in Polymer Science,* vol. 38, pp. 1487-1503, 2013.

[25] H. Janik and M. Marzec, "A review: Fabrication of porous polyurethane scaffolds," *Materials Science and Engineering: C,* vol. 48, pp. 586-591, 2015.

[26] P. Hariraksapitak, O. Suwantong, P. Pavasant, and P. Supaphol, "Effectual drug-releasing porous scaffolds from 1,6-diisocyanatohexane-extended poly(1,4-

butylene succinate) for bone tissue regeneration," *Polymer,* vol. 49, pp. 2678-2685, 2008.

[27] H. J. Park, O. J. Lee, M. C. Lee, B. M. Moon, H. W. Ju, J. m. Lee, *et al.*, "Fabrication of 3D porous silk scaffolds by particulate (salt/sucrose) leaching for bone tissue reconstruction," *International Journal of Biological Macromolecules,* vol. 78, pp. 215-223, 2015.

[28] J. J. Yoon, J. H. Kim, and T. G. Park, "Dexamethasone-releasing biodegradable polymer scaffolds fabricated by a gas-foaming/salt-leaching method," *Biomaterials,* vol. 24, pp. 2323-2329, 2003.

[29] L. De Nardo, R. Alberti, A. Cigada, L. Yahia, M. C. Tanzi, and S. Fare, "Shape memory polymer foams for cerebral aneurysm reparation: effects of plasma sterilization on physical properties and cytocompatibility," *Acta Biomater,* vol. 5, pp. 1508-18, 2009.

[30] A. G. Mikos, G. Sarakinos, S. M. Leite, J. P. Vacanti, and R. Langer, "Laminated three-dimensional biodegradable foams for use in tissue engineering," *Biomaterials,* vol. 14, pp. 323-30, 1993.

[31] K. J. Lissant, "The geometry of high-internal-phase-ratio emulsions," *Journal of Colloid and Interface Science,* vol. 22, pp. 462-468, 1966.

[32] K. J. Lissant and K. G. Mayhan, "A study of medium and high internal phase ratio water/polymer emulsions," *Journal of Colloid and Interface Science,* vol. 42, pp. 201-208, 1973.

[33] S. U. Pickering, "CXCVI.-Emulsions," *Journal of the Chemical Society, Transactions,* vol. 91, pp. 2001-2021, 1907.

[34] S. Arditty, C. P. Whitby, B. P. Binks, V. Schmitt, and F. Leal-Calderon, "Some general features of limited coalescence in solid-stabilized emulsions," *Eur Phys J E Soft Matter,* vol. 11, pp. 273-81, Jul 2003.

[35] M. Destribats, B. Faure, M. Birot, O. Babot, V. Schmitt, and R. Backov, "Tailored Silica Macrocellular Foams: Combining Limited Coalescence-Based Pickering Emulsion and Sol–Gel Process," *Advanced Functional Materials,* vol. 22, pp. 2642-2654, 2012.

[36] F. Leal-Calderon and V. Schmitt, "Solid-stabilized emulsions," *Current Opinion in Colloid & Interface Science,* vol. 13, pp. 217-227, 2008.

[37] M. S. Silverstein, "Emulsion-templated porous polymers: A retrospective perspective," *Polymer,* vol. 55, pp. 304-320, 2014.

[38] M. S. Silverstein, "PolyHIPEs: Recent advances in emulsion-templated porous polymers," *Progress in Polymer Science,* vol. 39, pp. 199-234, 2014.

[39] I. Gurevitch and M. S. Silverstein, "Shape memory polymer foams from emulsion templating," *Soft Matter,* vol. 8, pp. 10378-10387, 2012.

[40] W. Drenckhan and A. Saint-Jalmes, "The science of foaming," *Advances in Colloid and Interface Science,* vol. 222, pp. 228-259, 2015.

[41] C. Ji, N. Annabi, A. Khademhosseini, and F. Dehghani, "Fabrication of porous chitosan scaffolds for soft tissue engineering using dense gas CO2," *Acta Biomaterialia,* vol. 7, pp. 1653-1664, 2011.

[42] J. K. Jensen, L. O. Jensen, C. J. Terkelsen, J. F. Lassen, H. H. Tilsted, K. N. Hansen, *et al.*, "Incidence of definite stent thrombosis or in-stent restenosis after drug-eluting stent implantation for treatment of coronary in-stent restenosis: From Western Denmark heart registry," *Catheterization and Cardiovascular Interventions,* vol. 81, pp. 260-265, 2013.

[43] I. Pasquali, R. Bettini, and F. Giordano, "Solid-state chemistry and particle engineering with supercritical fluids in pharmaceutics," *European Journal of Pharmaceutical Sciences,* vol. 27, pp. 299-310, 2006.

[44] A. R. C. Duarte, J. F. Mano, and R. L. Reis, "Perspectives on: Supercritical Fluid Technology for 3D Tissue Engineering Scaffold Applications," *Journal of Bioactive and Compatible Polymers,* vol. 24, pp. 385-400, 2009.

[45] A. R. C. Duarte, J. F. Mano, and R. L. Reis, "Supercritical fluids in biomedical and tissue engineering applications: a review," *International Materials Reviews,* vol. 54, pp. 214-222, 2009.

[46] D. J. Maitland, W. t. Small, J. M. Ortega, P. R. Buckley, J. Rodriguez, J. Hartman, *et al.*, "Prototype laser-activated shape memory polymer foam device for embolic treatment of aneurysms," *J Biomed Opt,* vol. 12, p. 030504, 2007.

[47] S. M. Hasan, G. Harmon, F. Zhou, J. E. Raymond, T. P. Gustafson, T. S. Wilson, *et al.*, "Tungsten-loaded SMP foam nanocomposites with inherent radiopacity and tunable thermo-mechanical properties," *Polymer Advanced Technology,* 2015.

[48] S. M. Hasan, J. E. Raymond, T. S. Wilson, B. K. Keller, and D. J. Maitland, "Effects of Isophorone Diisocyanate on the Thermal and Mechanical Properties of Shape-Memory Polyurethane Foams," *Macromolecular Chemistry and Physics*, vol. 215, pp. 2420-2429, 2014.

[49] Y. Murayama, Y. L. Nien, G. Duckwiler, Y. P. Gobin, R. Jahan, J. Frazee, *et al.*, "Guglielmi detachable coil embolization of cerebral aneurysms: 11 years' experience," *Journal of neurosurgery*, vol. 98, pp. 959-966, 2003.

[50] V. L. Roger, A. S. Go, D. M. Lloyd-Jones, R. J. Adams, J. D. Berry, T. M. Brown, *et al.*, "Heart disease and stroke statistics—2011 update a report from the American Heart Association," *Circulation*, vol. 123, pp. e18-e209, 2011.

[51] M. H. Babiker, L. F. Gonzalez, F. Albuquerque, D. Collins, A. Elvikis, and D. H. Frakes, "Quantitative effects of coil packing density on cerebral aneurysm fluid dynamics: an in vitro steady flow study," *Annals of biomedical engineering*, vol. 38, pp. 2293-2301, 2010.

[52] R. C. Gaba, S. A. Ansari, S. S. Roy, F. A. Marden, M. A. Viana, and T. W. Malisch, "Embolization of Intracranial Aneurysms With Hydrogel-Coated Coils Versus Inert Platinum Coils Effects on Packing Density, Coil Length and Quantity, Procedure Performance, Cost, Length of Hospital Stay, and Durability of Therapy," *Stroke*, vol. 37, pp. 1443-1450, 2006.

[53] S. D. Simon, A. S. Reig, R. F. James, P. Reddy, and R. A. Mericle, "Relative cost comparison of embolic materials used for treatment of wide-necked intracranial aneurysms," *Journal of neurointerventional surgery*, vol. 2, pp. 163-167, 2010.

[54] B. R. Bendok, R. J. Parkinson, Z. A. Hage, J. G. Adel, and M. J. Gounis, "The Effect of Vascular Reconstruction Device-Assisted Coiling on Packing Density, Effective Neck Coverage, and Angiographic Outcome: An in Vitro Study," *Neurosurgery,* vol. 61, pp. 835-841, 2007.

[55] N. Chalouhi, P. Jabbour, L. F. Gonzalez, A. S. Dumont, R. Rosenwasser, R. M. Starke, *et al.*, "Safety and efficacy of endovascular treatment of basilar tip aneurysms by coiling with and without stent assistance: a review of 235 cases," *Neurosurgery,* vol. 71, pp. 785-794, 2012.

[56] N. Chalouhi, P. Jabbour, S. Singhal, R. Drueding, R. M. Starke, R. T. Dalyai, *et al.*, "Stent-assisted coiling of intracranial aneurysms predictors of complications, recanalization, and outcome in 508 cases," *Stroke,* vol. 44, pp. 1348-1353, 2013.

[57] S.-N. H. Khan, C. Nichols, J. J. DePowell, T. A. Abruzzo, and A. J. Ringer, "Comparison of coil types in aneurysm recurrence," *Clinical neurology and neurosurgery,* vol. 114, pp. 12-16, 2012.

[58] A. O'Hare, N. Fanning, J. Ti, R. Dunne, P. Brennan, and J. Thornton, "HydroCoils, occlusion rates, and outcomes: a large single-center study," *American Journal of Neuroradiology,* vol. 31, pp. 1917-1922, 2010.

[59] R. B. McLafferty, J. M. Lohr, J. A. Caprini, M. A. Passman, F. T. Padberg, T. W. Rooke, *et al.*, "Results of the National Pilot Screening Program for Venous Disease by the American Venous Forum," *Journal of Vascular Surgery,* vol. 45, pp. 142-148, 2007.

[60] A. N. Nicolaides, "Investigation of Chronic Venous Insufficiency: A Consensus Statement," *Circulation,* vol. 102, pp. e126-e163, 2000.

[61] M. R. Perrin, N. Labropoulos, and L. R. Leon Jr, "Presentation of the patient with recurrent varices after surgery (REVAS)," *Journal of Vascular Surgery,* vol. 43, pp. 327-334, 2006.

[62] M. A. Sharif, C. V. Soong, L. L. Lau, R. Corvan, B. Lee, and R. J. Hannon, "Endovenous laser treatment for long saphenous vein incompetence," *British Journal of Surgery,* vol. 93, pp. 831-835, 2006.

[63] T. M. Proebstle, H. A. Lehr, A. Kargl, C. Espinola-Klein, W. Rother, S. Bethge, *et al.*, "Endovenous treatment of the greater saphenous vein with a 940-nm diode laser: Thrombotic occlusion after endoluminal thermal damage by laser-generated steam bubbles," *Journal of Vascular Surgery,* vol. 35, pp. 729-736, 2002.

[64] R. R. Van Den Bos, M. Neumann, K.-P. De Roos, and T. Nijsten, "Endovenous Laser Ablation–Induced Complications: Review of the Literature and New Cases," *Dermatologic Surgery,* vol. 35, pp. 1206-1214, 2009.

[65] A. S. Hoffman, "Ionizing radiation and gas plasma (or glow) discharge treatments for preparation of novel polymeric biomaterials," in *Polymers in medicine,* ed: Springer, pp. 141-157, 1984.

[66] P. K. Chu, J. Y. Chen, L. P. Wang, and N. Huang, "Plasma-surface modification of biomaterials," *Materials Science and Engineering: R: Reports,* vol. 36, pp. 143-206, 2002.

[67] T. Desmet, R. Morent, N. De Geyter, C. Leys, E. Schacht, and P. Dubruel, "Nonthermal plasma technology as a versatile strategy for polymeric biomaterials surface modification: a review," *Biomacromolecules*, vol. 10, pp. 2351-78, 2009.

[68] T. Jacobs, R. Morent, N. De Geyter, P. Dubruel, and C. Leys, "Plasma Surface Modification of Biomedical Polymers: Influence on Cell-Material Interaction," *Plasma Chemistry and Plasma Processing*, vol. 32, pp. 1039-1073, 2012.

[69] R. Morent, N. De Geyter, M. Trentesaux, L. Gengembre, P. Dubruel, C. Leys, *et al.*, "Influence of Discharge Atmosphere on the Ageing Behaviour of Plasma-Treated Polylactic Acid," *Plasma Chemistry and Plasma Processing*, vol. 30, pp. 525-536, 2010.

[70] Z. J. Han, I. Levchenko, S. Kumar, M. M. A. Yajadda, S. Yick, D. H. Seo, *et al.*, "Plasma nanofabrication and nanomaterials safety," *Journal of Physics D: Applied Physics*, vol. 44, p. 174019, 2011.

[71] K. Furlan, A. Klein, and D. Hotza, "DIAMOND-LIKE CARBON FILMS DEPOSITED BY HYDROCARBON PLASMA SOURCES," *Rev. Adv. Mater. Sci*, vol. 34, pp. 165-172, 2013.

[72] B. W. Muir, S. L. Mc Arthur, H. Thissen, G. P. Simon, H. J. Griesser, and D. G. Castner, "Effects of oxygen plasma treatment on the surface of bisphenol A polycarbonate: a study using SIMS, principal component analysis, ellipsometry, XPS and AFM nanoindentation," *Surface and Interface Analysis*, vol. 38, pp. 1186-1197, 2006.

[73] K. Tsougeni, A. Tserepi, G. Boulousis, V. Constantoudis, and E. Gogolides, "Control of Nanotexture and Wetting Properties of Polydimethylsiloxane from Very Hydrophobic to Super-Hydrophobic by Plasma Processing," *Plasma Processes and Polymers,* vol. 4, pp. 398-405, 2007.

[74] N. Vourdas, A. Tserepi, and E. Gogolides, "Nanotextured super-hydrophobic transparent poly(methyl methacrylate) surfaces using high-density plasma processing," *Nanotechnology,* vol. 18, p. 125304, 2007.

[75] C. X. Wang, Y. Liu, H. L. Xu, Y. Ren, and Y. P. Qiu, "Influence of atmospheric pressure plasma treatment time on penetration depth of surface modification into fabric," *Applied Surface Science,* vol. 254, pp. 2499-2505, 2008.

[76] M. A. Hartney, D. W. Hess, and D. S. Soane, "Oxygen plasma etching for resist stripping and multilayer lithography," *Journal of Vacuum Science & Technology B,* vol. 7, pp. 1-13, 1989.

[77] S. J. Moss, A. M. Jolly, and B. J. Tighe, "Plasma oxidation of polymers," *Plasma Chemistry and Plasma Processing,* vol. 6, pp. 401-416, 1986.

[78] Y. Ikada, "Surface modification of polymers for medical applications," *Biomaterials,* vol. 15, pp. 725-736, 1994.

[79] R. Morent, N. De Geyter, T. Desmet, P. Dubruel, and C. Leys, "Plasma Surface Modification of Biodegradable Polymers: A Review," *Plasma Processes and Polymers,* vol. 8, pp. 171-190, 2011.

[80] J. J. A. Barry, M. M. C. G. Silva, K. M. Shakesheff, S. M. Howdle, and M. R. Alexander, "Using Plasma Deposits to Promote Cell Population of the Porous

Interior of Three-Dimensional Poly(D,L-Lactic Acid) Tissue-Engineering Scaffolds," *Advanced Functional Materials,* vol. 15, pp. 1134-1140, 2005.

[81] X. Fu, M. J. Jenkins, G. Sun, I. Bertoti, and H. Dong, "Characterization of active screen plasma modified polyurethane surfaces," *Surface and Coatings Technology,* vol. 206, pp. 4799-4807, 2012.

[82] S. Lerouge, M. R. Wertheimer, and L. H. Yahia, "Plasma Sterilization: A Review of Parameters, Mechanisms, and Limitations," *Plasmas and Polymers,* vol. 6, pp. 175-188, 2001.

[83] S. M. Mukhopadhyay, P. Joshi, S. Datta, and J. Macdaniel, "Plasma assisted surface coating of porous solids," *Applied Surface Science,* vol. 201, pp. 219-226, 2002.

[84] M. Pons, O. Joubert, P. Paniez, and J. Pelletier, "Plasma etching of polymers: A reinvestigation of temperature effects," *Journal of Applied Physics,* vol. 70, pp. 2376-2379, 1991.

[85] B. Akhavan, K. Jarvis, and P. Majewski, "Hydrophobic plasma polymer coated silica particles for petroleum hydrocarbon removal," *ACS applied materials & interfaces,* vol. 5, pp. 8563-8571, 2013.

[86] T. Schwarz-Selinger, A. Von Keudell, and W. Jacob, "Plasma chemical vapor deposition of hydrocarbon films: The influence of hydrocarbon source gas on the film properties," *Journal of Applied Physics,* vol. 86, pp. 3988-3996, 1999.

[87] A. von Keudell and W. Jacob, "Surface relaxation during plasma-enhanced chemical vapor deposition of hydrocarbon films, investigated by in situ ellipsometry," *Journal of Applied Physics,* vol. 81, pp. 1531-1535, 1997.

[88] S. R. Coulson, I. Woodward, J. P. S. Badyal, S. A. Brewer, and C. Willis, "Super-Repellent Composite Fluoropolymer Surfaces," *The Journal of Physical Chemistry B,* vol. 104, pp. 8836-8840, 2000.

[89] S. R. Coulson, I. S. Woodward, J. P. S. Badyal, S. A. Brewer, and C. Willis, "Plasmachemical Functionalization of Solid Surfaces with Low Surface Energy Perfluorocarbon Chains," *Langmuir,* vol. 16, pp. 6287-6293, 2000.

[90] P. Favia and R. d'Agostino, "Plasma treatments and plasma deposition of polymers for biomedical applications," *Surface and Coatings Technology,* vol. 98, pp. 1102-1106, 1998.

[91] N. Guerrouani, A. Baldo, A. Bouffin, C. Drakides, M.-F. Guimon, and A. Mas, "Allylamine plasma-polymerization on PLLA surface evaluation of the biodegradation," *Journal of Applied Polymer Science,* vol. 105, pp. 1978-1986, 2007.

[92] M. R. Sanchis, O. Calvo, O. Fenollar, D. Garcia, and R. Balart, "Surface modification of a polyurethane film by low pressure glow discharge oxygen plasma treatment," *Journal of Applied Polymer Science,* vol. 105, pp. 1077-1085, 2007.

[93] H. Shen, X. Hu, F. Yang, J. Bei, and S. Wang, "Combining oxygen plasma treatment with anchorage of cationized gelatin for enhancing cell affinity of poly(lactide-co-glycolide)," *Biomaterials*, vol. 28, pp. 4219-30, 2007.

[94] F. Siffer, J. Schultz, and V. Roucoules, "Alkene Pulsed Plasma Functionalized Surfaces: An Interfacial Diels-Alder Reaction Study," in *Adhesion*, ed: Wiley-VCH Verlag GmbH & Co. KGaA, pp. 289-303, 2006.

[95] M. Tatoulian, O. Bouloussa, F. Morière, F. Arefi-Khonsari, J. Amouroux, and F. Rondelez, "Plasma Surface Modification of Organic Materials: Comparison between Polyethylene Films and Octadecyltrichlorosilane Self-Assembled Monolayers," *Langmuir*, vol. 20, pp. 10481-10489, 2004.

[96] Y. J. Wu, R. B. Timmons, J. S. Jen, and F. E. Molock, "Non-fouling surfaces produced by gas phase pulsed plasma polymerization of an ultra low molecular weight ethylene oxide containing monomer," *Colloids and Surfaces B: Biointerfaces*, vol. 18, pp. 235-248, 2000.

[97] J. Yang, J. Bei, and S. Wang, "Enhanced cell affinity of poly (D,L-lactide) by combining plasma treatment with collagen anchorage," *Biomaterials*, vol. 23, pp. 2607, 2002.

[98] J. N. Rodriguez, F. J. Clubb, T. S. Wilson, M. W. Miller, T. W. Fossum, J. Hartman, *et al.*, "In vivo response to an implanted shape memory polyurethane foam in a porcine aneurysm model," *Journal of Biomedical Materials Research Part A*, vol. 102, pp. 1231-1242, 2014.

[99] P. Singhal, A. Boyle, M. L. Brooks, S. Infanger, S. Letts, W. Small, *et al.*, "Controlling the Actuation Rate of Low-Density Shape-Memory Polymer Foams in Water," *Macromolecular Chemistry and Physics*, vol. 214, pp. 1204-1214, 2013.

[100] Y.-J. Yu, K. Hearon, T. S. Wilson, and D. J. Maitland, "The effect of moisture absorption on the physical properties of polyurethane shape memory polymer foams," *Smart Materials and Structures*, vol. 20, p. 085010, 2011.

[101] H. J. Cloft and D. F. Kallmes, "Aneurysm Packing with HydroCoil Embolic System versus Platinum Coils: Initial Clinical Experience," *American Journal of Neuroradiology*, vol. 25, pp. 60-62, 2004.

[102] S. Hasan, R. Thompson, H. Emery, A. Nathan, A. Weems, F. Zhou, *et al.*, "Modification of shape memory polymer foams using tungsten, aluminum oxide, and silicon dioxide nanoparticles," *RSC Advances*, vol. 6, pp. 918-927, 2016.

[103] J. Milburn, A. Pansara, R. Martinez, and G. Vidal, "E-021 Initial experience using the Penumbra Coil 400: comparison of aneurysm packing and coil efficiency," *Journal of NeuroInterventional Surgery*, vol. 4, pp. A54-A55, 2012.

[104] A. I. Qureshi and A. L. Georgiadis, *Textbook of Interventional Neurology*: Cambridge University Press, 2011.

[105] J. N. Rodriguez, W. Hwang, J. Horn, T. L. Landsman, A. Boyle, M. A. Wierzbicki, *et al.*, "Design and biocompatibility of endovascular aneurysm filling devices," *Journal of Biomedical Materials Research Part A*, 2014.

[106] J. N. Rodriguez, M. W. Miller, A. Boyle, J. Horn, C.-K. Yang, T. S. Wilson, *et al.*, "Reticulation of low density shape memory polymer foam with an in vivo demonstration of vascular occlusion," *Journal of the Mechanical Behavior of Biomedical Materials,* vol. 40, pp. 102-114, 2014.

[107] J. M. Anderson, A. Rodriguez, and D. T. Chang, "FOREIGN BODY REACTION TO BIOMATERIALS," *Seminars in immunology,* vol. 20, pp. 86-100, 2008.

[108] J. M. Ortega, J. Hartman, J. N. Rodriguez, and D. J. Maitland, "Virtual treatment of basilar aneurysms using shape memory polymer foam," *Ann Biomed Eng,* vol. 41, pp. 725-43, 2013.

[109] E. A. Vogler and C. A. Siedlecki, "Contact activation of blood-plasma coagulation," *Biomaterials,* vol. 30, pp. 1857-69, Apr 2009.

[110] V. R. Kumar, S.L., *Robbins Basic Pathology*, 8th ed. Philadelphi, PA: Saunders/Elsevier, 2007.

[111] V. M. Donnelly and A. Kornblit, "Plasma etching: Yesterday, today, and tomorrow," *Journal of Vacuum Science & Technology A,* vol. 31, p. 050825, 2013.

[112] F. Egitto, F. Emmi, R. Horwath, and V. Vukanovic, "Plasma etching of organic materials. I. Polyimide in O2–CF4," *Journal of Vacuum Science & Technology B,* vol. 3, pp. 893-904, 1985.

[113] C. J. Mogab, A. C. Adams, and D. L. Flamm, "Plasma etching of Si and SiO2—The effect of oxygen additions to CF4 plasmas," *Journal of Applied Physics,* vol. 49, pp. 3796-3803, 1978.

[114] Y. Ozdemir, N. Hasirci, and K. Serbetci, "Oxygen plasma modification of polyurethane membranes," *Journal of Materials Science: Materials in Medicine,* vol. 13, pp. 1147-1152, 2002.

[115] M. Zelzer, D. Scurr, B. Abdullah, A. J. Urquhart, N. Gadegaard, J. W. Bradley, *et al.*, "Influence of the Plasma Sheath on Plasma Polymer Deposition in Advance of a Mask and down Pores," *The Journal of Physical Chemistry B,* vol. 113, pp. 8487-8494, 2009.

[116] A. J. Boyle, A. C. Weems, S. M. Hasan, L. D. Nash, M. B. B. Monroe, and D. J. Maitland, "Solvent stimulated actuation of polyurethane-based shape memory polymer foams using dimethyl sulfoxide and ethanol," *Smart Materials and Structures,* vol. 25, p. 075014, 2016.

[117] T. L. Barr and S. Seal, "Nature of the use of adventitious carbon as a binding energy standard," *Journal of Vacuum Science & Technology A,* vol. 13, pp. 1239-1246, 1995.

[118] D. J. Wilson, N. P. Rhodes, and R. L. Williams, "Surface modification of a segmented polyetherurethane using a low-powered gas plasma and its influence on the activation of the coagulation system," *Biomaterials,* vol. 24, pp. 5069-81, 2003.

[119] P. Van der Valk, A. Van Pelt, H. Busscher, H. De Jong, C. R. Wildevuur, and J. Arends, "Interaction of fibroblasts and polymer surfaces: relationship between surface free energy and fibroblast spreading," *Journal of biomedical materials research,* vol. 17, pp. 807-817, 1983.

[120] M. J. Dalby, M. O. Riehle, H. J. Johnstone, S. Affrossman, and A. S. Curtis, "Polymer-demixed nanotopography: control of fibroblast spreading and proliferation," *Tissue Eng,* vol. 8, pp. 1099-108, 2002.

[121] W. Hwang, B. L. Volk, F. Akberali, P. Singhal, J. C. Criscione, and D. J. Maitland, "Estimation of aneurysm wall stresses created by treatment with a shape memory polymer foam device," *Biomech Model Mechanobiol,* vol. 11, pp. 715-29, 2012.

[122] J. Rodriguez, Y.-J. Yu, M. Miller, T. Wilson, J. Hartman, F. Clubb, *et al.*, "Opacification of Shape Memory Polymer Foam Designed for Treatment of Intracranial Aneurysms," *Annals of Biomedical Engineering,* vol. 40, pp. 883-897, 2012.

[123] W. Krause, "Angiographic Contrast Agents," in *Vascular Diagnostics*, P. Lanzer and J. Rösch, Eds., ed: Springer Berlin Heidelberg, pp. 193-206, 1994.

[124] W. Krause and P. Schneider, "Chemistry of X-Ray Contrast Agents," in *Contrast Agents II*. vol. 222, W. Krause, Ed., ed: Springer Berlin Heidelberg, pp. 107-150, 2002.

[125] J. A. Ehrhard and P. Hennessey, "Radio-opaque polymeric compositions," ed: Google Patents, 2003.

[126] M. Modesti, N. Baldoin, and F. Simioni, "Formic acid as a co-blowing agent in rigid polyurethane foams," *European Polymer Journal*, vol. 34, pp. 1233-1241, 1998.

[127] L. D. Nash, N. C. Docherty, M. B. B. Monroe, K. P. Ezell, J. K. Carrow, S. M. Hasan, *et al.*, "Cold Plasma Reticulation of Shape Memory Embolic Tissue Scaffolds," *Macromolecular Rapid Communications*, 2016.

[128] J. Y. Cherng, T. Y. Hou, M. F. Shih, H. Talsma, and W. E. Hennink, "Polyurethane-based drug delivery systems," *International Journal of Pharmaceutics*, vol. 450, pp. 145-162, 2013.

[129] P. Gunatillake, R. Mayadunne, and R. Adhikari, "Recent developments in biodegradable synthetic polymers," in *Biotechnology Annual Review*. vol. Volume 12, M. R. El-Gewely, Ed., ed: Elsevier, pp. 301-347, 2006.

[130] A. B. Strong, *Fundamentals of Composites Manufacturing, Second Edition: Materials, Methods and Applications*: Society of Manufacturing Engineers, 2008.

[131] L. May-Hernández, F. Hernández-Sánchez, J. L. Gomez-Ribelles, and R. Sabater-i Serra, "Segmented poly(urethane-urea) elastomers based on polycaprolactone: Structure and properties," *Journal of Applied Polymer Science*, vol. 119, pp. 2093-2104, 2011.

[132] G. Mitchell, F. France, A. Nordon, P. L. Tang, and L. T. Gibson, "Assessment of historical polymers using attenuated total reflectance-Fourier transform infra-red spectroscopy with principal component analysis," *Heritage Science*, vol. 1, p. 28, 2013.

[133] C. Zhang, Z. Ren, Z. Yin, H. Qian, and D. Ma, "Amide II and Amide III Bands in Polyurethane Model Soft and Hard Segments," *Polymer Bulletin*, vol. 60, pp. 97-101, 2008.

[134] A. E. Segneanu, A. Dabici, I. Gozescu, P. Sfirloaga, and Z. Szabadai, *Organic Compounds FT-IR Spectroscopy*: INTECH Open Access Publisher, 2012.

APPENDIX

EFFECTS OF ELECTRON BEAM STERILIZATION ON SHAPE MEMORY POLYURETHANE FOAMS

A.1 Purpose

This appendix summarizes results from an engineering study assessing the effects of electron beam (E-beam) sterilization on shape memory polymer foam compositions used for the PED (Peripheral Embolization Device) currently under development by Shape Memory Medical, Inc.

This experiment was designed to investigate E-beam dose-dependent effects on three PED shape memory polymer foam compositions. Changes in thermomechanical properties and chemical composition were characterized for foam and neat polymer sample geometries.

A.2 Background

The purpose of this study is to provide a quantitative assessment of dose-dependent PED performance criteria, particularly effects on shape memory polymer (SMP) foam expansion rate. Results from a previous sterilization study on SMP foam showed negligible effects on wet glass transition temperature (T_g), dry T_g, mechanical properties, device morphology, shape memory capacity, and bulk material chemistry as determined by FTIR. These results make E-beam radiation a promising candidate for sterilizing shape memory polymer foam, especially when packaged with desiccant in a nitrogen-purged, vacuum-sealed foil pouch environment that mitigates oxidative species generation from ambient moisture and atmospheric oxygen during sterilization.

The most interesting result from preliminary testing was a trend of increasing expansion time with increasing sterilization dose. As shown in Figure A.1, this trend appeared to be more pronounced in compositions with lower percentages of N,N,N',N'-Tetrakis(2 hydroxypropyl)ethylenediamine (HPED). The hypothesis is that compositions with higher percentages of Triethanolamine (TEA) are more susceptible to radiation-induced material changes. This study will utilize compositions with different ratios of TEA and a composition that replaces TEA with glycerol, a polyol that has been shown to help resist oxidative degradation.

This study is designed to determine the repeatability of these dose- and composition-dependent expansion results and to understand their underlying cause. Clinically relevant PED foams with varying compositions will be sterilized at varying doses and their expansion profiles quantified. Neat polymer films with varying compositions will also be sterilized in different packaging environments to quantify the effects of material oxidation.

Preliminary results that motivated this study are summarized in the manuscript "Effects of Sterilization on Shape Memory Polyurethane Embolic Foam Devices" submitted to the ASME Journal of Medical Devices. A summary of the study process flow is outlined in Figure A.1.

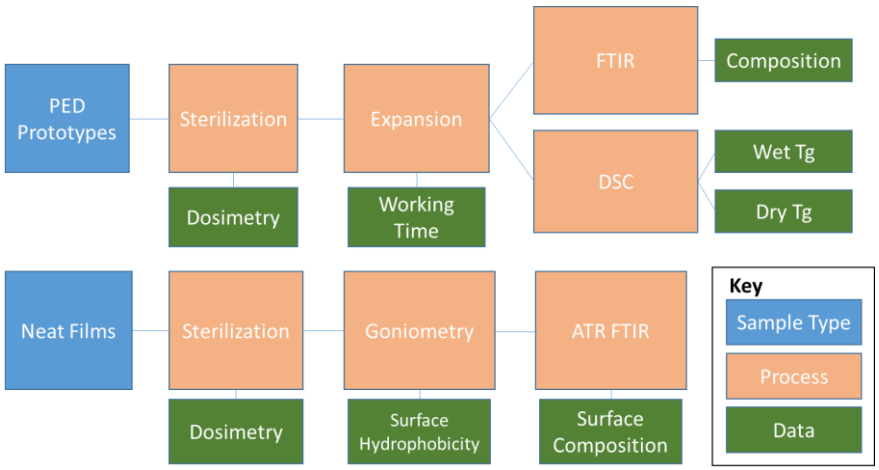

Figure A.1: Sample process flow.

A.3 Methods

A.3.1 Sample preparation

All samples were prepared in the Controlled Fabrication Laboratory at Texas A&M University under work order BG06. 8 mm foam samples were crimped over 0.008” nitinol wire. Crimped foam samples were placed within stainless steel introducers with luer locks (Biotex Part # 015-2513). Neat films were cut into 1.5 cm squares and adhered to a 0.020” polyethylene sheet using double-sided tape. All samples were packaged in nitrogen-purged, vacuum-sealed foil pouches (Beacon Converters, Biotex Part # 015-2000-013) with molecular sieve desiccant (Multisorb MiniPax), except for “O2 Films” packaged with ambient air and moisture without desiccant.

Table A.3: Foam traceability table

CFL Work Order BG06	
Foam IDs	
H30	160603PEDMH01
H60	160408PEDMH01
G40	160225RCHGF05

Table A.2: Neat film monomer traceability table

Neat Film Monomer Lot #s	
HPED	BCBQ0036V
TEA	BCBN8242V
HDI	H0324

A.3.2 Irradiation

Samples were irradiated at the Texas A&M National Center for Electron Beam Research on July 28, 2016. Dosimetry was measured using Alanine dosimeters and a Bruker Alanine dosimeter reader.

A.3.3 Expansion tests

Samples were held in a custom fixture that positioned the samples in the same imaging plane as a ¼" measurement reference for image calibration. The fixture was immersed in 37°C water and imaged at 30-second intervals until foam expansion was observed. Using ImageJ software, five diameter measurements were taken along the length of all 3 foam samples at each time point, for a total of 15 measurements. After

expansion, ~50 mg of moisture-plasticized foam was kept for wet DSC analysis. The remaining foam was vacuum dried at 50°C for ATR and dry DSC analysis.

A.3.4 Differential scanning calorimetry (DSC)

DSC thermograms were obtained using a TA Instruments Q200. Dry T_g cycles consisted of hermetically sealing dried foam samples in an aluminum pan and cooling the sample to -40°C, holding isothermal for 2 minutes, ramping to 120°C, isothermal 2 minutes, returning to -40°C, isothermal 2 minutes, and ramping again to 120°C. All heating and cooling rates were 10°C/min. T_g was calculated from the inflection point on the second heating ramp to 120°C using TA Universal Analysis software. Wet DSC cycles consisted of cooling the hermetically sealed wet sample to -40°C, holding isothermal for 2 minutes, and ramping to 80°C at 10°C/min. Glass transition was determined as the inflection point of the thermogram using TA Universal Analysis Software.

A.3.5 ATR FTIR

ATR FTIR spectra were obtained using a Bruker ALPHA Infrared Spectrometer with a diamond ATR crystal. Data analysis was conducted using Bruker OPUS Spectroscopy software.

A.4 Results

A.4.1 Foam dosimetry

As seen in Table A.3, the delivered dose for each sample group was consistently within 1 kGy of the desired target dose. With the exception of the absolute H30 dose on the top of the pouch, all dosimeters were placed on the back of the foil pouch, opposite

of the beam source. When comparing the absolute H30 dose to the dose delivered after the beam passes through the H30 sample, there is a maximum dose shielding effect of only 0.362 kGy.

Table A.3: Foam sample dosimetry

	Target Dose (kGy)		
	25 kGy	**40 kGy**	**60 kGy**
Absolute (H30)	25.985	40.329	60.487
H30	25.623	40.311	60.244
H60	25.842	39.517	59.542
G40	25.539	40.577	59.659

A.4.2 Foam DSC

Table A.4 summarizes the dry and wet glass transition temperatures for each composition and dose. As seen in previous studies, there is no significant difference in dry T_g with increasing dose. Although there is a slight decrease in wet T_g with increasing dose, this is not anticipated to negatively impact medical device performance because all untreated foam compositions have wet T_gs significantly below body temperature.

The wet T_g for the H30 samples irradiated at 25 and 40 kGy could not be determined because the moisture plasticized glass transition temperature was too close to the freezing point of water for accurate calorimetric assessment. A glass transition temperature close to 0°C for irradiated H30 samples is realistic based on wet T_g depression trends in the other compositions.

Table A.4: Foam T_g summary

	Glass Transition Temperature (°C)			
	Control	**25 kGy**	**40 kGy**	**60 kGy**
H30 Dry	55.99	54.51	54.55	54.16
H30 Wet	4.85	-	-	5.77
H60 Dry	67.64	66.63	66.52	66.25
H60 Wet	18.18	15.12	17.32	16.76
G40 Dry	84.28	83.15	83.29	82.15
G40 Wet	32.91	29.2	28.31	27.67

A.4.3 Foam expansions

Figures A.2 to A.3 depict the unconstrained expansion data for each foam composition and dose configuration. In all cases, radiation caused an increase in ultimate expansion time. The G40 composition had the most dose-dependent trend in expansion time, with increasing dose leading to longer expansion times. The H30 and H60 sample groups did not show a dose-dependent trend for expansion time. For all 3 compositions, the highest dose of 60 kGy had the smallest variation in expansion profile, as indicated by standard deviation.

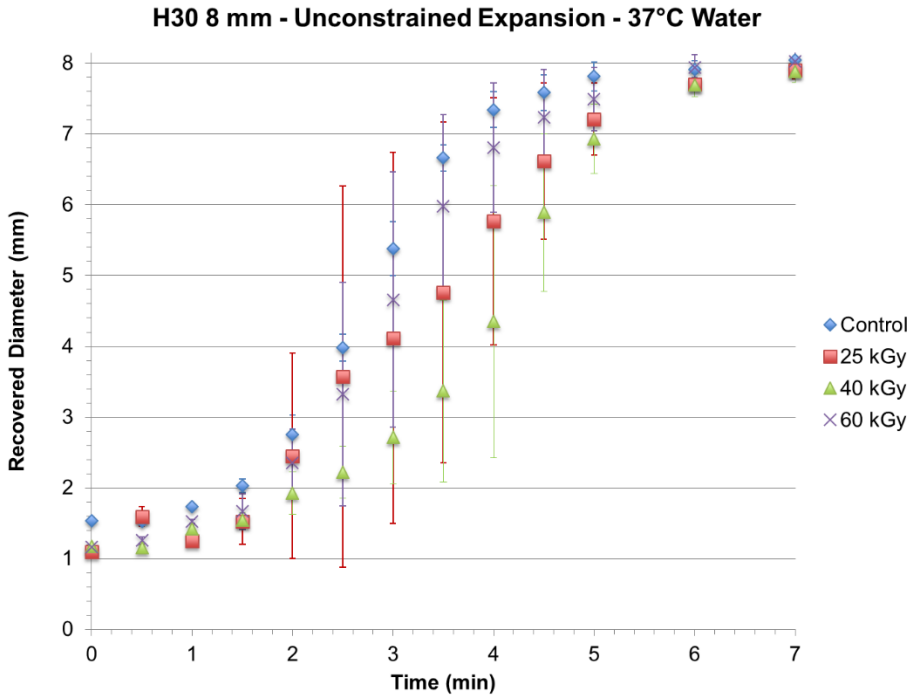

Figure A.2: 37°C aqueous unconstrained expansion of 1 cm long, 8 mm diameter H30 foam samples compressed over 0.008" nitinol wire.

As shown in Figure A.2 irradiated H30 samples had longer expansion times and larger standard deviations when compared to the untreated control foam. This increase in expansion time is attributed to increased intermolecular interactions between dangling chains at scission sites. Assuming this change in material performance is accounted for in the device design, it should not significantly affect the utility of an SMP embolic foam device.

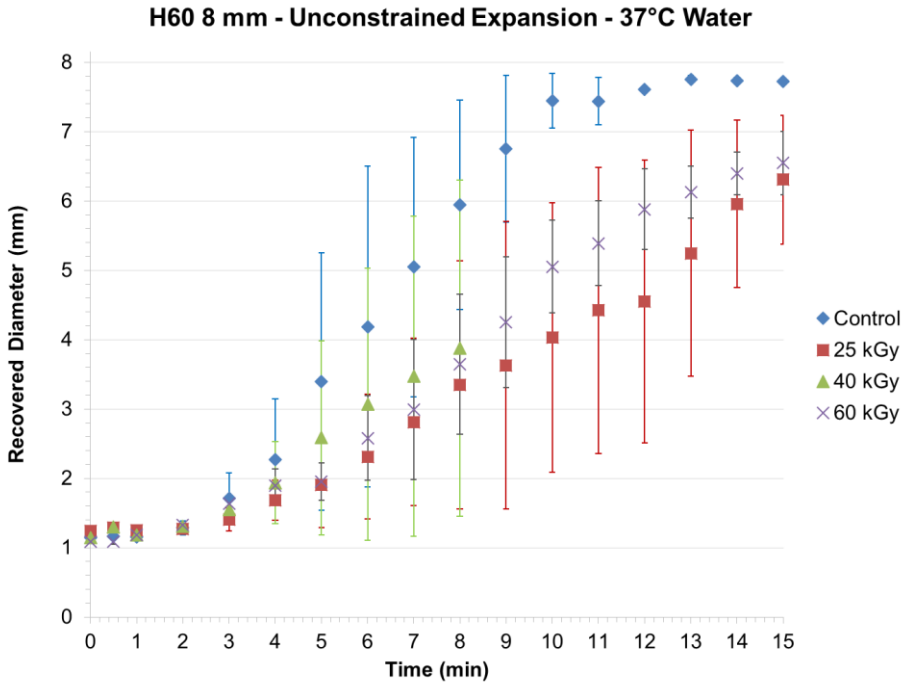

Figure A.3: 37°C aqueous unconstrained expansion of 1 cm long, 8 mm diameter H60 foam samples compressed over 0.008" nitinol wire.

The H60 samples in Figure A.3 shows a more exaggerated increase in expansion time than the H30 cohort. Previous studies showed an opposite trend, with lower HPED content foams showing a more significant increase in expansion time with increasing dose. Regardless of this discrepancy, the observed changes in expansion time for any data set have not been significant enough to significantly impact device performance.

The 40 kGy curve is truncated due to a failure during image acquisition. These samples continued to expand, but there are no images past the 8-minute time point for quantitative measurements. Images were captured and measured to convey changes in expansion rate, not ultimate shape recovery. The irradiated samples are not plotted to full

expansion, but previous results show there is no concern for diminished ultimate shape recovery for the dose range of 25–60 kGy.

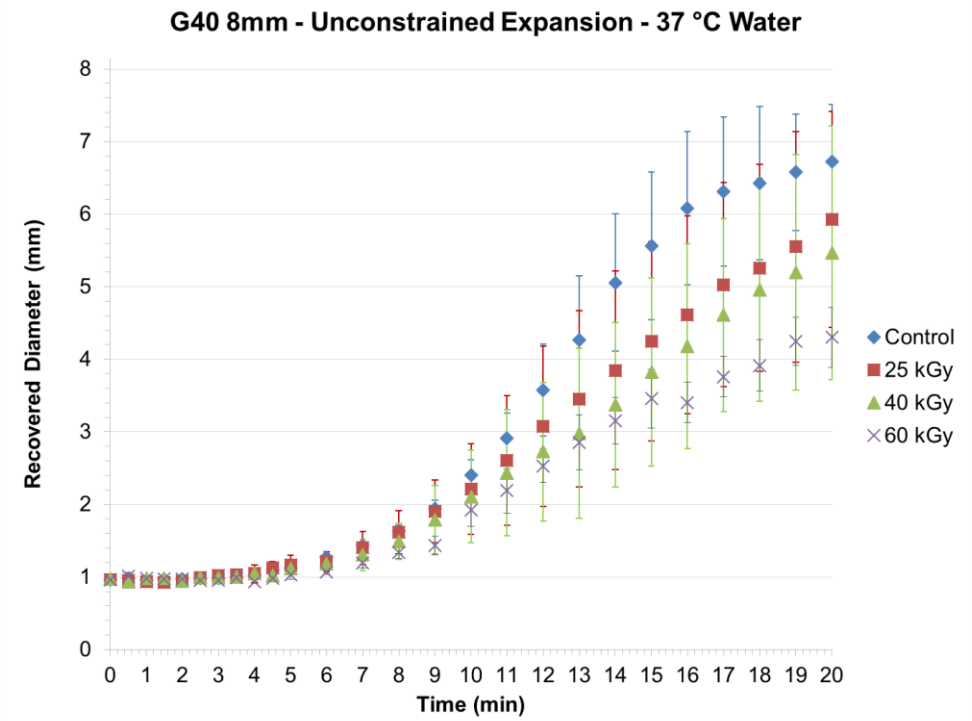

Figure A.4: 37°C aqueous unconstrained expansion of 1 cm long, 8 mm diameter G40 foam samples compressed over 0.008" nitinol wire.

The G40 foams in Figure A.4 howed the clearest trend for increasing expansion time with increasing dose. This plot suggests the G40 composition is not resistant to radiation effects as hypothesized in the study rationale.

A.4.4 Foam ATR

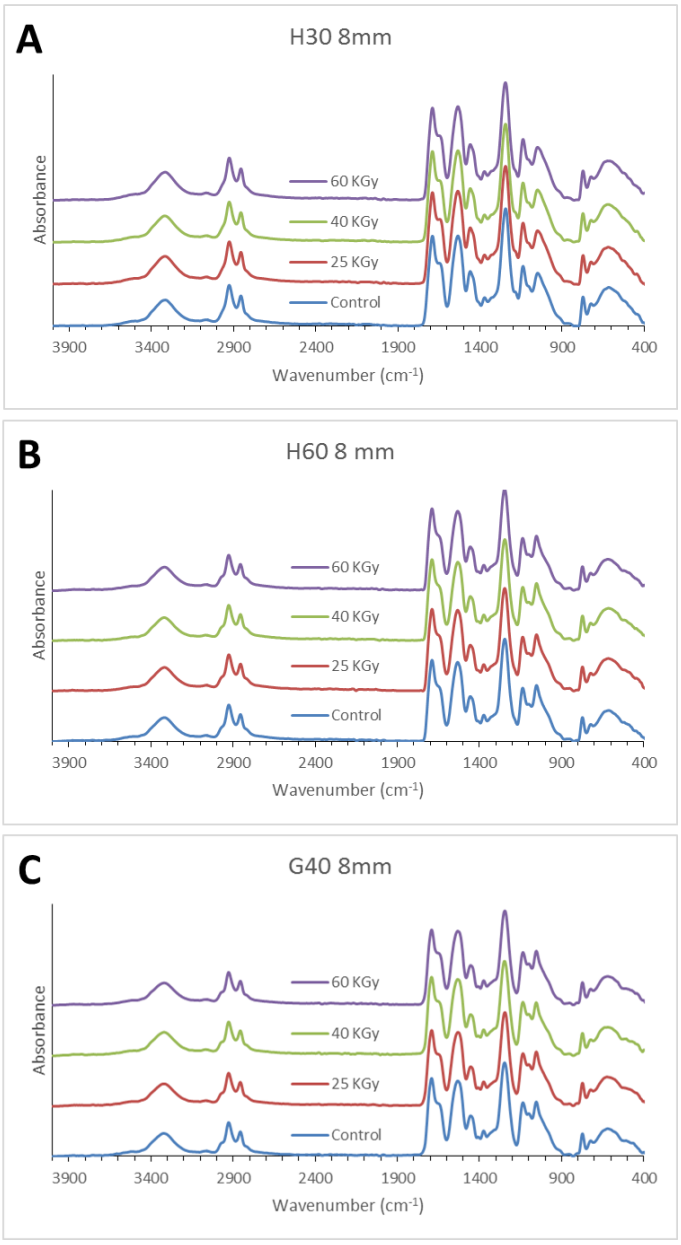

Figure A.5: ATR FTIR Spectra of SMP foams after expansion and vacuum drying at 50°C. A – H30 foam. B – H60 Foam. C – G40 Foam.

The ATR spectra in Figure A.5 A–C show no significant dose-dependent changes in any of the three material compositions. Although slight changes in foam

expansion kinetics are observed, the changes in the material are not significant enough to change the infrared spectra

A.4.5 Film dosimetry

As with the foam dosimetry, the dose delivered to the neat polymer films was within ±3 kGy of the target dose. Film dosimetry is summarized in Table A.5.

Table A.5: Film dosimetry summary

	Target Dose		
	25 kGy	**40 kGy**	**60 kGy**
H30 N2	26.496	42.197	62.396
H60 N2	26.365	40.587	60.543
H30 O2	26.263	41.472	61.197
H60 O2	26.677	41.920	61.742

A.4.6 Film ATR

Changes in packaging conditions were anticipated to have the greatest effect on oxidation reactions that occur predominately at the material surface. ATR was used over transmission FTIR to achieve higher resolution of the surface chemistry. Figure A.6 summarizes ATR spectra of neat polymer films sterilized under inert packaging conditions. All spectra were identical, except for a new peak at 960 cm^{-1} for the H60 sample sterilized at 40 kGy. This peak corresponds with an aliphatic amine oxide functional group.[134] This group is hypothesized to form due to the oxidation of the tertiary amine in TEA and HPED. This amine oxide peak was not observed in any of the N2 packaged foam ATR spectra.

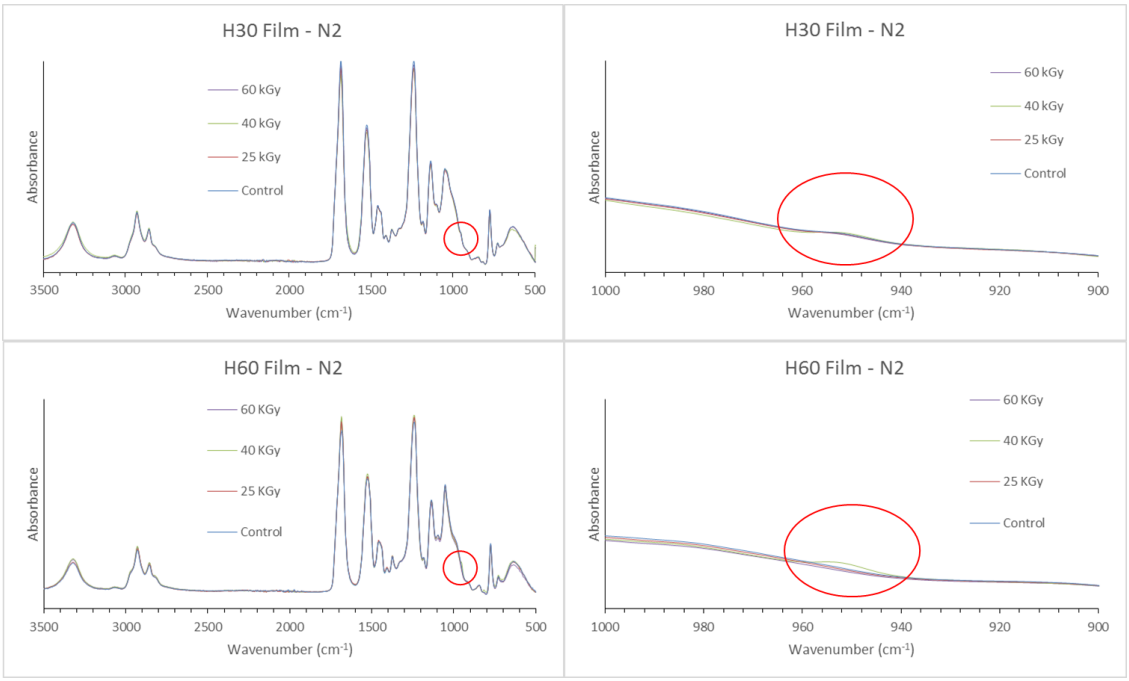

Figure A.6: ATR spectra of neat polymer films irradiated under inert packaging conditions (N2).

Figure A.7 summarizes ATR spectra for neat polymer films sterilized under ambient oxygen and moisture. Samples irradiated under these conditions had more amine oxide formation compared to the inert packaged materials. Amine oxide peaks at 960 cm^{-1} are more pronounced and occur at lower doses. When compared to H30 material, the H60 composition was more susceptible to amine oxide formation in both packaging configurations. This result is congruent with higher H60 sensitivity to radiation-induced changes in foam expansion rate.

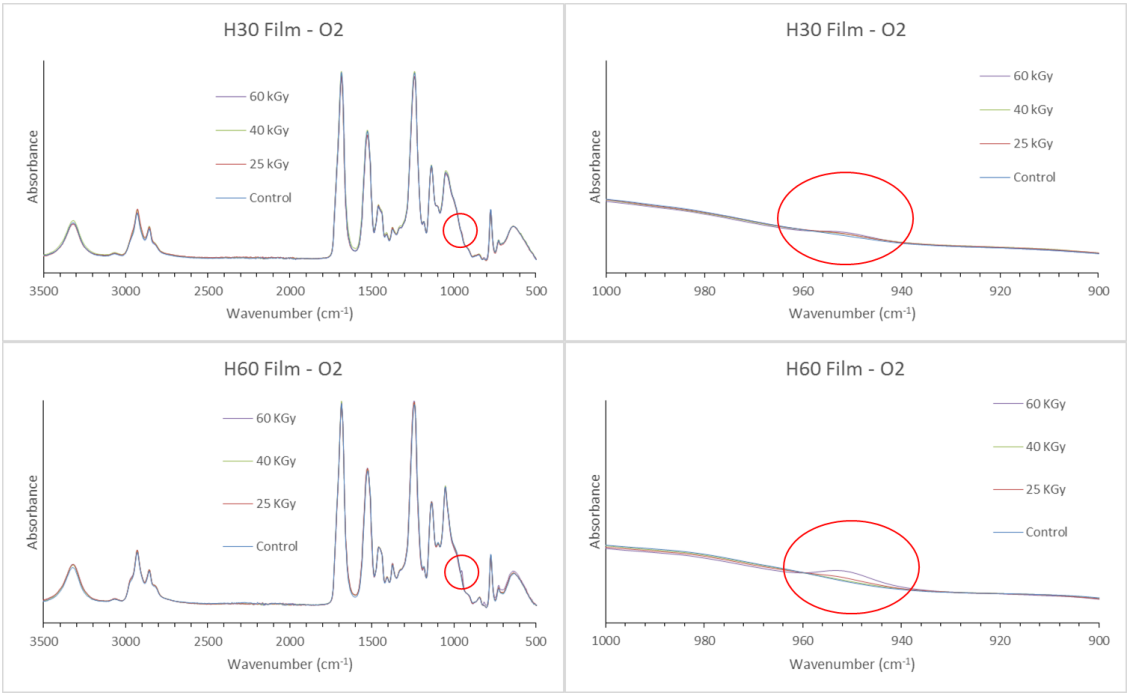

Figure A.7: ATR spectra of neat polymer films under ambient oxygen and moisture packaging conditions (O2).

A.4.7 Film contact angle

Contact angle measurements were inconclusive. It is hypothesized that the two sides of the polymer film have different surface finishes that would affect the wetting behavior of a water droplet. The film sides were not documented during sample preparation and testing; thus, the contact angle data is convoluted by changes in material composition and undocumented differences in surface roughness. The samples have since been exposed to ambient moisture for multiple days, further convoluting any subsequent tests. This data was intended to support hypotheses in material changes but is not critical for assessing device performance. This data was determined to be secondary and not critical enough to repeat for this study.

A.4.8 Color changes

Yellowing was observed for all neat and foamed compositions at all doses. This aesthetic change is hypothesized to be independent from amine oxide formation observed in select ATR spectra because it is observed in all irradiated samples. This color change affects wavelengths in the visible spectrum not covered in FTIR analysis. Electron beam–induced color changes are not atypical for materials, even at low doses. When considering all other data, these color changes are considered to be cosmetic with negligible effects on material performance. Observed color changes are summarized in Figures A.8 and A.9.

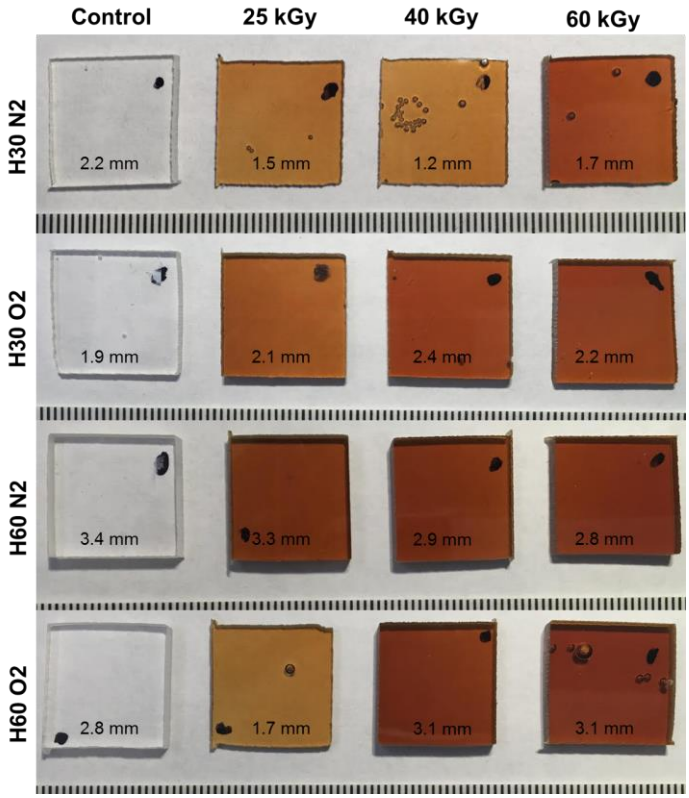

Figure A.8: Qualitative color change of neat polymer films. Film thickness reported for each film in mm.

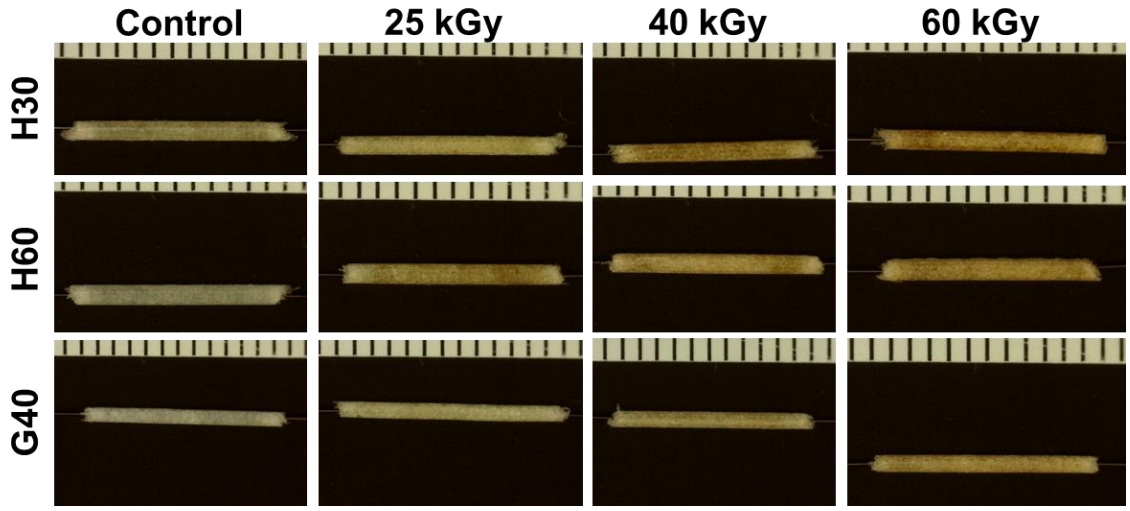

Figure A.9: Qualitative color change of crimped polymer foams.

A.5 Conclusion

Based on the presented body of data, the proposed material compositions have stable performance characteristics when exposed to 25–60 kGy of Electron beam radiation under inert packaging conditions. Packaging under inert conditions helps prevent the formation of amine oxides, especially at lower doses, such as 25 kGy. Medical devices using these material compositions are anticipated to maintain important performance behavior, including shape memory expansion, when sterilized at an Ebeam dose of 25 kGy.